博士論文(要約)

Development of injection scheme of antiprotons and production of antihydrogen atoms in low-lying excited states

(反陽子入射方法の開発と低励起状態反水素原子の生成)

田島　美典

Contents

Chapter 1

Introduction

This thesis mainly describes research and development to measure ground-state hyperfine splitting of antihydrogen atoms by ASACUSA collaboration. Comparison of the measurement of antihydrogen atoms with that of hydrogen atoms is a unique probe to test CPT symmetry. ASACUSA collaboration is aiming for the measurement at relative precision of ppm using atomic beams of antihydrogen.

1.1 Motivation

1.1.1 Antimatter

The theory of relativity and the quantum mechanics are two revolutions in physics of 20th century. However, the theories were incompatible. To address this problem, Paul Dirac proposed an alternative wave equation which is consistent with the quantum mechanics and the theory of special relativity in 1928 [1]. The equation, which is known as the Dirac equation, describes the states of a spin-1/2 particle, with positive and negative energies. The latter state, a particle with negative energy, was interpreted as the evidence of the existence of an antiparticle, which had never been observed before. In 1932, Carl Anderson discovered a new particle whose mass is the same and its charge is opposite to an electron [2]. This was identified as a positron, an antiparticle of electron. Antiproton, the antiparticle of proton, was discovered in 1955 by Owen Chamberlain, Emilio Segrè, and their group at Bevatron, a proton synchrotron at Berkley [3]. Protons are accelerated up to 6.2 GeV and injected onto a target made by

copper. The antiproton was generated via

$$p + N \rightarrow p + N + p + \overline{p} \tag{1.1}$$

where N corresponds to the target nucleus. We note that the baryon number is conserved in this reaction - it is an observational fact that the baryon number is conserved in every elementary particle reactions.

1.1.2 Baryon asymmetry

The discovery of antiproton leads to a great mystery in physics - the baryon asymmetry. It is natural to assume the Big Bang produced equal amount of particles and antiparticles. And all known reactions between particles (and antiparticles) conserve the baryon number. But it is also an observational fact that the number of baryons in the universe is much larger than that of antibaryons. Alpha Magnetic Spectrometer (AMS) collaboration reported the upper limit on the flux ratio of antihelium ($\overline{\mathrm{He}}$) to helium (He) of $< 1.1 \times 10^{-6}$ [4]. They upgraded the detector and measurement is ongoing now at the international space station. Antimatters outside of the solar system are also investigated from observations of x-rays and γ-rays emitted at annihilations which have not observed a significant amounts of antimatter. How it was possible that the universe has evolved to the current matter-dominant universe is still an open question.

The baryon asymmetry can be defined by η given by

$$\eta = \left.\frac{N_B - N_{\overline{B}}}{N_\gamma}\right|_{T\sim 2.7\mathrm{K}} \sim \left.\frac{N_B - N_{\overline{B}}}{N_B + N_{\overline{B}}}\right|_{T\geq 1\mathrm{GeV}} \tag{1.2}$$

where N_B is the number of baryons, $N_{\overline{B}}$ is the number of antibaryons, N_γ is the number of photons, and T is the temperature of the universe. The current temperature is determined at 2.72548$\pm$0.00057 K from a cosmic microwave background (CMB) [5]. The right side corresponds to the hot universe and the left side corresponds to the current universe after most of baryons and antibaryons, once existed in hot universe, annihilated. The baryon asymmetry is estimated at $\eta \sim 6 \times 10^{-10}$ using the CMB radiation [6].

There have been several scenarios which are proposed to explain this asymmetry. One of the prominent scenarios was proposed by Andrei Sakharov, in which three conditions (Sakharov's conditions) must be met in an interaction [7]. The conditions are that baryon number is

not conserved, C and CP symmetry is violated, and the interaction occurs out of thermal equilibrium. The first condition can be met if there is the grand unification between the strong interaction and the electroweak interaction, and there is a consensus among physicists that the grand unification must happen in higher energy scale which we cannot reach in high energy accelerators. The third condition can be met if the universe is still evolving, which again most physicists agree. The second condition is a key if this scenario can be accepted.

1.1.3 Discrete symmetries and its violations

C symmetry and CP symmetry are among discrete symmetries (and their combination) the physical laws have. There are three discrete symmetries C, P, and T symmetry which have been particularly studied in the modern physics. These symmetries are defined as the invariance under charge conjugation (C) which is a transformation between particles and antiparticles, parity inversion (P), and time reversal (T), respectively. CP symmetry is defined as the invariance under combined transformations of C and P. Similarly, CPT symmetry is defined using combined transformations of C, P, and T. At first, it was believed that these symmetries exactly hold. Then, Chien-Shiung Wu experimentally observed the asymmetry of angular distribution of electrons coming from beta decays of polarized ^{60}Co [8] which means the violation of P symmetry in weak interaction as proposed by Chen-Ning Lee and Tsung-Dao Yang [9]. The violation of C symmetry is also known such that all neutrinos are left-handed and all antineutrinos are right-handed. In addition, CP violations are directly observed in the decay process of Kaon [10] [11], B meson [12] [13]. Therefore, it seems Sakharov's three conditions can be satisfied within the Standard Model in principle. However, the baryon asymmetry including known CP violations can be estimated at $10^{-20} \ll 6.0 \times 10^{-10}$ [14], indicating that current level of asymmetry is not likely to be realized within the framework of the Standard Model.

Sakharov introduced his three conditions under the assumption that CPT symmetry is conserved in the process. The assumption seems very reasonable because CPT symmetry is mathematically derived by assuming quantum field theory, locality, and Lorentz invariance. For example, the Standard Model satisfies the assumptions which means CPT symmetry holds in the Standard Model. But we note that if CPT symmetry is allowed to be broken, the baryon asymmetry can be naturally explained. And progress of theoretical work on super string theory implies that possibility of non-local effect at very short distance (very high energy). A new theory beyond the Standard Model is indeed necessary to explain not only the baryon

asymmetry, but also other observations such as neutrino oscillations [15][16], dark matter, dark energy, and so on. The experimental investigation whether CPT symmetry is broken, and if not how far the symmetry is conserved, should give a new insight for the baryon asymmetry and the fundamental framework of the particle physics.

1.2 Test of CPT symmetry through spectroscopy of antihydrogen atoms

1.2.1 Test of CPT symmetry

It is known that any difference between matter and antimatter automatically means CPT violation, because the mass, lifetime, absolute value of charge, magnetic moment are the same as those of an antimatter when CPT symmetry holds. The test of CPT symmetry is possible by comparison between matter and antimatter. Since we do not know how a violation occurs, it is important to test in many systems such as leptons, baryons, atoms, and so on regarding different interactions. According to Greenberg [17], an interacting theory which violates CPT invariance necessarily violates Lorentz invariance. It is also reported that the baryon asymmetry can be explained within thermal equilibrium if Lorentz invariance is broken [18]. Although there is no established theory including CPT violation, Alan Kostelckeý *et al.* consider Lagrangian which contains all possible Lorentz-violating interaction terms [19] [20]. It is called the Standard-Model Extension.

In general, energy shifts in precision measurements can be expressed as

$$\Delta E \sim \left(\frac{m}{\Lambda_{NP}}\right)^n \times m \tag{1.3}$$

where $n > 0$ and m is a characteristic energy scale of the system, in order to probe new physics at scale Λ_{NP} [21]. For example, if we expect a CPT-violating new physics at the Plank scale and we conduct the experiment in GeV range, the expected energy shift due to CPT-violation is calculated to be around 10^{-19} GeV by substituting $n = 1$, $m \sim$ GeV, and $\Lambda_{NP} \sim 10^{19}$ GeV [22]. The mass difference between K^0 and $\overline{K^0}$ is often referred as the most stringent test of CPT symmetry because of its high relative precision, where

$$|m_{K^0} - m_{\overline{K^0}}| < 4.0 \times 10^{-19}\,\mathrm{GeV} \sim 100\,\mathrm{kHz}\ (\mathrm{CL} = 95\%) \tag{1.4}$$

is obtained, in terms of the energy shift, from the measurement of strangeness oscillation between K^0 and $\overline{K^0}$ [23]. The upper limit is larger than 10^{-19} GeV, which means the result is not excluding a CPT violation at the Plank scale. We propose the spectroscopy of the ground-state hyperfine splitting of antihydrogen atom (and its comparison with available spectroscopic data of hydrogen atom) as a new probe to investigate CPT symmetry. The value of the ground-state hyperfine splitting is around 1.4 GHz, thus, a ppm level of the spectroscopy would enable us to test the energy shift due to the CPT violation in a few kHz level, which far exceeds the upper limit obtained from K^0-$\overline{K^0}$ system.

1.2.2 Antihydrogen

An antihydrogen atom which is antimatter of an hydrogen atom and the simplest anti-atom have been considered as a unique probe for a test of CPT symmetry. Antihydrogen atoms were produced experimentally and observed by PS210 collaboration in 1995 at the Low Energy Antiproton Ring (LEAR) of the European Organization for Nuclear Research (CERN) for the first time [24]. Antiprotons at 1.9 GeV/c are injected into Xenon-cluster target and an antihydrogen atom is produced from injected antiproton and a pair-produced e^+. 11 antihydrogen atoms including 2 ± 1 backgrounds were observed. At that time, the energy of the antihydrogen atoms is $\sim$GeV, which is not appropriate for precision spectroscopy. In 2000, the Antiproton Decelerator (AD) at CERN was started to run as the only facility in the world to supply a bunch of 10^7 antiprotons every two minutes at low energy of 5.3 MeV, which leads to production of antihydrogen atoms for a precision measurement in 2002 [25] [26]. Investigation of antihydrogen atoms is currently ongoing by several collaborations at AD. Antihydrogen Laser Physics Apparatus (ALPHA) and Antihydrogen Trap (ATRAP) collaborations are aiming for measuring the 1S-2S transition frequency of antihydrogen atom. Atomic Spectroscopy and Collisions Using Slow Antiprotons (ASACUSA) collaboration is aiming for measuring the hyperfine splitting in the ground-state of antihydrogen atom. Antihydrogen Experiment: Gravity, Interferometry, Spectroscopy (AEGIS), the Gravitational behavior of Antihydrogen at Rest (GBAR), and ALPHA collaborations are aiming for test of the weak equivalence principle. Recently ALPHA collaboration reported the first spectroscopy of antihydrogen atoms [27] and the antihydrogen study has been one of active research fields.

1.2.3 Hyperfine splitting

The hyperfine splitting ΔE_{HFS} is caused by interactions between magnetic dipole moments of the electron and the proton for the hydrogen atom, and between that of the positron and the antiproton for the antihydrogen atom. For the case of a ground-state hydrogen atom, the total angular momentum quantum number of electron is $j = 1/2$ and the spin angular momentum quantum number of proton is $I = 1/2$. Therefore the ground state of a hydrogen atom splits into two levels with total angular momentum quantum number $F = 1$ and $F = 0$. The best experimental result of hydrogen atoms is given by [28][29][30]

$$\nu_{\mathrm{HFS}} = 1\,420\,405\,751.7667(9)\,\mathrm{Hz}. \tag{1.5}$$

The ground-state hyperfine splitting of an hydrogen atom ΔE_{HFS} is theoretically given by

$$\begin{aligned} \Delta E_{\mathrm{HFS}} &= \frac{4\mu_0}{3\pi}\mu_B\mu_p\left(\frac{m_r}{a_0 m_e}\right)^3(1+\Delta) \\ &= E_F^p(1+\Delta) \end{aligned} \tag{1.6}$$

where $\mu_B = e\hbar/(2m_e)$ is the Bohr magneton, μ_p is a magnetic dipole moment of a proton, $m_r = m_e m_p/(m_e + m_p)$ is the reduced mass, a_0 is the Bohr radius, E_F^p is the energy due to the Fermi contact interaction, and Δ is a correction. The correction is mainly due to QED and the proton structure. In particular, the latter part, depending on the proton structure, dominates the uncertainty of the calculation. The largest correction other than QED about 40 ppm is Zemach correction Δ_Z given by

$$\Delta_Z = -2\alpha m_r r_Z(1+\delta_Z^{\mathrm{rad}}) \tag{1.7}$$

where $\delta_Z^{rad} \sim 0.01$ is a radiative correction and r_Z is the Zemach radius given by

$$r_Z = -\frac{4}{\pi}\int_0^\infty \frac{dQ}{Q^2}\left(G_E(Q^2)\frac{G_M(Q^2)}{1+\kappa} - 1\right) \tag{1.8}$$

where G_E and G_M are electric and magnetic form factors of proton and κ is the proton anomalous magnetic moment in nuclear magnetons [31]. The expected precision of our proposed experiment to measure the ground-state hyperfine splitting of antihydrogen atoms is the relative uncertainty of 10^{-6}. This enables us the comparison between antihydrogen and hydrogen

from the level of Δ_Z, which gives us a new information on the form factors of antiproton assuming the magnetic moment of antiproton and proton are equal. If the magnetic moment of antiproton differs from that of proton by more than 10^{-6}, our experiment clearly detect the difference. The magnetic moment of the antiproton is measured by BASE collaboration to be equal to that of proton with relative uncertainty of 0.8×10^{-6} [32], and our experiment will provide an independent confirmation of the result.

1.2.4 Measurement method using atomic beams

In a weak magnetic field, the energy levels are split further into $2F + 1$ levels with $m = -F$, ..., $F - 1, F$ where m is a quantum number corresponding to the projection of F along the magnetic field. Considering the selection rules, transitions with $\Delta F = \pm 1$ or 0, $\Delta m = \pm 1$ or 0 may occur. Those with $\Delta m = 0$ are called σ transitions and those with $\Delta m = \pm 1$ are called π transitions.

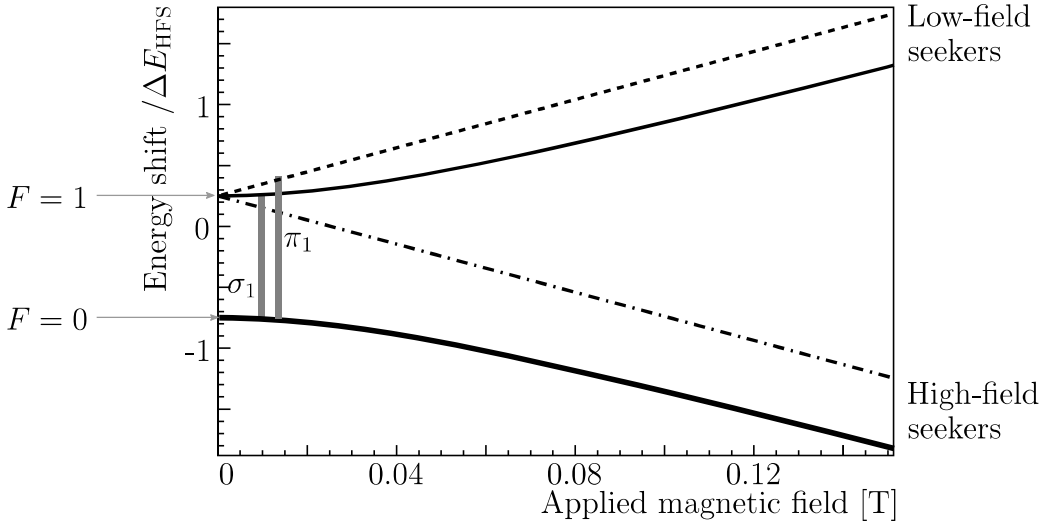

Figure 1.1: Breit-Rabi diagram of a ground-state hydrogen atom. There are low-field seekers and high-field seekers with different dependence as a function of applied magnetic field. The vertical axis shows the energy shift due to the hyperfine interaction divided by the ground-state hyperfine splitting.

Fig. 1.1 shows the energy levels as a function of applied magnetic field. It is called Breit-Rabi diagram [33]. The energy levels with parallel magnetic moment to the magnetic field decreases as a function of magnetic field because the interaction of the magnetic moment $\boldsymbol{\mu}$ with the magnetic field $\boldsymbol{B}$ is given by $-\boldsymbol{\mu} \cdot \boldsymbol{B}$. The atoms in these energy levels are called high-field seekers, because the force is given by $\nabla(\boldsymbol{\mu} \cdot \boldsymbol{B}) = +\mu \nabla |\boldsymbol{B}|$ and they are attracted towards the regions with high magnetic field strength. On the other hand, the energy levels with anti-parallel

magnetic moment to the magnetic field increases as a function of magnetic field. The atoms in these levels are called low-field seekers because the force is given by $\nabla(\boldsymbol{\mu}\cdot\boldsymbol{B}) = -\mu\nabla|\boldsymbol{B}|$ and they are attracted towards the regions with low magnetic field strength.

The energy levels are given by

$$-\frac{\Delta E_{\rm HFS}}{4} + g_I\mu_B B + \frac{\Delta E_{\rm HFS}}{2}\sqrt{(1+2x+x^2)} \tag{1.9}$$

$$-\frac{\Delta E_{\rm HFS}}{4} + \frac{\Delta E_{\rm HFS}}{2}\sqrt{(1+x^2)} \tag{1.10}$$

$$-\frac{\Delta E_{\rm HFS}}{4} - g_I\mu_B B + \frac{\Delta E_{\rm HFS}}{2}\sqrt{(1-2x+x^2)} \tag{1.11}$$

$$-\frac{\Delta E_{\rm HFS}}{4} - \frac{\Delta E_{\rm HFS}}{2}\sqrt{(1+x^2)} \tag{1.12}$$

using

$$x = \frac{(g_J - g_I)\mu_B B}{\Delta E_{\rm HFS}} \tag{1.13}$$

where g_I and g_J are the nuclear and electronic gyromagnetic ratio expressed by the Larmor angular frequency divided by magnetic field. The frequency of σ_1 transition, corresponds to the energy difference between two levels given by Eq.(1.10) and Eq.(1.12), is

$$\nu_{\sigma_1} = \frac{\Delta E_{\rm HFS}}{h}\sqrt{1+x^2}. \tag{1.14}$$

The frequency of π_1 transition, corresponds to the energy difference between two levels given by Eq.(1.9) and Eq.(1.12), is

$$\nu_{\pi_1} = \frac{\Delta E_{\rm HFS}}{h}\left(\frac{1+x}{2} + \frac{\sqrt{1+x^2}}{2} + g_I\frac{\mu_B B}{\Delta E_{\rm HFS}}\right) \tag{1.15}$$

These two frequencies will change low-field seekers to high-field seekers and vice versa.

The ASACUSA collaboration is aiming for a spectroscopy of ground-state hyperfine splitting of antihydrogen atoms using atomic beams. The experimental setup consists of a spin-polarized antihydrogen beam source and a spectrometer which is made of a microwave cavity, a sextupole magnet, and an antihydrogen detector. The spin-polarized antihydrogen atoms are extracted using magnetic field gradient called a cusp configuration (described later). A basic idea is proposed in [34]. The magnetic field of the sextupole magnet becomes strong as radial distance from the beam axis increases. Figure1.2(a) shows that beams of low-field-seeking antihydrogen are focused by the magnet onto the antihydrogen detector when microwave is turned off or the

frequency is off resonance of transitions. On the other hand, Fig.1.2(b) shows that the low-field seekers become high-field seekers by the applied microwave in the cavity with a right frequency, the beam is defocused by the magnet, and less antihydrogen atoms reach the detector. Therefore the transition frequency is determined from the count rate at the antihydrogen detector as a function of the frequency of the applied microwave.

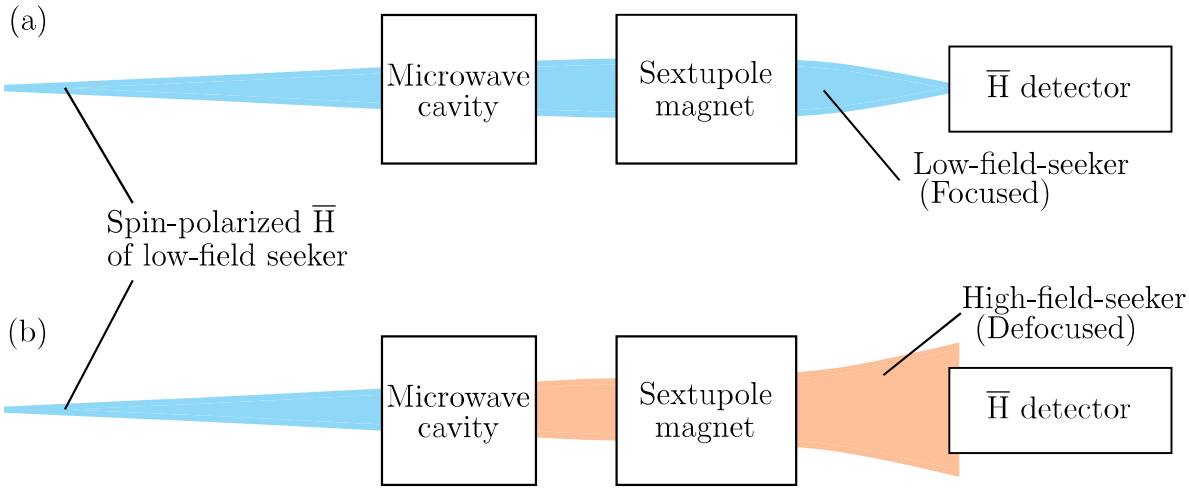

Figure 1.2: A principle of measurement for ground-state hyperfine splitting of antihydrogen atoms in ASACUSA antihydrogen experiment. The setup consists of a spin-polarized antihydrogen beam source and a spectrometer which is made of a microwave cavity, a sextupole magnet, and an antihydrogen detector. (a) The spin-polarized beams of low-field-seeking antihydrogen are focused by the magnet onto the antihydrogen detector when microwave is turned off or the frequency is off resonance of transitions. (b) The low-field seekers become high-field seekers by the applied microwave in the cavity with a right frequency, the beam is defocused by the magnet, and less antihydrogen atoms reach the detector. The transition frequency is determined from the count rate at the antihydrogen detector as a function of the frequency of the applied microwave.

The same spectrometer (the cavity and the sextupole magnet) has been also developed for measurement of ground-state hyperfine splitting of hydrogen atoms and a relative precision of 2.7×10^{-9} [35] is achieved which is better than the old measurements using atomic beams of hydrogen [36][37]. The precision to determine the center frequency of the count rate as a function of the applied frequency of the cavity can be estimated by

$$\delta \sim \frac{1}{T_{\mathrm{int}}\sqrt{N}} \frac{\sigma_R}{\Delta_R} \tag{1.16}$$

where T_{int} is interaction time corresponding to the traveling time through the cavity with the length of 105.5 mm [38] for our spectrometer, N is the number of frequency data points, Δ_R is the count rate drop, and σ_R is the average error bar of a data point [35]. It suggests that

the traveling time, in other words, the kinetic energy of antihydrogen atoms is important for precision. The measurement of hydrogen atoms are performed using those with kinetic energy of ~ 50 K (~ 900 m/s), which means $1/T_{\rm int}$ is 8.5 kHz. Majorana spin flip can be ignored for kinetic energy ~ 50 K. This means the proposed experiment is promising to achieve the relative precision of ppm with sufficient small kinetic energy and enough statistics.

Compared with the measurement very recently reported by ALPHA collaboration with the relative precision of 10^{-4} at 1420.4 ± 0.5 MHz [39] using trapped antihydrogen atoms in strong magnetic field, our method using atomic beams of antihydrogen has an advantage because the microwave cavity is located in magnetic-field-free region and the spectral line width should be reduced to achieve higher precision.

1.3 Structure of this thesis

In order to realize the proposed experiment, chapter 2 describes about development of antihydrogen beams extracted from the source to the downstream and detected by the antihydrogen detector. Then chapter 3 focuses on the remaining issue to perform the spectroscopy, the quality of produced antihydrogen atoms. In order to produce many antihydrogen atoms with small kinetic energy, injection of antiprotons with small energy spread into antihydrogen production region is developed, which is the main work of this thesis. Production rate of antihydrogen atoms is greatly improved which leads to the improvement of the signal to noise ratio for detection of antihydrogen atoms. A distribution of atomic states is measured and antihydrogen atoms in low-lying excited states are observed which is an important step for the spectroscopy of ground-state antihydrogen atoms. Chapter 4 summarize the results.

Chapter 2

Production and detection of antihydrogen beams

In this chapter, a production scheme of antihydrogen atoms by injection of antiprotons into confined positrons are explained. Antihydrogen atoms extracted to magnetic-field-free region is successfully observed at 2.7 m downstream from the production region.

2.1 Setup

Figure 2.1 shows a schematic view of the actual setup. Positrons are accumulated in a positron accumulator and transported to a single cusp trap via a positron transport line. Antiprotons are accumulated and cooled down in an antiproton trap, then they are injected into the positrons in the single cusp trap through an antiproton transport line. An antihydrogen detector is installed at the end of the spectrometer line.

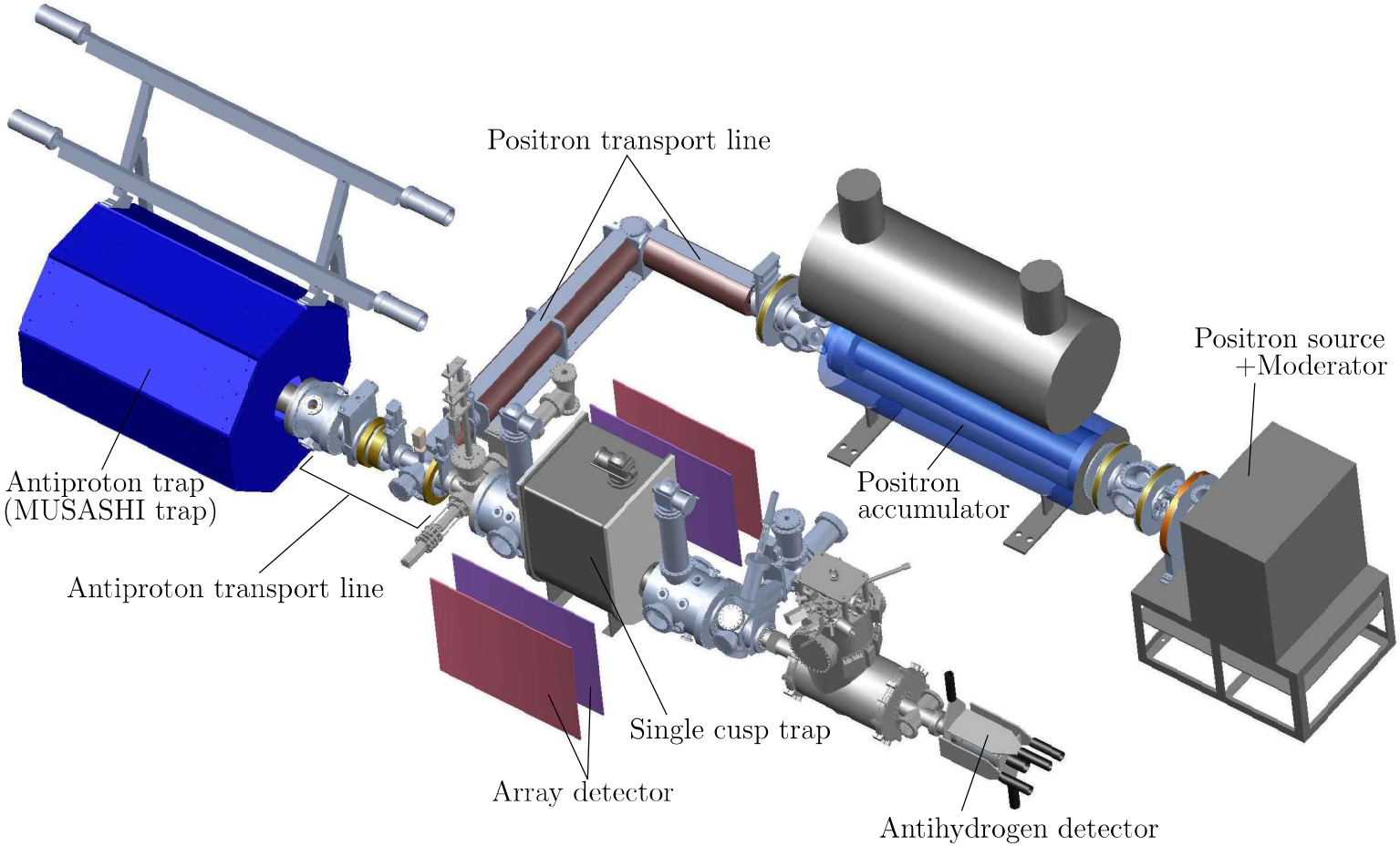

Figure 2.1: A schematic view of the experimental setup. Positrons are accumulated in a positron accumulator and transported to a single cusp trap via a positron transport line. Antiprotons are accumulated and cooled down in an antiproton trap, then they are injected into the positrons in the single cusp trap through an antiproton transport line. An antihydrogen detector is installed at the end of the spectrometer line.

2.1.1 MRE trap

The common setup for the positron accumulator, the antiproton trap, and the single cusp trap to confine non-neutral plasmas is explained as follows.

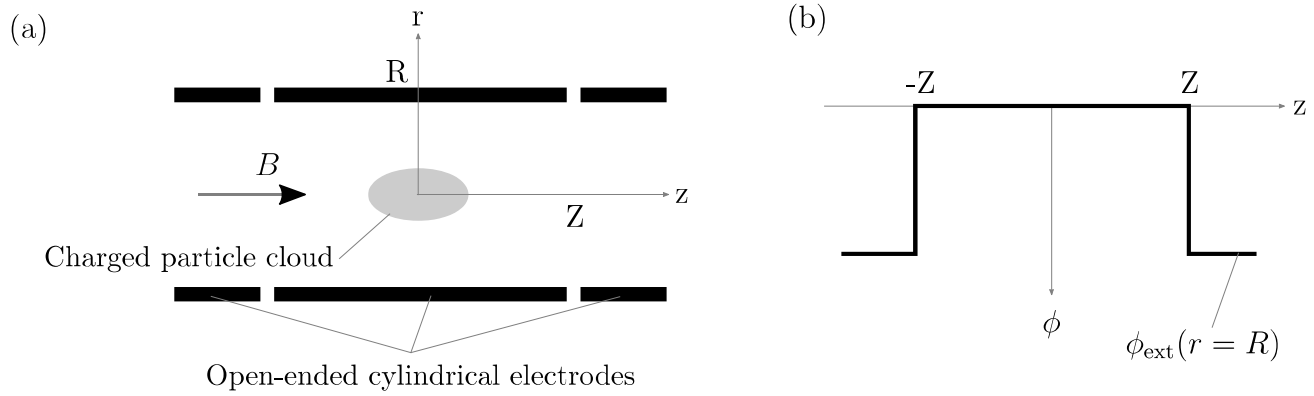

Figure 2.2: (a) A schematic diagram of the Penning-Malmberg trap. Three cylindrical electrodes with their radius of R produce a electrostatic potential well and a static magnetic field is applied along the axis. Charged particles are confined radially by the magnetic field and axially by the potential well. (b) Applied potential on the cylindrical electrodes.

Penning-Malmberg trap is widely used for confinement of charged particles. Fig. 2.2(a) shows a schematic diagram of an example of the Penning-Malmberg trap. A charged particle cloud is confined radially by a magnetic field B and axially by an electrostatic potential well $\phi_{\rm ext}$ produced by three open-ended cylindrical electrodes. Fig. 2.2(b) shows the applied potential on the electrodes. Focusing on one particle in a charged particle cloud, the electrostatic potential for the particle is shielded on the scale of Debye length λ_D. The Debye length is determined by the temperature T and density ρ of the cloud and given by

$$\lambda_D = \sqrt{\frac{\epsilon_0 k_B T}{q^2 \rho}}. \tag{2.1}$$

If the temperature is low and density is high for the charged particles, λ_D becomes small and each particle feels the electric field by the others as a whole. In this case, the charged particle cloud can be treated as a non-neutral plasma.

For a non-neutral plasma, Coulomb repulsive force each other exists due to the self electric field characterized by $\phi_{\rm self}$. The plasma rotates around the magnetic field axis so that the Lorentz force directing inward, centrifugal force directing outward, and the repulsive force outward balance each other in the equilibrium condition within the Penning-Malmberg trap. Assuming a non-neutral plasma as a cold fluid, a radial component of the equation of motion

is given by [40]

$$\frac{mv_\theta^2}{r} = q(E_r + v_\theta B) \tag{2.2}$$

where m is mass of a particle, $v_\theta = -\omega_r r$ is fluid velocity, q is charge of a particle, and E_r is given by

$$E_r = -\frac{\partial \phi}{\partial r} = -\frac{\partial}{\partial r}(\phi_{\text{ext}} + \phi_{\text{self}}). \tag{2.3}$$

When the rotation frequency is independent on r, it is called the rigid rotor equilibrium and the plasma density is given by [41]

$$\rho(r,z) = C \exp\left(-q\left(\frac{1}{2}m\omega_r\left(\frac{qB}{m} - \omega_r\right)r^2 + q\phi(r,z)\right)\frac{1}{k_B T}\right) \tag{2.4}$$

where the temperature is T and the plasma thermal pressure is assumed as $\rho k_B T$. Together with Poisson's equation, the density can be determined with given rotation frequency, temperature, total number, the equilibrium condition, and ϕ [42]. The density is uniform within a plasma and falls to zero quickly on the scale of Debye length at its surface if the plasma is sufficiently cold.

For a non-neutral plasma in a harmonic well expressed as

$$\phi_{\text{ext}} = A(r^2 - 2z^2) \tag{2.5}$$

in cylindrical coordinates (r, θ, z), the rigid-rotor equilibrium state in spheroidal shape is analytically derived. Multi-ring electrode (MRE) trap is capable for more stable confinement of non-neutral plasma without instabilities than normal Penning-Malmberg traps by realizing such harmonic potential well [43]. By carefully adjusting applied voltage on each electrodes, MRE trap is able to compensate self field by the plasma itself. Variations of MRE trap are utilized to our experiment.

2.1.2 Antiproton trap (MUSASHI)

This section explains about the structure of antiproton trap and preparations of antiprotons including supply from the AD of CERN, cooling, accumulation, radial compression, and extraction to the downstream side.

The antiproton trap is mainly composed of a superconducting solenoid and MRE as shown in Fig. 2.3(a). The magnetic field on beam axis is set at 2.5 T for this experiment and can be increased up to 5 T. The antiproton trap is named as the MUSASHI trap. MUSASHI stands for monoenergetic ultraslow antiproton beam source for high-precision investigation. The bore is cooled down to 5 K by Gifford-McMahon (GM) cryocoolers. The pressure $P_H = 10^{-10}$ mbar is measured at the downstream edge of the bore where it is at room temperature. However it is expected to be about 10^{-14} mbar where the temperature is $T \sim 5$ K, by considering the confinement lifetime of antiprotons in the trap $\tau_{conf} \sim 10^4$ s, using $P_H \sim 5.1 \times 10^{-11} T/\tau_{conf}$ [44]. The vacuum is isolated by two sheets of thin PET (polyethylene terephthalate) foil from the upstream side where a pressure is $\sim 10^{-9}$ mbar. The bore is heated up to typically ~ 50 K for 8 hours every day to reduce residual gas and keep the good vacuum. The foil works as a monitor to see a radial profile of injected beams. Cylindrical electrodes and a movable electron gun are prepared at downstream side which are used for transport and cooling of antiprotons, respectively (discussed later).

Figure 2.3(b) shows the schematic view of the MRE. The electrodes are made of oxygen free copper with their diameter of 4 cm. UCE and DCE electrodes are used for catching of fast antiprotons at ~ 10 keV. The other 10 electrodes are used to prepare a harmonic potential well by carefully adjusting applied voltages on each electrodes. One electrode named S is segmented azimuthally into four. Applied voltages on these ten electrodes can be operated between -100 V and 100 V in addition to the float voltage applied on the MRE as a whole which is capable up to 800 V. The MRE is cooled down via thermal contacts with the bore wall. Further details are described in [45].

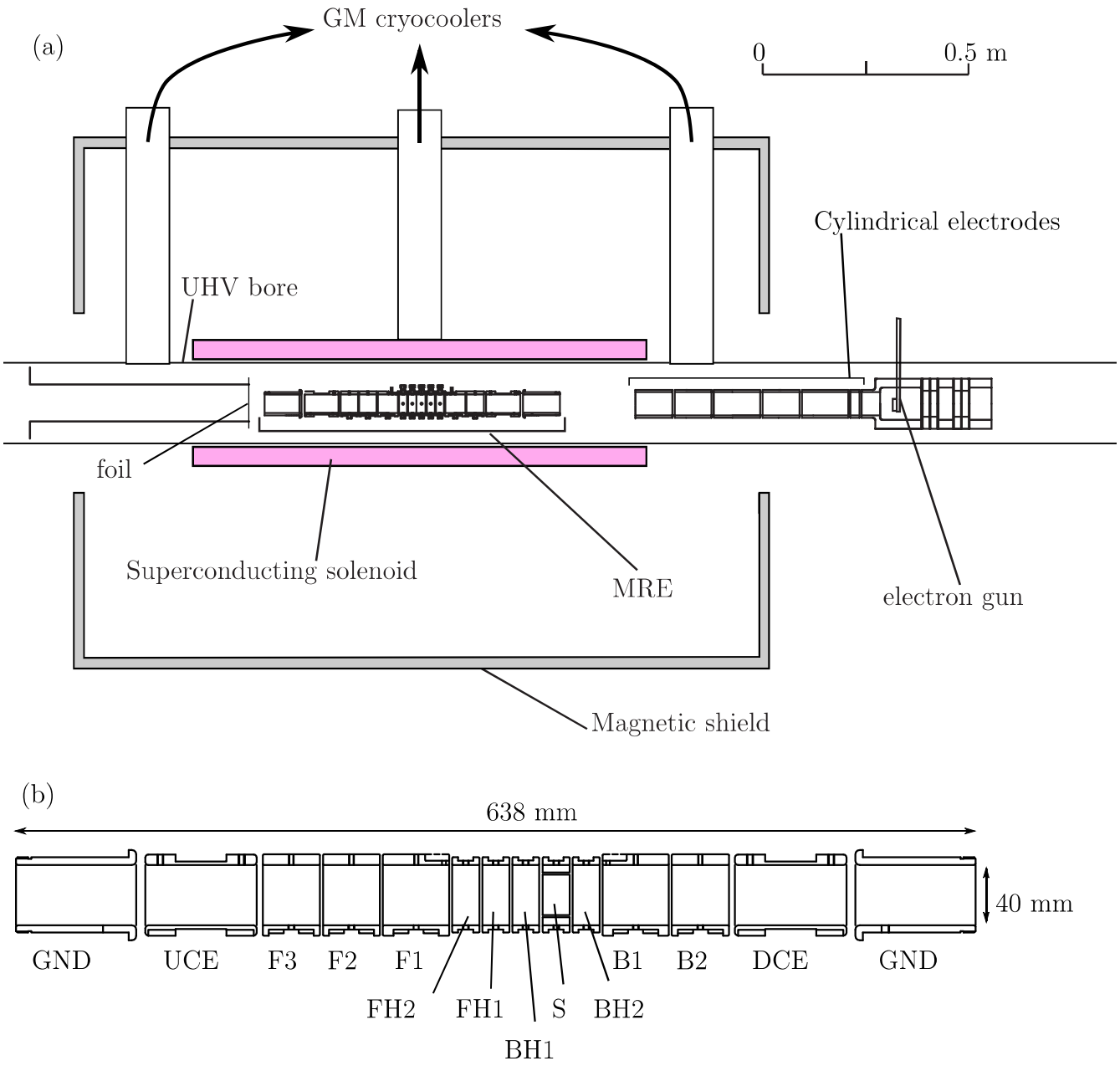

Figure 2.3: (a) A cross sectional view of the antiproton trap mainly composed of a superconducting solenoid and MRE. The magnetic field on beam axis is set at 2.5 T for this experiment. (b) A schematic drawing of the MRE. UCE and DCE are used for catching of fast antiprotons. The other 10 electrodes(F3-B2) are used to prepare a harmonic potential well by carefully adjusting applied voltages on each electrodes. One electrode named S is segmented azimuthally into four.

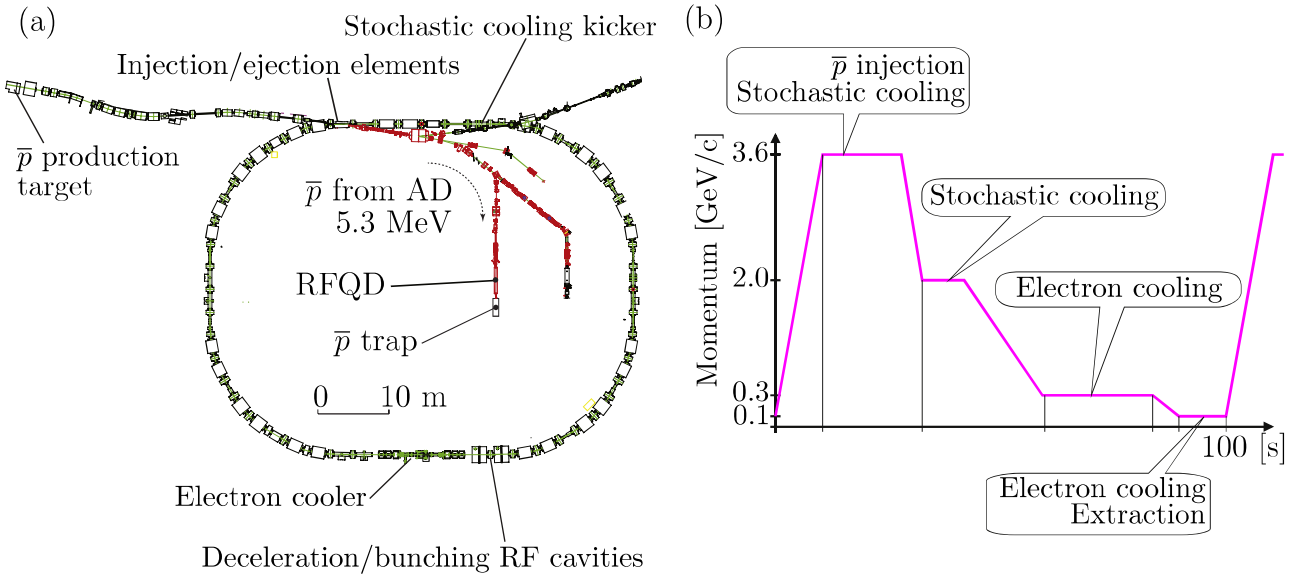

Figure 2.4: (a) A schematic drawing of the AD ring including the RFQD and the antiproton trap. (b) Typical machine cycle of the AD. Antiprotons are supplied every 2 minutes. Figures are adapted from [46].

Antiprotons are supplied from the Antiproton Decelerator (AD) of CERN. Figure 2.4(a) shows the schematic drawing of the AD. Since many components are arranged in a circle, it is called the AD ring. Protons are accelerated up to 26 GeV/c by the proton synchrotron of CERN in advance and injected onto an iridium target located at the most left-hand side of Fig. 2.4(a) to produce antiprotons. The produced antiprotons at 2.8 GeV are decelerated down to 5.3 MeV inside the AD ring. Figure 2.4(b) shows a typical machine cycle of the AD ring. In order to realize a low momentum spread, the antiprotons are cooled down by utilizing stochastic cooling technique at 3.5 GeV/c and 2 GeV/c followed by electron cooling at 300 MeV/c and 100 MeV/c [47]. Antiprotons at 5.3 MeV are supplied to the experimental area every 100 s. However, the energy is still too high for efficient antihydrogen production. ASACUSA collaboration has developed a radio frequency quadrupole decelerator (RFQD) with CERN by utilizing RF acceleration technique inversely [48]. The antiprotons are decelerated down to 100 keV by RFQD and injected into the antiproton trap penetrating through the foil. The foil decelerates antiprotons further down to 10 keV. Because of the sequential combination of the AD, the RFQD, and the thin PET foil, more antiprotons by a factor of 10 are available compared with other collaborations in the AD.

The injected antiprotons at 10 keV should be cooled down. In general, charged particles are cooled down via cyclotron radiation in a strong magnetic field. According to Larmor formula, the energy loss rate can be given by [49]

$$\frac{dE_\perp}{dt} = -\frac{e^2}{6\pi\epsilon_0 c^3}(\Omega v_\perp)^2 = -\frac{e^2(eB/m)^2}{3\pi\epsilon_0 mc^3}E_\perp = -\tau_{\rm rad}^{-1}E_\perp \tag{2.6}$$

where $v_\perp$ is the velocity perpendicular to the magnetic field, $E_\perp$ is the kinetic energy given by $E_\perp = mv_\perp^2/2$, and $\Omega = qB/m$ is the cyclotron frequency. Electrons in 2.5 T are cooled with the time constant $\tau_{\rm rad} \sim 0.4$ s, while the time constant for antiprotons is much longer by a factor of $(m_{\overline{p}}/m_{e^-})^3 \sim 1800^3$. In order to cool down antiprotons efficiently, electrons are used. Antiprotons lose energy via collisions with electrons and electrons are cooled down by the cyclotron radiation.

Therefore electrons are prepared in the MUSASHI trap prior to injection of antiprotons from the RFQD. Figure 2.5 shows electrostatic potential configurations on axis as a function of axial positions during the preparation of electrons. Electrons are injected at ~ 60 eV from the electron gun located at downstream of the MUSASHI trap into $\phi_{\rm e^-inj}$ by lowering the potential barrier at the downstream side and then $\phi_{\rm e^-inj}$ is changed into $\phi_{\rm e^-}$ which is more harmonic for a stable confinement.

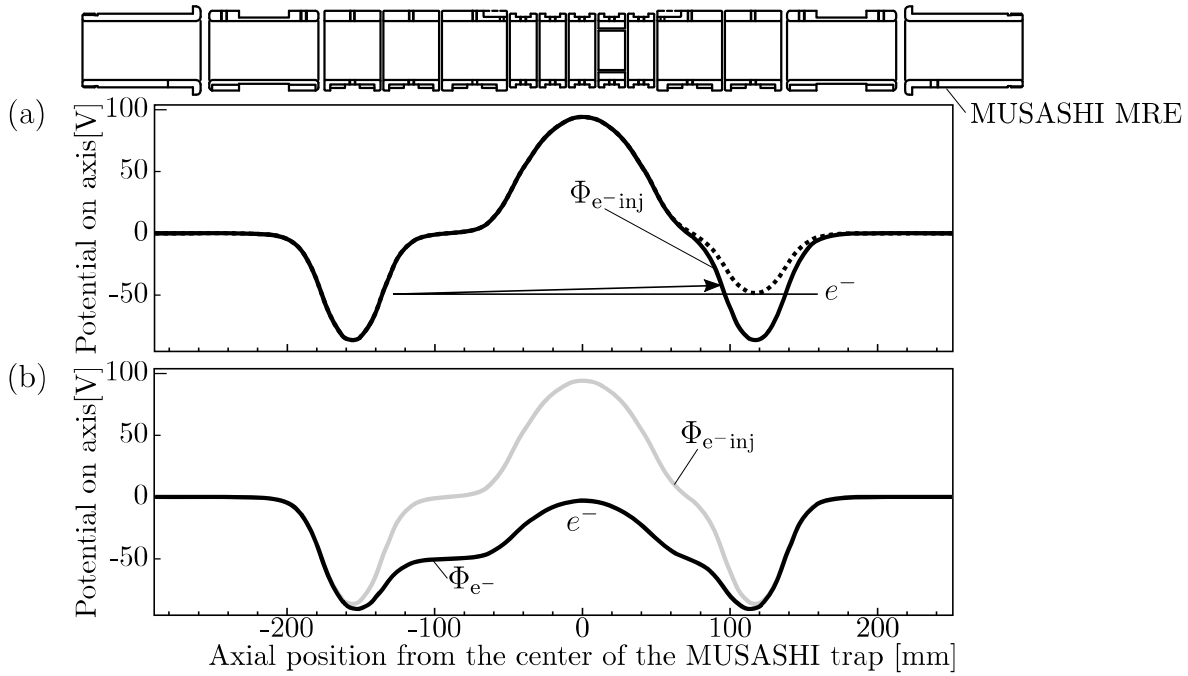

Figure 2.5: Electrostatic potentials on axis as a function of axial positions for preparation of electrons in the MUSASHI trap. Electrons are injected at ~ 60 eV from the downstream of the MUSASHI trap into $\phi_{\rm e^-inj}$ by lowering the potential barrier at the downstream side and then $\phi_{\rm e^-inj}$ is changed into $\phi_{\rm e^-}$ which is more harmonic for a stable confinement.

Radial overlap between electrons and injected antiprotons should be increased for effective cooling. The radial distribution of a non-neutral plasma can be controlled by applying torque on the plasma (rotating-wall technique). When the torque is applied on a plasma and the rotation speed is increased(decreased), the radius gets smaller(larger) in order to conserve the total angular momentum P_θ given by

$$P_\theta = \sum_{i=1}^{N} p_{\theta i}(t) = \int d^3r d^3v f(\mathbf{r}, \mathbf{v}, t)(mv_\theta r + qBr^2/2) \tag{2.7}$$

where p_θ is the θ component of the canonical angular momentum for a particle in a uniform magnetic field [40]. The segmented electrode is used for this technique. Figure 2.6 shows equipotential lines produced by applying a sinusoidal potential with a phase difference on azimuthally segmented electrodes. The applied voltages and equipotential lines are shown every 1/4 period of the sinusoidal wave.

The electron cloud confined in the potential configuration ϕ_{e^-} is radially expanded by the rotating-wall technique.

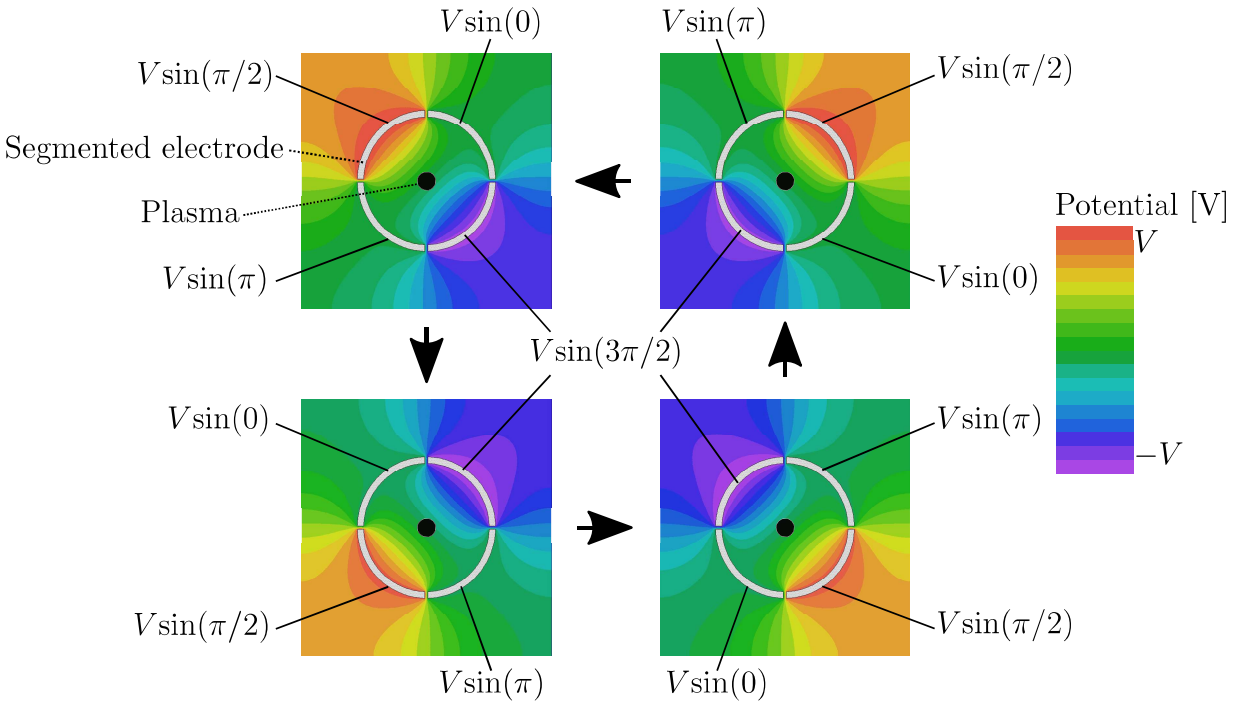

Figure 2.6: A schematic diagram of the rotating-wall electric field by four segmented electrodes. Colored filled contour plot shows the electrostatic potential (radial profile, perpendicular to the magnetic field). The applied voltages on each segmented electrode are shown. Each of 4 squares corresponds to a snapshot at every 1/4 period of one cycle.

After electrons are prepared for effective cooling of antiprotons at the center, a potential barrier at -12 kV is prepared using DCE electrode for catching of antiprotons. Antiprotons are injected from the upstream side through the foil at $\sim$ 10 keV, pass UCE electrode, and are reflected by the potential barrier at DCE as shown in Fig. 2.7(a). Another potential barrier is prepared using UCE electrode before reflected antiprotons are gone away from the trapping region as shown in Fig. 2.7(b). The time constant of the switching to apply -12 kV on UCE electrode is $\sim$ 300 ns [50]. Both potential barriers at DCE and UCE are kept for 40 s. Trapped antiprotons are cooled by coexisting electrons. Then both potential barriers at -12 kV are removed to release uncooled antiprotons, while cooled antiprotons and electrons are kept trapped in the harmonic potential well ϕ_{e^-} at the center. This cycle is repeated typically for 4 times ($\sim$ 10 minutes).

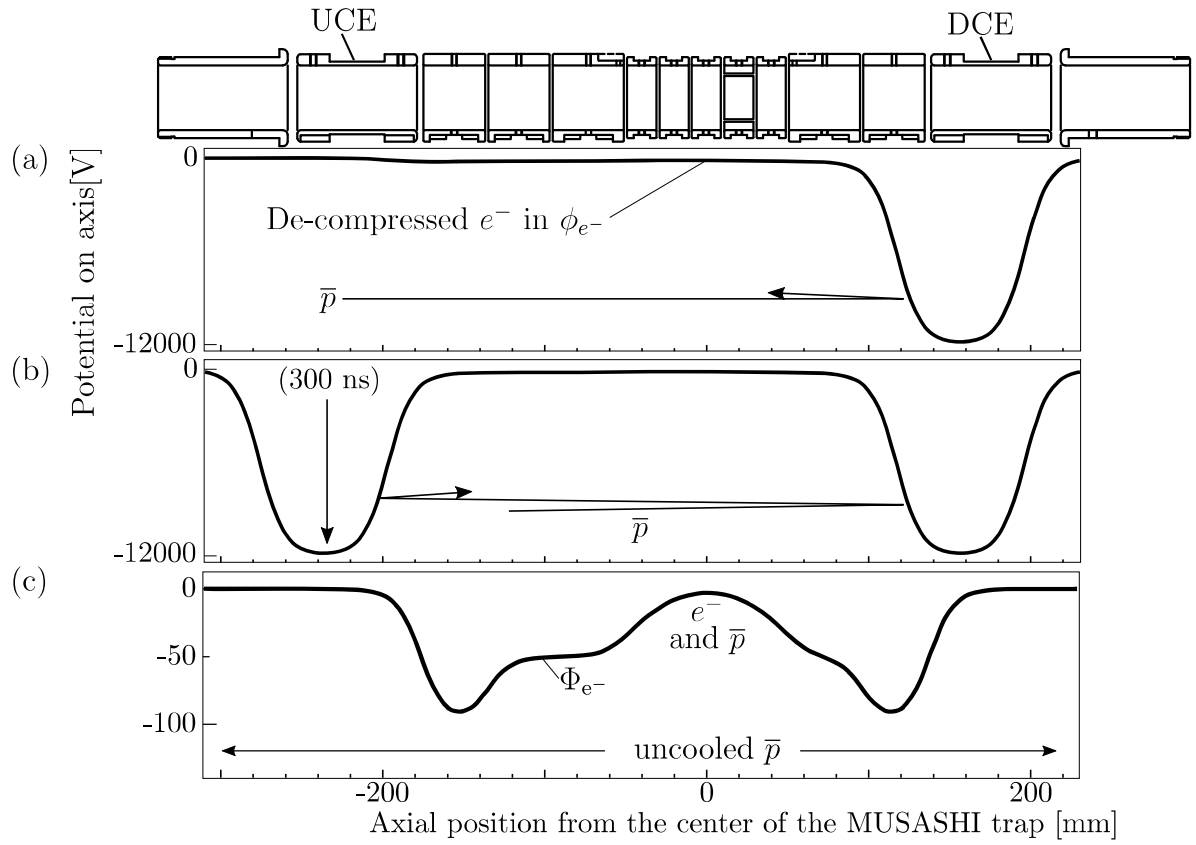

Figure 2.7: Potential configurations for catching of injected fast antiprotons in the MUSASHI trap. (a) After electrons are prepared for effective cooling of antiprotons at the center, a potential barrier at -12 kV is prepared using DCE electrode, antiprotons are injected from the upstream side at $\sim$ 10 keV, pass UCE electrode, and are reflected by the potential barrier at DCE. (b) Another potential barrier is prepared using UCE electrode before reflected antiprotons are gone away from the trapping region and both potential barriers at DCE and UCE are kept for 40 s. Trapped antiprotons are cooled by coexisting electrons. (c) Potential barriers at -12 kV are removed to release uncooled antiprotons, while cooled antiprotons and electrons are kept trapped in the harmonic potential well at the center.

Antiprotons should be radially compressed for a higher transport efficiency to the downstream by applying rotating-wall technique. In order to compress antiproton cloud effectively, the remained electrons coexist with antiprotons are kicked out from the MUSASHI trap in advance. Figure 2.8(a) shows that the potential barrier at the upstream side is shortened (black solid line), the barrier is removed only for a short time of 500 ns (dotted line), and then the potential configuration is quickly switched back (black solid line). If antiprotons and electrons have the same kinetic energy, the velocity is lower by a factor of 40 because antiprotons are heavier than electrons by a factor of 1800. Therefore only faster electrons are released and slower antiprotons are still trapped, which is called electron kickout.

After the electron kickout, the potential configuration is changed into a confinement well $\phi_{\mathrm{confinement}}$ as shown in Fig. 2.8(b) for a stable confinement. The rotating-wall electric field is applied to radially compress the antiproton cloud in $\phi_{\mathrm{confinement}}$. The radial compression of antiprotons are reported in [51][52].

Figure 2.8(c) shows potential configurations to extract antiprotons to the downstream side. The confinement region is shortened first to minimize the bunch length (dotted line) and then a negative pulsed voltage is applied to remove the potential barrier at downstream of the potential well (black solid line). This scheme contributes to a higher catching efficiency at the single cusp trap at the downstream side. The extraction energy of antiprotons from the MUSASHI trap can be changed simply by changing the float voltage applied on the MRE as a whole. The float voltage is -150 V for the potential configurations shown in Fig. 2.8(c).

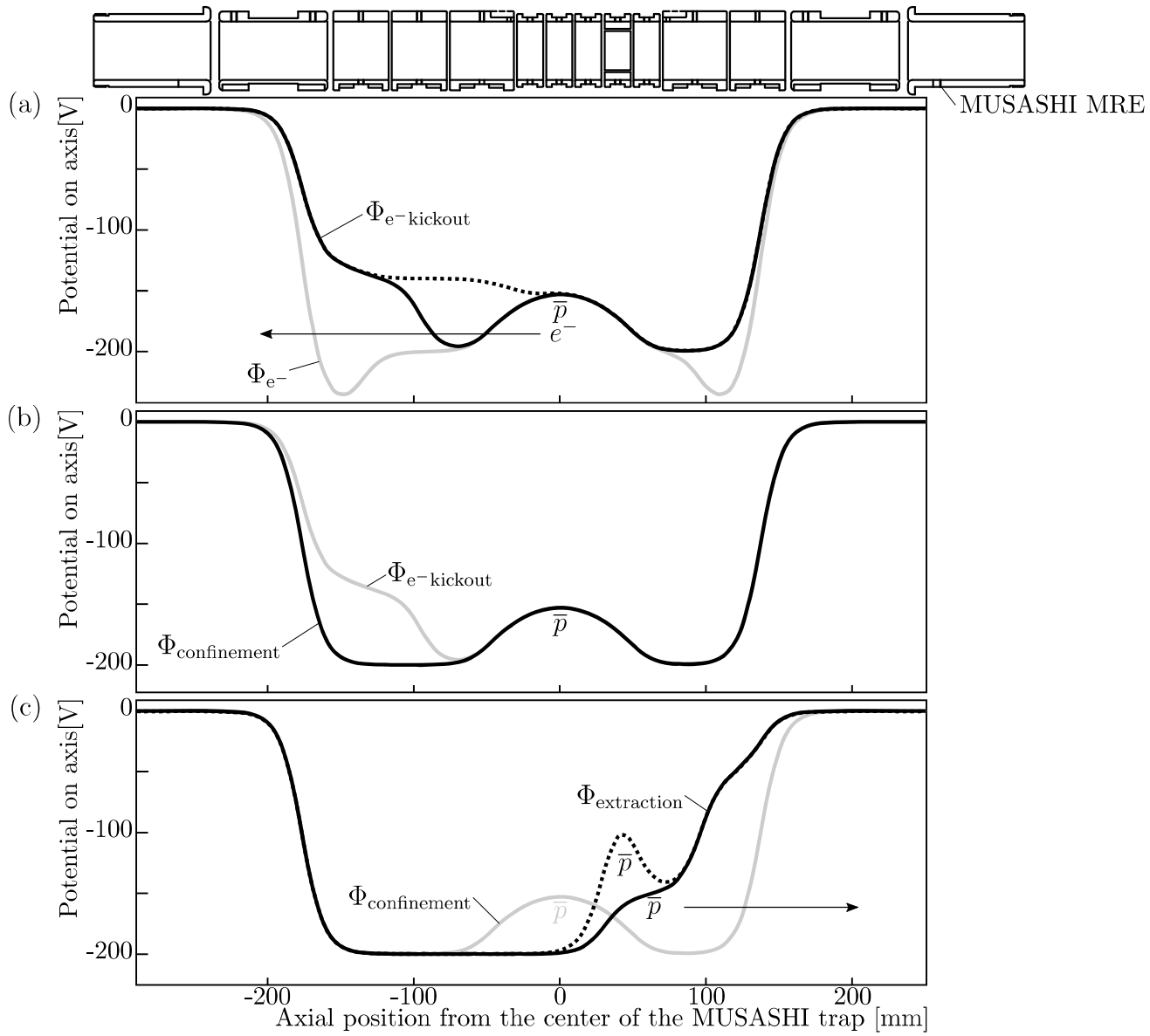

Figure 2.8: (a) Potential configurations for electron kickout to compress antiproton cloud effectively. The potential barrier at the upstream side is shortened (black solid line), the barrier is removed only for a short time of 500 ns (dotted line), and then the potential configuration is quickly switched back (black solid line). (b) After the electron kickout, the potential configuration is changed into a confinement well $\phi_{\text{confinement}}$. The rotating-wall electric field is applied to radially compress the antiproton cloud in $\phi_{\text{confinement}}$. (c) Potential configurations to extract antiprotons to the downstream side. The confinement region is shortened first to minimize the bunch length (dotted line) and then a negative pulsed voltage is applied to remove the potential barrier at downstream of the potential well (black solid line). The extraction energy of antiprotons from the MUSASHI trap can be changed simply by changing the float voltage applied on the MRE as a whole (-150 V in this case).

2.1.3 Antiproton transport line

The extracted antiprotons from the MUSASHI trap are transported to the single cusp trap through the antiproton transport line. This section explains basic ideas of transport of charged particles first, and then the actual setup of the antiproton transport line is described. Calculated trajectories of antiprotons through the transport line are shown.

In order to transport antiprotons at relatively low energy without loss due to annihilations with surrounding materials, trajectories of antiprotons should be focused. In general, trajectories of charged particles are affected by Lorentz force $q(E + v \times B)$. Figure 2.9(a) shows an example. Trajectories of antiprotons are focused by one type of the electrostatic lens, called Einzel lens. Einzel lens is composed of three cylindrical electrodes and widely used for focusing of charged particle beams. An electrostatic potential is applied on an electrode and two electrodes at both sides are grounded. The equipotential lines are shown together. Figure 2.9(b) shows another example. Trajectories of antiprotons are focused by the coaxial transport coil along the beam axis. The magnetic field lines are shown together. The antiproton transport line is mainly composed of these components.

Figure 2.10 shows a schematic drawing of the actual setup of the antiproton transport line. The cylindrical electrodes are placed at the exit of the MUSASHI trap and two coaxial transport coils are placed along the transport line. The transport coils are named coil A and coil B, respectively. The cylindrical electrodes work as Einzel lens by applying 400 V on the electrodes shown by colored square. They are made of aluminum. Transport coil A and B are composed of aluminum wire with 150 turns and fixed with support structure on the duct. The magnetic field on axis is ~ 0.012 T for both transport coils.

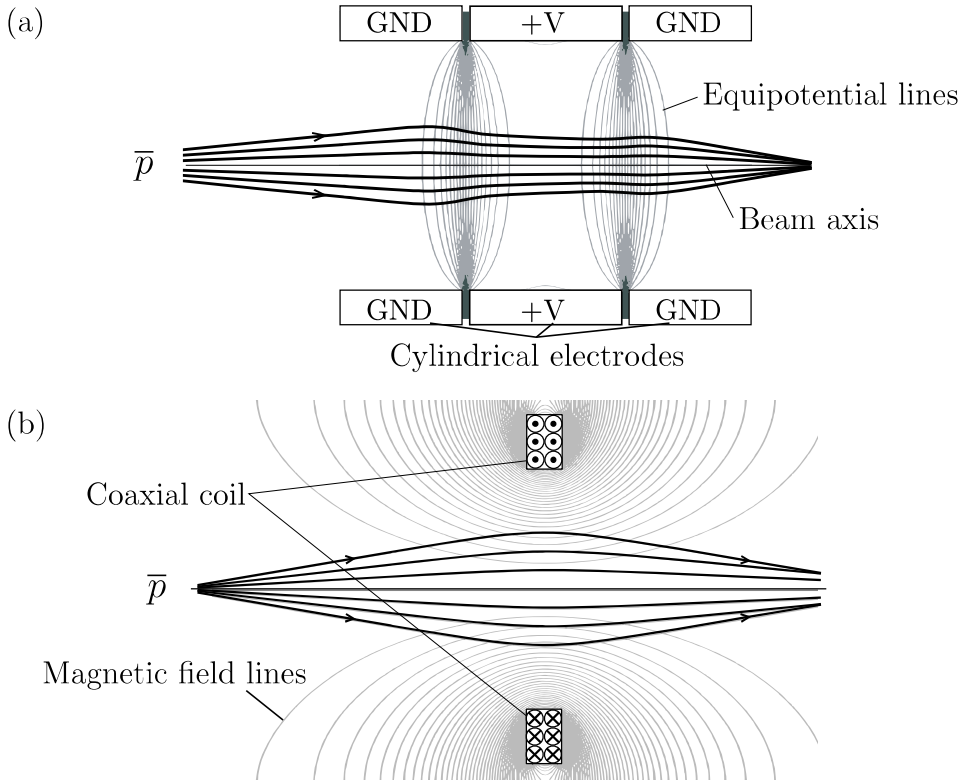

Figure 2.9: Schematic figures of trajectories of antiprotons with focusing elements. (a) Trajectories of antiprotons are focused by Einzel lens, which is composed of three cylindrical electrodes. An electrostatic potential is applied on an electrode and two electrodes at both sides are grounded. The equipotential lines are shown together. (b) Trajectories of antiprotons are focused by the coaxial transport coils along the beam axis. The magnetic field lines are shown together.

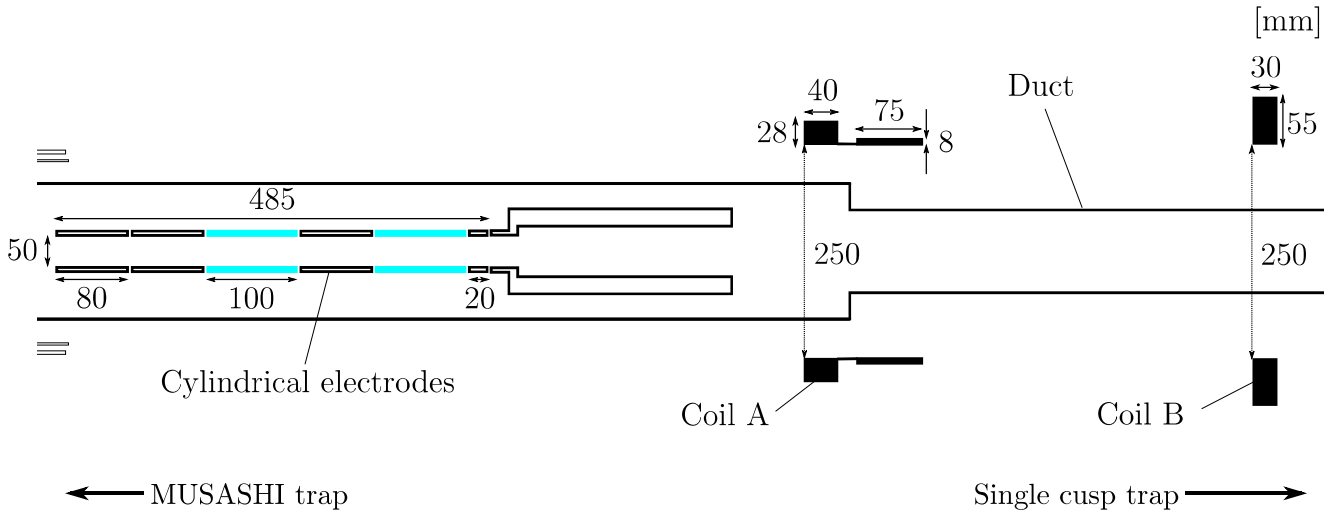

Figure 2.10: A schematic drawing of the actual setup of the antiproton transport line including the cylindrical electrodes and two coaxial transport coils named coil A and coil B, respectively. The cylindrical electrodes work as Einzel lens by applying 400 V on the electrodes shown by colored square. The magnetic field strength on axis is ~ 0.012 T for both transport coils.

Figure 2.11 shows calculated trajectories of antiprotons at 150 eV through the antiproton transport line shown on top. Filled regions show axial positions of the Einzel lens (cylindrical electrodes), coil A, and coil B. A commercial software called Tricomp (by Field Precision LLC) including trak 8.0, mesh 8.0, estat 8.0, and permag 8.0 is used for the calculations. The Tricomp mesh, estat, and permag calculate two dimensional static electric and magnetic fields by finite element method. A trajectory of a charged particle is given by Tricomp trak under the calculated static electric and magnetic field. In the calculation shown in Fig. 2.11, the initial radial positions of antiprotons are assumed to be less than 4 mm every 0.2 mm and the initial radial momentum are assumed to be zero. Interactions between charged particles are ignored. While the trajectories diverge as the magnetic field becomes weak outside of the MUSASHI trap, they are focused by the Einzel lens (cylindrical electrodes). The trajectories are also weakly focused by two transport coils at downstream side. The radial positions approach to the axis again near the single cusp trap because the magnetic field becomes strong.

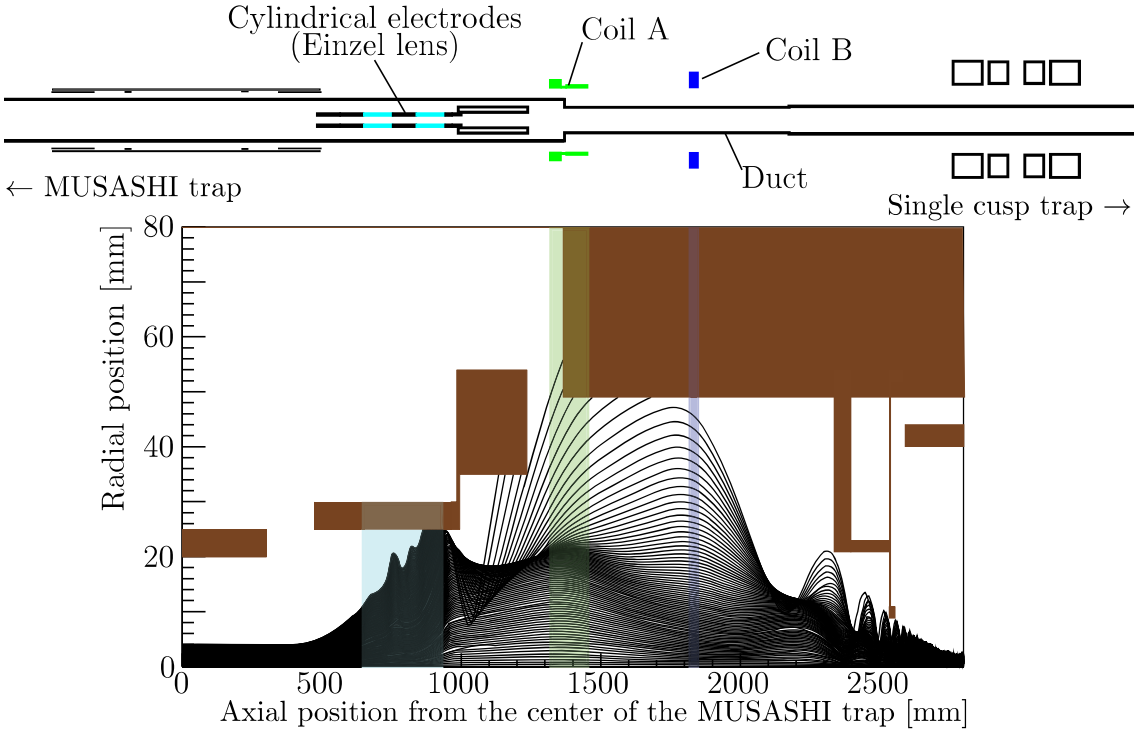

Figure 2.11: Calculated trajectories of antiprotons at 150 eV using the commercial software called Tricomp (by Field Precision LLC). Two dimensional static electric and magnetic fields are calculated by finite element method for the antiproton transport line shown on top, and then trajectories are calculated under the static field. The initial radial positions of antiprotons are assumed to be less than 4 mm every 0.2 mm and the initial radial momentum are assumed to be zero. Filled region shows axial position of the Einzel lens (cylindrical electrodes), coil A, and coil B. While the trajectories diverge as the magnetic field becomes weak outside of the MUSASHI trap, they are focused by the Einzel lens and two transport coils. The radial positions approach to the axis again near the single cusp trap because the magnetic field becomes strong.

2.1.4 Positron accumulator

This section explains about preparation of positrons including moderation of positrons by solid Ne and buffer-gas cooling in the positron accumulator.

Figure 2.12(a) shows a schematic drawing of the positron source and positron accumulator which is composed of a N_2 gas cell and MRE, named positron-MRE, inside a superconducting solenoid at 0.6 T on axis. The magnet is cooled down by liquid helium down to 5 K. The bore is also cooled down by circulating the helium through surrounding cooling loop down to 100 K.

Positrons are supplied from ^{22}Na source through β^+ decay with its half-life of 2.6 years, $^{22}\mathrm{Na} \rightarrow ^{22}\mathrm{Ne} + e^+ + \nu_e$. However, the emitted positrons have a large energy spread up to ~ 500 keV because ν_e carries part of the energy.

The large energy spread is not appropriate for trapping. Solid Ne is used as a moderator to make the energy spread smaller. Figure 2.12(b) shows a schematic diagram of the moderation. The positron source is contained in a source holder made of copper. It has a conical aperture in front of the ^{22}Na source. By cooling the holder down to 7.5 K in Ne atmosphere, solid Ne is created on the surface of the holder. The emitted positrons are injected into solid Ne and lose energy quickly through ionizing collisions. Considering a wide band gap $E_g = 21.5$ eV for solid Ne, the positronium binding energy in the solid E_b, and the work function ϕ_+, the phonon excitation is the only process to lose energy further when the energy is lower than 16 eV ($= E_g - E_b - \phi_+$) and then positrons are very likely to be re-emitted from the surface [53]. A moderation efficiency is $\sim 10^{-2}$ which is the highest value among various materials. The energy spread of the re-emitted positrons is small at a few eV for a combination of ^{22}Na source and solid Ne [53]. In order to extract the moderated positrons with the energy spread of a few eV from the moderator to the downstream side, they are accelerated up to the energy determined by applied voltage on the bias electrode.

The positrons are injected into the positron accumulator. Figure 2.12(c) shows the pressure and the electrostatic potential configuration on axis as a function of axial positions in the positron accumulator. The gas cell is composed of four parts (G1 - G4) and N_2 gas is supplied and evacuated continuously. The pressure can be variated depending on the position by different conductances for the evacuation. The injected positrons lose energies inside the gas cell mainly through the electronic excitation of nitrogen molecules with its threshold at 7 eV. The pressure near the source is set as high as 10^{-2} mbar to increase collisions, while the pressure at the other side of the trap is as low as 10^{-6} mbar for slow positrons to suppress annihilations [54].

An averaged energy loss is approximately 9 eV per collision and it competes with positronium formation. In consequence, positrons are trapped in the electrostatic potential well prepared by the positron-MRE with a magnetic field by the superconducting solenoid. This method is called buffer-gas cooling.

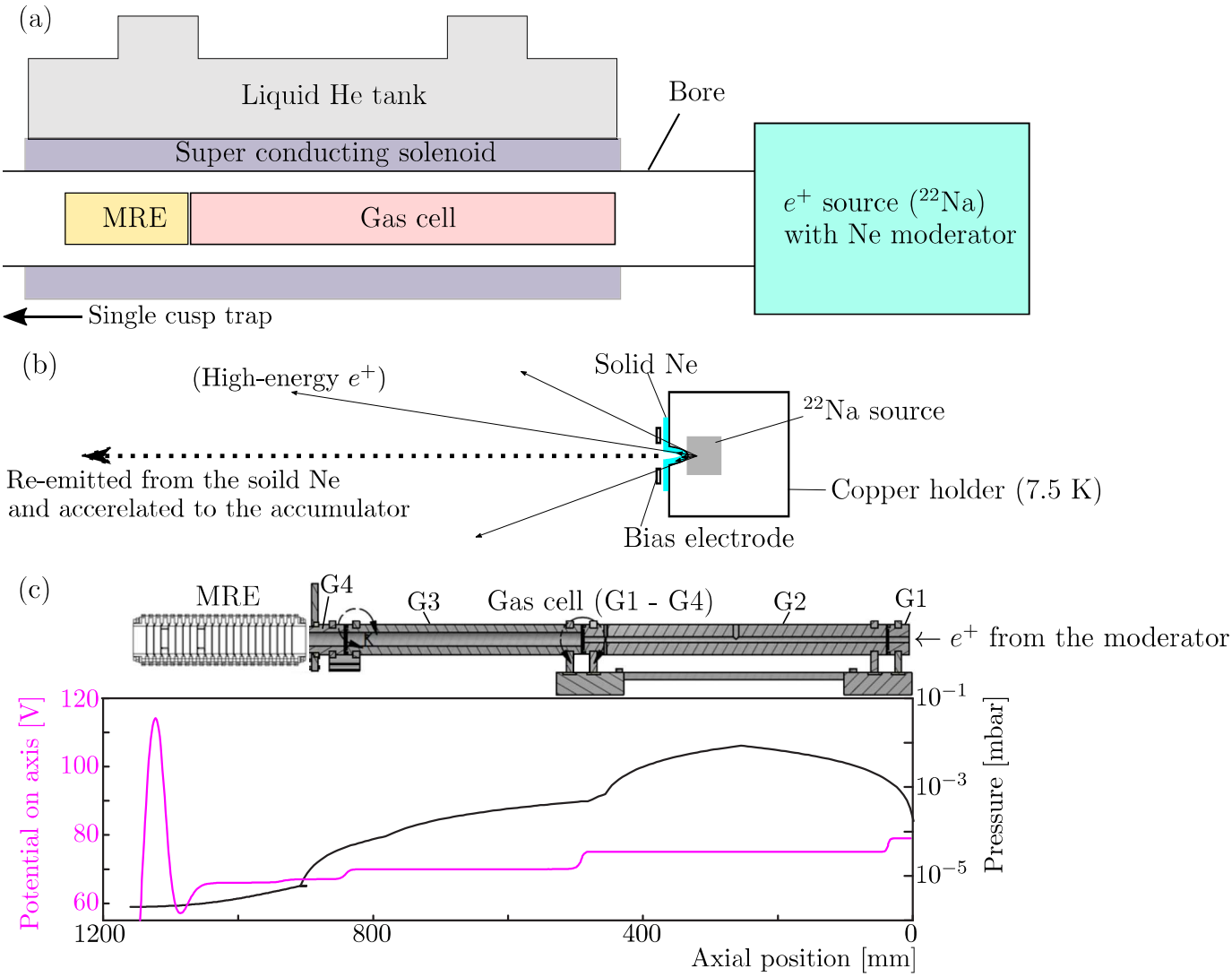

Figure 2.12: (a) A schematic drawing of the positron source and positron accumulator including the N_2 gas cell, positron-MRE, and superconducting solenoid. (b) A schematic diagram of the moderation of positrons. The emitted positrons from the source are injected into solid Ne and lose energy through collisions. When the energy is so low that the phonon excitation is the only process to lose energy further, positrons are re-emitted from the surface. (c) The pressure and typical electrostatic potential configuration on axis in the positron accumulator. The injected positrons lose energies inside the gas cell mainly through the electronic excitation of nitrogen molecules. In consequence, positrons are trapped in the electrostatic potential well of the positron-MRE with a magnetic field by the superconducting solenoid.

2.1.5 Single cusp trap

This section explains about the structure of the single cusp trap, where antihydrogen atoms are produced, including its magnetic field configuration to extract the spin-polarized antihydrogen atoms.

The single cusp trap is mainly composed of the superconducting anti-Helmholtz coils and MRE, named scusp-MRE. Figure 2.13(a) shows a cross sectional view of the single cusp trap. The cold bore is cooled down to ~ 6 K.

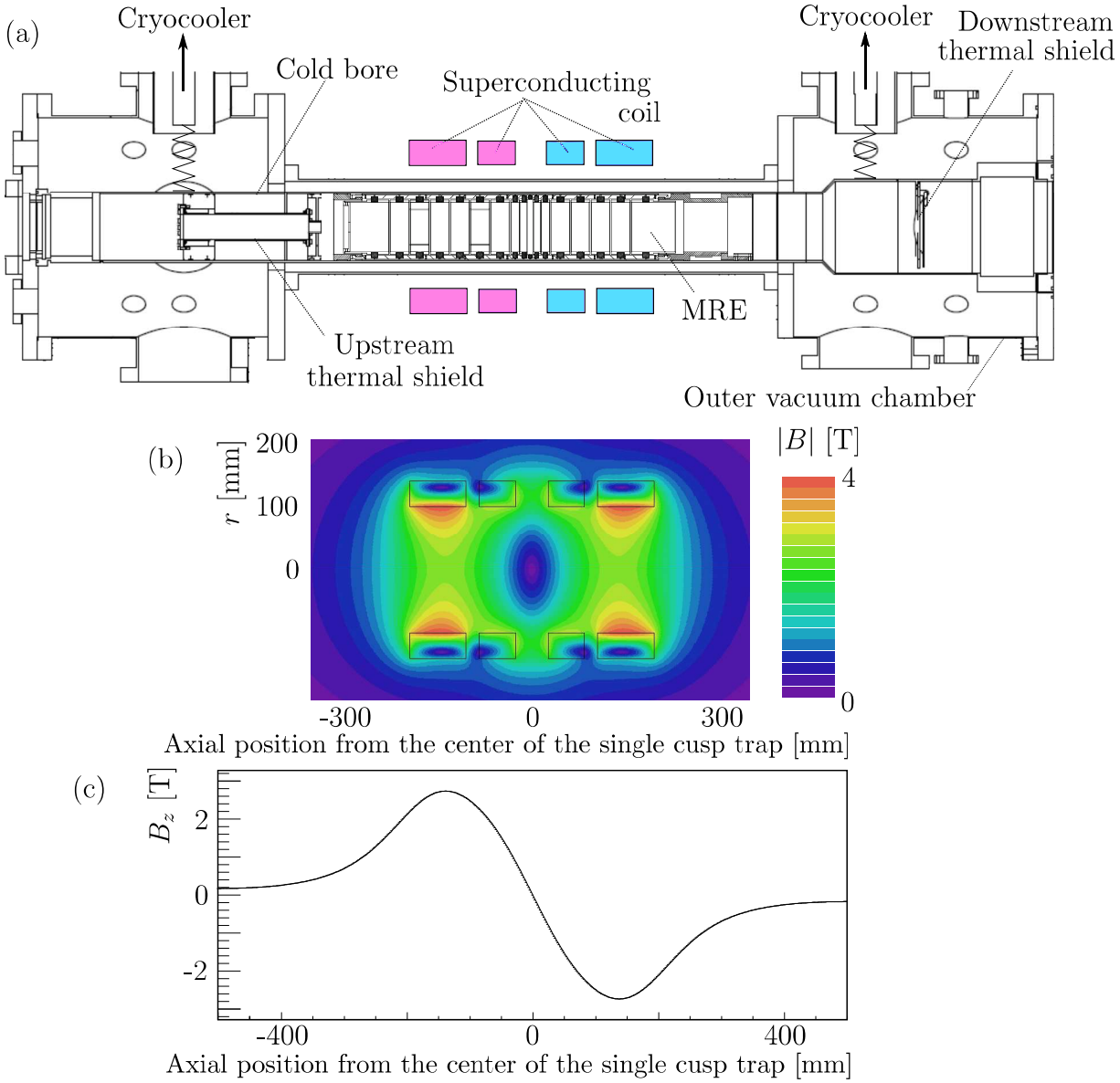

Figure 2.13: (a) A cross sectional view of the single cusp trap including the superconducting anti-Helmholtz coils (single cusp magnet), scusp-MRE, cold bore, thermal shields, and outer vacuum chamber. The cold bore is cooled down to ~ 6 K. (b) The two dimensional magnetic field distribution of the single cusp magnet ($|B| = 0$ at the center). It satisfies $\partial|B|/\partial r > 0$. (c) The magnetic field distribution along the axis of the single cusp magnet.

Anti-Helmholtz coil is a pair of coils with flowing current in opposite directions. Fig. 2.13(b) shows a two dimensional magnetic field distribution provided by a combination of the anti-Helmholtz coils. It satisfies $\partial|B|/\partial r > 0$. There is a zero-magnetic field point at the center ($z = 0$ and $r = 0$). Figure 2.13(c) shows the magnetic field distribution along the axis. The force acting on an antihydrogen atom with its magnetic moment of $\boldsymbol{\mu}$ is given by

$$\nabla(\boldsymbol{\mu} \cdot \boldsymbol{B}) = \begin{cases} +\mu\nabla|\boldsymbol{B}| \text{ (high-field seekers)} \\ -\mu\nabla|\boldsymbol{B}| \text{ (low-field seekers)} \end{cases} \tag{2.8}$$

because the magnetic moment is parallel to the magnetic field for high-field seekers and anti-parallel for low-field seekers as described before. Therefore low-field seekers are focused along the axis while high-field seekers are defocused away from the axis.

With this focusing and defocusing effects, Fig. 2.14(a) and (b) show calculated trajectories of ground-state antihydrogen atoms at 10 K for low-field seekers and high-field seekers, respectively [55]. In the calculation, antihydrogen atoms are assumed to be produced isotropically at the point of maximum magnetic field on axis shown by open circles, the magnetic moment is constant and Majorana spin-flip is ignored which is estimated to be negligibly small for our experimental condition [55]. Trajectories are shown every two degrees. It clearly shows that the transported fraction of low-field seekers at $z \sim 1.5$ m (f_{LFS}) is higher than that of high-field seekers (f_{HFS}). The spin-polarization of antihydrogen beams can be defined by $(f_{\mathrm{LFS}} - f_{\mathrm{HFS}})/(f_{\mathrm{LFS}} + f_{\mathrm{HFS}})$. Figure 2.14(c) shows the calculated polarization as a function of the kinetic energy of antihydrogen atoms when the production position is 16 cm upstream from the center of the single cusp trap [55]. The higher spin-polarization is achieved as the kinetic energy of antihydrogen atoms becomes small.

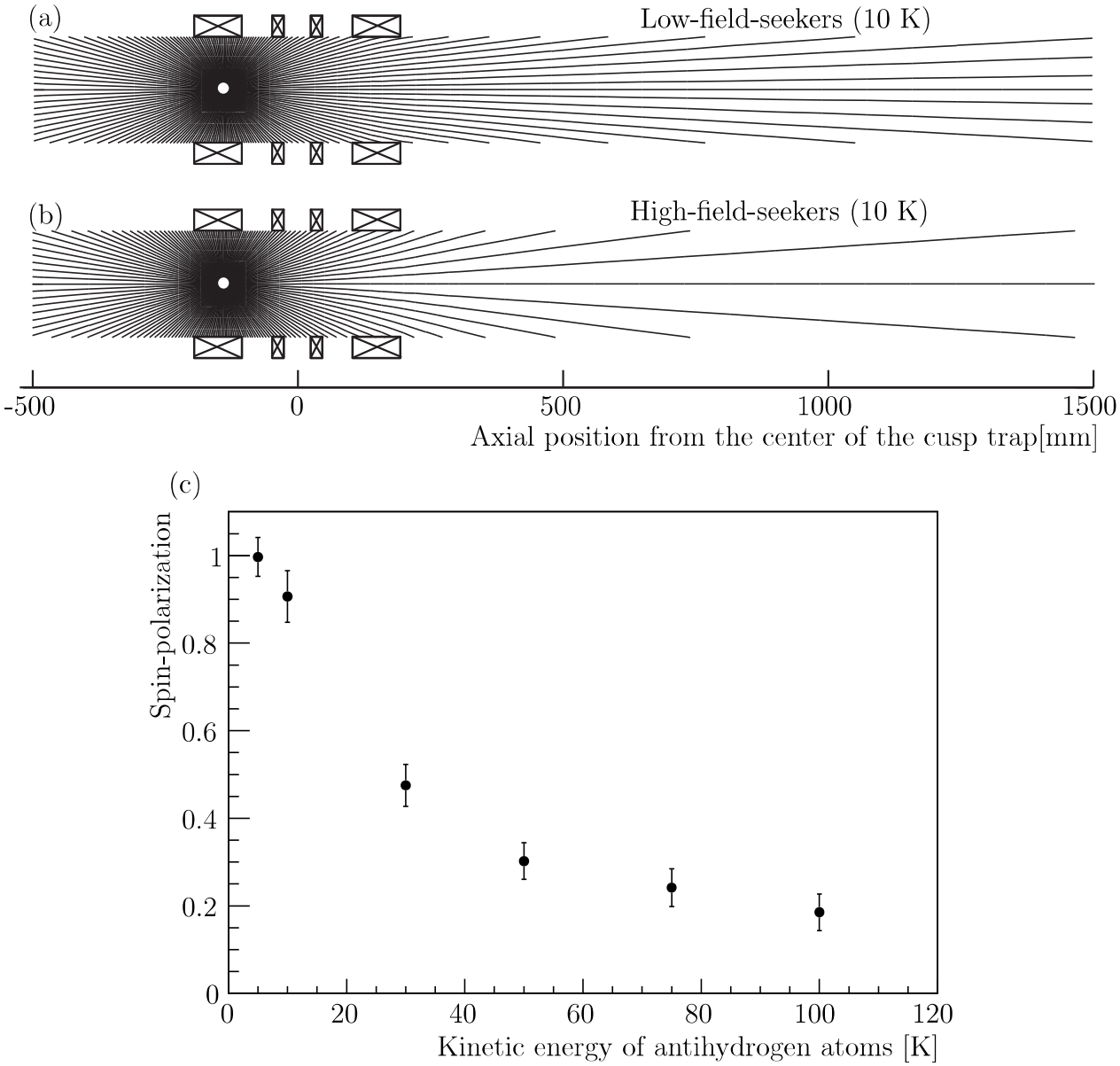

Figure 2.14: (a) Calculated trajectories of ground-state antihydrogen atoms of low-field seekers (focused). (b) Calculated trajectories of ground-state antihydrogen atoms of high-field seekers (defocused). (c) The calculated spin-polarization as a function of the kinetic energy of antihydrogen atoms. The higher spin-polarization is achieved as the kinetic energy of antihydrogen atoms becomes low. In the calculation, antihydrogen atoms are assumed to be produced isotropically at the point of maximum magnetic field on axis shown by open circles, the magnetic moment is constant and Majorana spin-flip is ignored which is estimated to be negligibly small for our experimental condition. These figures are adapted from [55].

The scusp-MRE is composed of 17 cylindrical electrodes named U9 - U1, CE, D1 - D7 from upstream to downstream. They are made of gold-plated aluminum. U7 and U4 are segmented azimuthally into four. The radius is larger than that of the antiproton trap by a factor of two for a larger solid angle viewed from produced antihydrogen beams inside the scusp-MRE. The scusp-MRE is cooled down to $\sim$ 15 K via thermal contact with the cold bore. Typical pressure can be estimated at $\sim 10^{-12}$ mbar considering the confinement time of antiprotons of $\sim$ 1000 s. Electronic filters both at cryogenic temperature and at room temperature to reduce electric noise are connected to the scusp-MRE.

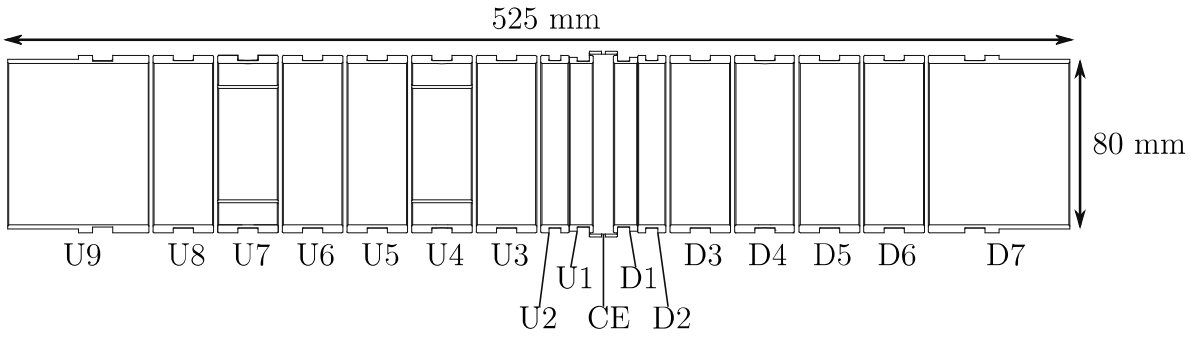

Figure 2.15: A schematic drawing of the scusp-MRE. U7 and U4 electrodes are segmented azimuthally into four.

Thermal shields both at upstream and downstream side of the single cusp trap are placed to reduce thermal radiation from the room temperature. Figure 2.16 shows the downstream thermal shield which is movable and opened for efficient evacuation and extraction of antihydrogen atoms to the downstream side.

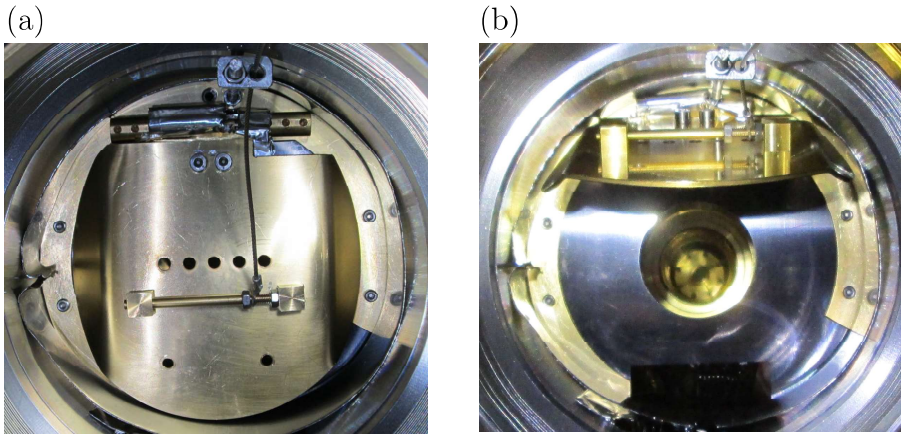

Figure 2.16: Pictures of the downstream thermal shield (views from downstream) when it is closed (a) and opened (b).

Further details of the single cusp trap are described in [56].

2.1.6 The array detector

This section explains about the array detector next to the single cusp trap including detection of antiprotons in general.

Antiprotons are usually detected by annihilations with nucleons. In order to monitor annihilations inside the single cusp trap, four arrays of plastic scintillator bars are placed along the beam axis at both sides of the single cusp trap. Figure 2.17(a) shows a schematic view of the array detector. Inner array 1, 2 are composed of 30 horizontal bars and 62 vertical bars, 56 horizontal bars and 56 vertical bars, respectively. Outer array 1, 2 are both composed of 62 vertical bars. Emitted photons are collected from one end by a multi-anode photomultiplier (MAPMT). Table 2.1 shows channels of $p\overline{p}$ annihilation at rest and their fractions [57]. Pions are produced at the mean energy of $\sim$ 2 GeV and the number of charged pions are three on average. When the charged pions resulted from annihilations lose energy inside the plastic scintillator, molecules of the scintillation material are excited and photons are emitted through de-excitation. The number of photons is propotional to the energy deposit. The photons are collected by the photomultiplier (PMT) which converts the photons into an electric current and amplify it so as to be easily measured. Plastic scintillators are in use because they are relatively inexpensive, easy to fabricate and they respond quickly on the order of ns.

Table 2.1: Annihilation channels for $p\overline{p}$ at rest. This table is adapted from [57].

channel	fraction [%]
π^+, π^-	0.375
π^+, π^-, π^0	6.9
π^+, π^-, more π^0	35.8
$\pi^+, \pi^+, \pi^-, \pi^-$	6.9
$\pi^+, \pi^+, \pi^-, \pi^-, \pi^0$	19.6
$\pi^+, \pi^+, \pi^-, \pi^-$, more π^0	20.8
$\pi^+, \pi^+, \pi^+, \pi^-, \pi^-, \pi^-$	2.1
$\pi^+, \pi^+, \pi^+, \pi^-, \pi^-, \pi^-, \pi^0$	1.85
$\pi^+, \pi^+, \pi^+, \pi^-, \pi^-, \pi^-$, more π^0	0.3

If annihilations are detected from both horizontal and vertical bars of inner arrays coincidently, the event is counted as an array detector count. The detection efficiency is estimated to be more than 90 %. Figure 2.17(b) shows a schematic view of the inner array. When both horizontal bar and vertical bar detect annihilations coincidently, a hit position can be determined as their intersection. A track can be estimated from the hit positions. From several tracks, an annihilation position can be estimated.

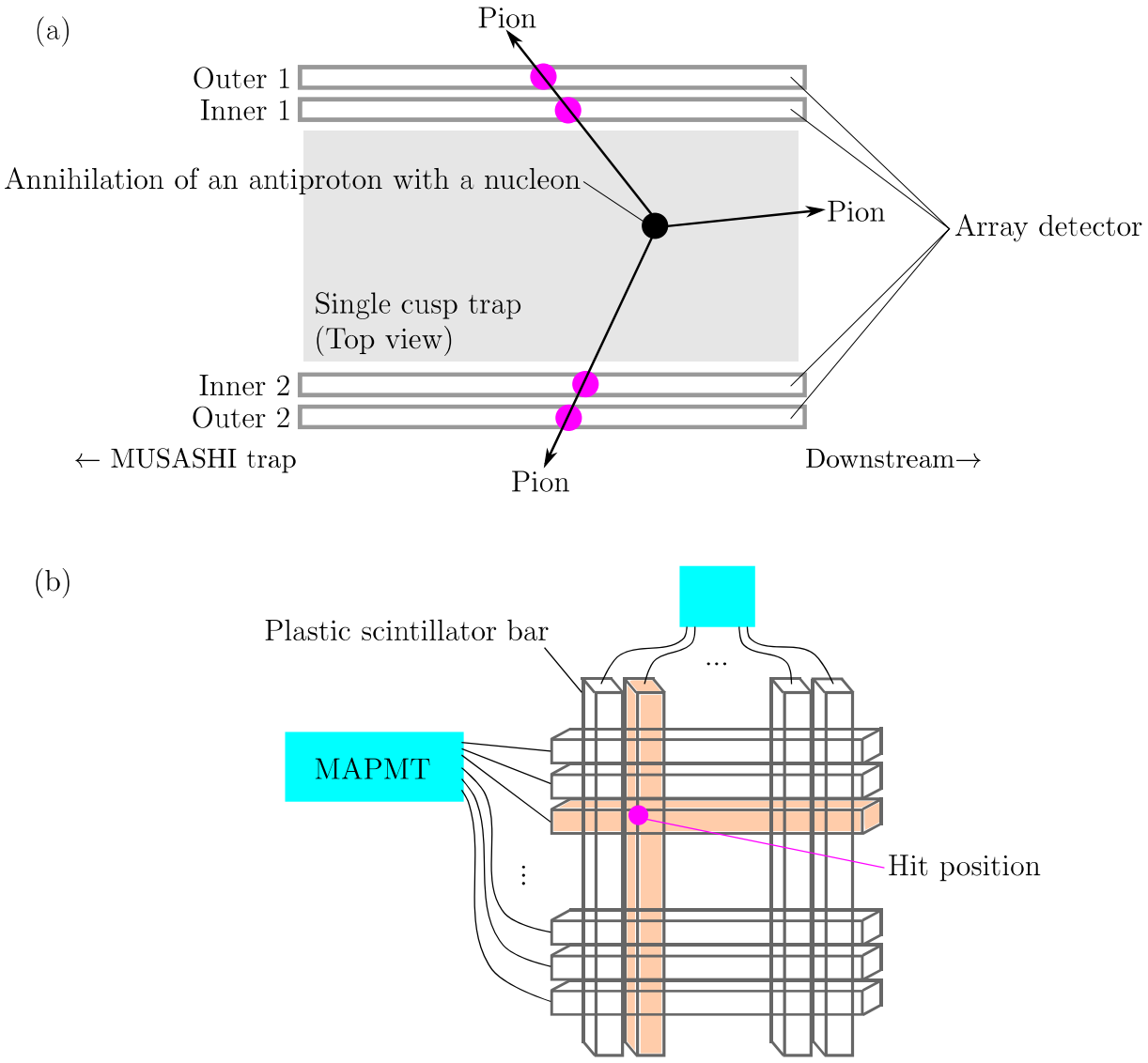

Figure 2.17: (a) A schematic view of the array detector. Four arrays of plastic scintillator bars are placed at both sides of the single cusp trap in order to monitor annihilations inside the single cusp trap, (b) A schematic view of the inner array. Three charged pions on average are produced when an antiproton annihilates with a proton. Photons emitted due to the energy deposit by charged pions are collected by Multi-anode photomultiplier (MAPMT) and detected. If annihilations are detected from both horizontal and vertical bars of inner arrays coincidently, the event is counted as an array detector count. A track can be estimated from the hit positions. From several tracks, an annihilation position can be estimated.

2.1.7 Antihydrogen detector using the BGO crystal and plastic scintillator plates

This section explains the antihydrogen detector which is placed at the most downstream of the experimental setup, 2.7 m from the production region.

The antihydrogen detector is composed of a disk of an inorganic scintillator crystal of Bismuth germanium oxide (BGO) with a 5-inch photomultiplier and surrounding 5 plastic scintillator plates with 2-inch photomultipliers. Figure 2.18(a) shows a positional relationship among the BGO crystal and plastic scintillator plates. The BGO is selected for its ultra-high vacuum compatibility and high density which resulted in large energy deposit. Figure 2.18(b) shows a schematic drawing of the cross section of the detector along the beam axis. Cylindrical electrodes are placed in front of the BGO crystal inside the vacuum.

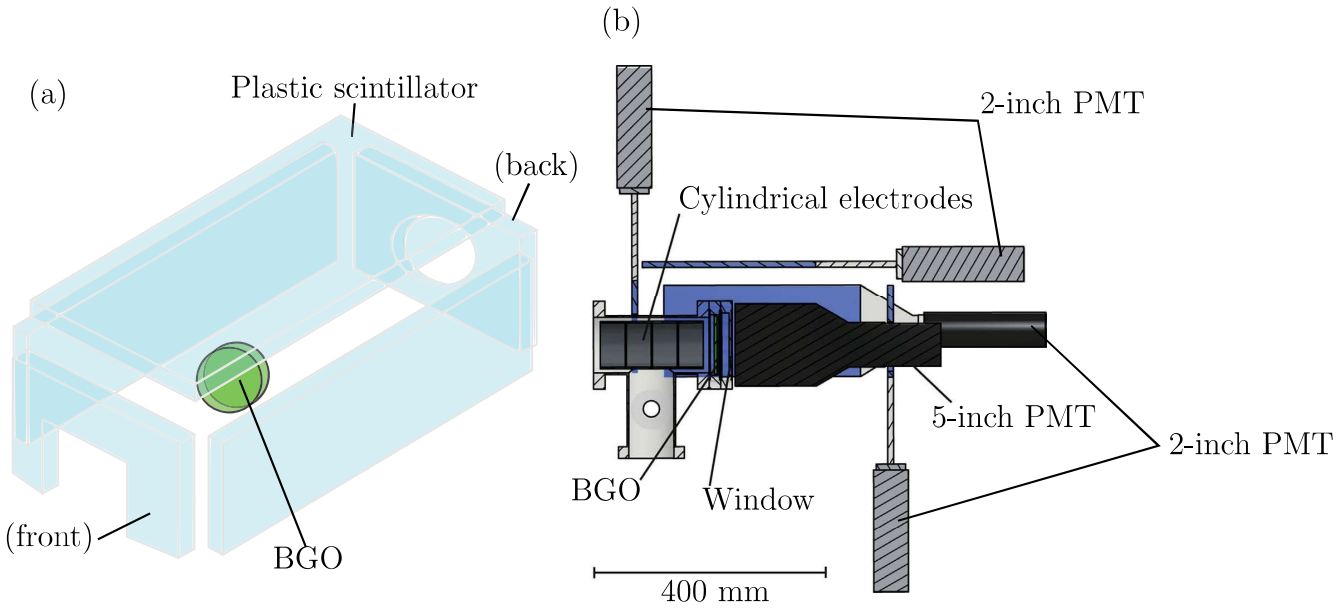

Figure 2.18: (a) A positional relationship among main components of the antihydrogen detector. A disk of an inorganic scintillator crystal of BGO is surrounded by 5 plastic scintillator plates. (b) A schematic drawing of the cross section of the detector along the beam axis. Cylindrical electrodes are placed in front of the BGO crystal inside the vacuum. Figures are adapted from [58].

Figure 2.19 illustrates the detection principle of the antihydrogen detector. Typical events are shown such as (a) antihydrogen atoms annihilated at the BGO crystal, (b) background pions resulted from annihilation of antihydrogen atoms before the detector, (c) background pions resulted from annihilation of antiprotons within the cusp trap, and (d) background cosmic rays. When the resulted pions from annihilation at the BGO crystal are emitted perpendicular to the beam axis, they run within the disk for longer distance compared with background pions coming almost parallel to the beam axis from upstream. It means the energy deposit on the BGO crystal is the largest for annihilations of antihydrogen atoms at the BGO crystal. In addition, the number of tracks for Fig. 2.19(a) is expected to be larger compared with (b)(c)(d). It is because background pions usually penetrate from upstream to downstream side as shown in Fig. 2.19(b)(c) and background cosmic muons penetrate from top to bottom as shown in Fig. 2.19(d). The number of tracks can be estimated by the number of counts at the surrounding plastic scintillator plates which is detected coincidently at the timing of the hit on the BGO crystal. Although annihilations of a bare antiproton at the BGO crystal cannot be distinguished with an antihydrogen atom, the antiproton is reflected and cannot reach the BGO crystal by preparing a potential barrier at the cylindrical electrodes just before the BGO crystal. The electrodes can also be used to roughly estimate atomic states of antihydrogen atoms as discussed later.

Therefore, both energy deposit on the BGO crystal and multiplicity of the coincidence counts by plastic scintillator plates are expected to be larger for antihydrogen atoms compared with backgrounds. Candidate events are defined when both the amount of energy deposit on the BGO and the multiplicity are larger than each threshold. The threshold of the energy and the multiplicity should be optimized for better signal to noise ratio. Although it has a relatively simple structure, noise rejection rate reaches up to 99.50 ± 0.09 % [58].

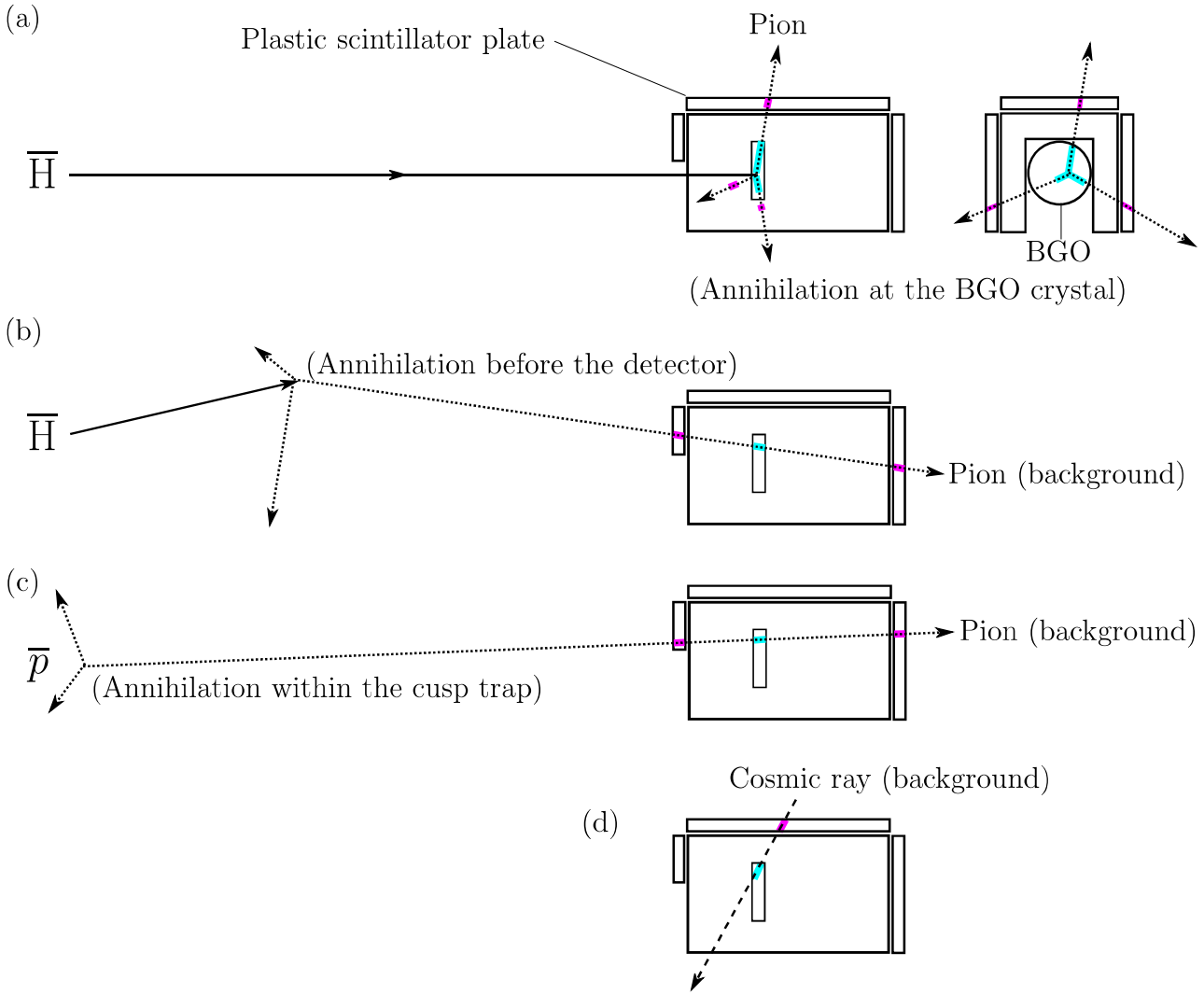

Figure 2.19: Schematic diagrams of the detection principle of the antihydrogen detector. Four typical events are shown such as (a) antihydrogen atoms annihilated at the detector, (b) background pions resulted from annihilation of antihydrogen atoms at the upstream side of the detector, (c) background pions resulted from annihilation of antiprotons within the cusp trap, and (d) background cosmic rays. Although annihilations of a bare antiproton at the BGO crystal cannot be distinguished with an antihydrogen atom, the antiprotons is reflected and cannot reach the BGO crystal by preparing a potential barrier at the cylindrical electrodes just before the BGO crystal. Both energy deposit on the BGO crystal and the number of the coincidence counts at the surrounding plastic scintillator plates which is detected coincidently at the timing of the hit on the BGO crystal are expected to be larger for antihydrogen atoms compared with backgrounds. Candidate events are defined when both the amount of energy deposit on the BGO and the multiplicity are larger than each threshold. The noise rejection rate reaches up to 99.50 ± 0.09 % [58].

2.2 Antihydrogen production in the single cusp trap with RF excitation

2.2.1 Recombination processes of antiprotons and positrons

For energy and momentum conservation, an antihydrogen atom cannot be produced from only one antiproton and one positron. Another component which is responsible for the binding energy is necessary. If it is a photon,

$$\overline{p} + e^+ \rightarrow \overline{\mathrm{H}} + h\nu \tag{2.9}$$

is a possible reaction and is called radiative recombination. The recombination rate per antiproton with a positron density of ρ_e [cm^{-3}] and temperature T is given by [59]

$$\Gamma = 3 \times 10^{-11}(4.2/T)^{-1/2}\rho_e\,[\mathrm{s}^{-1}]. \tag{2.10}$$

If another component is a positron,

$$\overline{p} + e^+ + e^+ \rightarrow \overline{\mathrm{H}} + e^+ \tag{2.11}$$

is possible and it is called three-body recombination. The recombination rate per antiproton with a positron density of ρ_e [cm^{-3}] is given by [60]

$$\Gamma = 6 \times 10^{-12}(4.2/T)^{-9/2}\rho_e^2\,[\mathrm{s}^{-1}] \tag{2.12}$$

Eq.(2.10) and Eq.(2.12) clearly show that the temperature should be small for higher recombination rate and three-body recombination becomes dominant as the temperature decreases.

2.2.2 Antihydrogen production

This section explains the procedure of mixing antiprotons with positrons to produce antihydrogen atoms in the single cusp trap, detection of antihydrogen atoms within the single cusp trap using the so-called field ionization technique, and the mixing with the RF excitation to prolong antihydrogen production.

As the procedure of mixing, positrons are prepared in the single cusp trap in advance. They are transported at 100 eV guided by magnetic field along the positron transport line from the positron accumulator into the single cusp trap, after accumulation for 30 s in the positron accumulator. This accumulation cycle is repeated typically for 25 times per one mixing cycle until 3×10^7 positrons are accumulated in the single cusp trap. The positrons are cooled down by cyclotron radiation in the single cusp trap and they can be considered as a plasma. This positron plasma is radially compressed by applying the rotating-wall electric field in a harmonic potential in the single cusp trap. After the radial compression, the potential called the nested well configuration is prepared and the positron plasma is confined at the center as shown in Fig. 2.20(a). Figure 2.20(b) shows the magnetic field on axis. The magnetic field strength is at maximum at the center of the nested well for a stable confinement of the positron plasma. Because of the self electric field of the plasma, the axial electric field vanishes inside the positron plasma in the equilibrium condition. Thereby the effective potential configuration of the nested well shows a plateau on axis within the positron plasma as shown in Fig. 2.20(a).

Then the antiprotons are transported at 150 eV from the MUSASHI trap through the antiproton transport line into the positron plasma which is confined in the single cusp trap for antihydrogen production. It is called direct injection scheme. When antiprotons are injected, the upstream side of the nested well is opened as shown with dashed line in Fig. 2.20(a) and the potential is quickly switched back as shown with solid line. Typically 3×10^5 antiprotons and 3×10^7 positrons are trapped in the single cusp trap per mixing. Antihydrogen production in the single cusp trap is first demonstrated in [61].

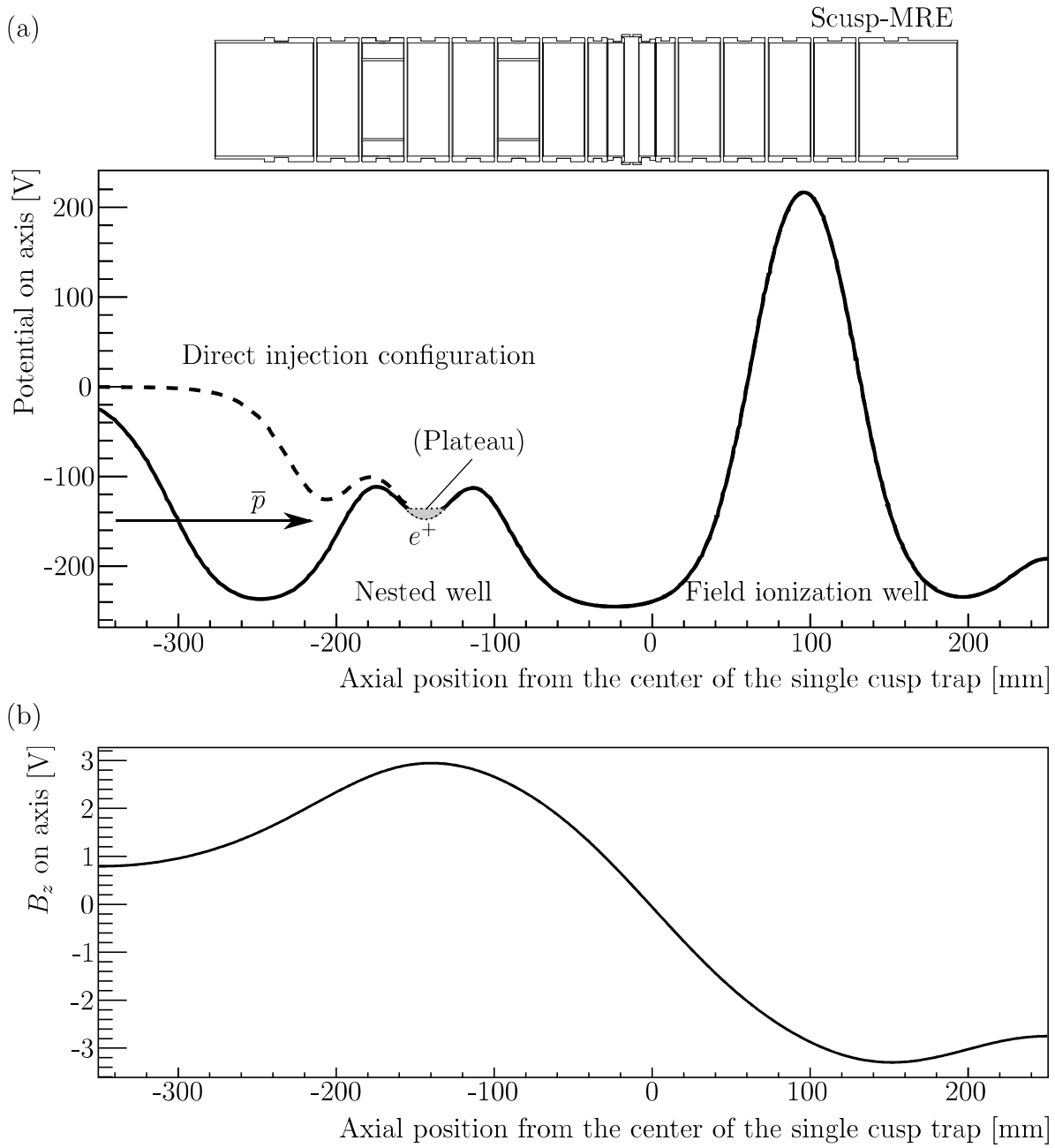

Figure 2.20: (a) Potential configurations during antihydrogen production. Solid line shows the nested well in the upstream side, and a field ionization well in the downstream side (discussed later). The positron plasma is confined at the center of the nested well after the radial compression. Because of the self electric field of the plasma, the effective potential configuration of the nested well shows a plateau on axis within the positron plasma. Antiprotons are injected into the positron plasma to produce antihydrogen atoms. When antiprotons are injected, the upstream side of the nested well is opened (dashed line) and quickly switched back (solid line). Typically 3×10^5 antiprotons and 3×10^7 positrons are trapped in the single cusp trap per mixing. Antihydrogen production in the single cusp trap is first demonstrated in [61]. (b) Magnetic field strength along the axis. It is at its maximum at the center of the nested well for a stable confinement of the positron plasma.

The number of antihydrogen atoms is estimated in the single cusp trap using a field ionization technique which had been utilized for an antihydrogen experiment by the ATRAP collaboration [26]. A deep potential well called the field ionization well is prepared at the downstream side as shown in Fig. 2.20(a). Once antihydrogen atoms are produced, they are neutral and cannot be confined by the electrostatic nested well and expected to move freely. If the antihydrogen atoms reach the field ionization well and are re-ionized by the steep electric field, the resulted antiprotons can be trapped inside the field ionization well. The trapped antiprotons should be antihydrogen-origin. It is because bare antiprotons are still confined in the nested well and cannot reach the field ionization well. Therefore the number of antihydrogen atoms can be estimated by counting the trapped antiprotons in the field ionization well.

The potential experienced by an positron in antihydrogen atom with an external electric field $(0, 0, F)$ is

$$V(\mathbf{r}) = -\frac{e}{4\pi\epsilon_0 r} - Fz \tag{2.13}$$

where ϵ_0 is permittivity of free space, e is unit charge, and z is a distance from the antiproton along the external electric field. A magnetic field and Stark effect is ignored for simplicity here. Figure 2.21 shows the potential when the external electric field is $F = 100$ V/cm. The binding energies defined by $-13.6/n^2$ eV are also shown where n is principal quantum number of the antihydrogen atom. Antihydrogen atoms with $n \leq 40$ are still attractive, while those with $n \geq 45$ are no longer bound states and ionized. The saddle point $z = z_s$ is given by solving

$$-\frac{e}{4\pi\epsilon_0 z_s^2} - F = 0. \tag{2.14}$$

If the potential energy at $z = z_s$ is equal to the binding energy of an antihydrogen atom as

$$-\frac{e}{4\pi\epsilon_0 z_s} - Fz_s = -\frac{13.6}{n^2}, \tag{2.15}$$

the required electric field in order to ionize the antihydrogen atom is given by

$$F = \frac{\pi\epsilon_0 Ry^2}{e^3 n^4} \sim \frac{3.2 \times 10^8}{n^4} V/\mathrm{cm}. \tag{2.16}$$

The field ionization scheme can be used to estimate atomic states of antihydrogen atoms [26].

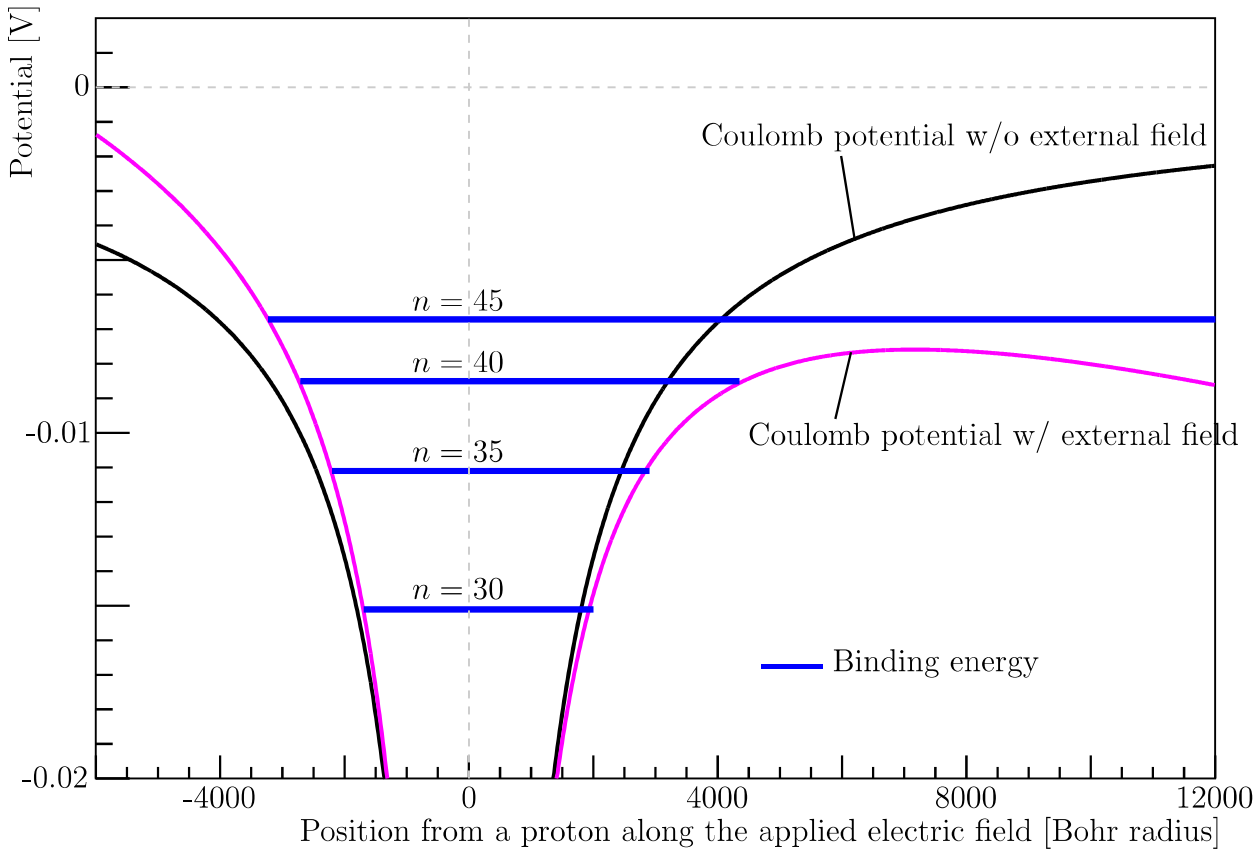

Figure 2.21: The potential distribution experienced by an positron in antihydrogen atom with and without the external electric field of $F = 100$ V/cm as a function of axial positions from the center of the antiproton trap along the external electric field. Horizontal solid lines show the binding energies defined by $-13.6/n^2$ eV for several principal quantum number n of the antihydrogen atom. Antihydrogen atoms with $n \leq 40$ are still attractive, while those with $n \geq 45$ are no longer bound states and ionized. It is called the field ionization technique and the number of antihydrogen atoms is estimated in the single cusp trap using this scheme.

Figure 2.22(a) shows the array detector count when the field ionization well is dumped for a short time at $t = t_{\rm dump}$. Antihydrogen atoms with $n \geq 45$ are ionized by the electric field on axis. The peak at $t_{\rm dump}$ corresponds to annihilations of antihydrogen-oriented antiprotons. The released antiprotons annihilate mainly at the position of zero magnetic field. It is because antiprotons are expected to diverge as the magnetic field becomes weak and annihilate on the inner surface of the scusp-MRE. The resulted pions are detected by the array detector. The number of field ionized events $N_{\rm FI}$ is defined as

$$N_{\rm FI} = N_s - N_b \times (2\,{\rm ms}/14\,{\rm ms}) \tag{2.17}$$

where the number of candidate events N_s is the sum of the filled region for 2 ms (from $t_{\rm dump}$ to $t_{\rm dump} + 2$ ms) and the number of background events N_b is the sum of the filled region for 14 ms in total, for 8 ms (from $t_{\rm dump} - 10$ ms to $t_{\rm dump} - 2$ ms) and for 6 ms (from $t_{\rm dump} + 4$ ms to $t_{\rm dump} + 10$ ms). The factor of (2 ms / 14 ms) normalizes the background events.

A time evolution of antihydrogen production can be monitored by periodically counting the field ionized events [61]. Figure 2.22(b) shows the applied voltage on D5 electrode as a function of time where the field ionization well is prepared. The field ionization well is kept for 5 s at $V_{\rm D5} = 350$ V and collapsed at $V_{\rm D5} = 0$ V. This cycle is repeated for 15 times typically. Squares in Fig. 2.22(c) shows the time evolution of antihydrogen production. The production rate reaches its maximum at 20 s after mixing start and decreases monotonically.

Inside the nested well, antiprotons gradually lose energy via collisions with antiprotons, positrons, electrons and then finally localizes in both potential maxima of the nested well. Electrons can exist because they are left behind when antiprotons annihilate with residual gas mainly composed of hydrogen. In addition, they can be injected from the MUSASHI trap together with antiprotons. If positrons and antiprotons are axially separated each other, antihydrogen synthesis stops, which explains the decrease of the antihydrogen production rate after ~ 30 s.

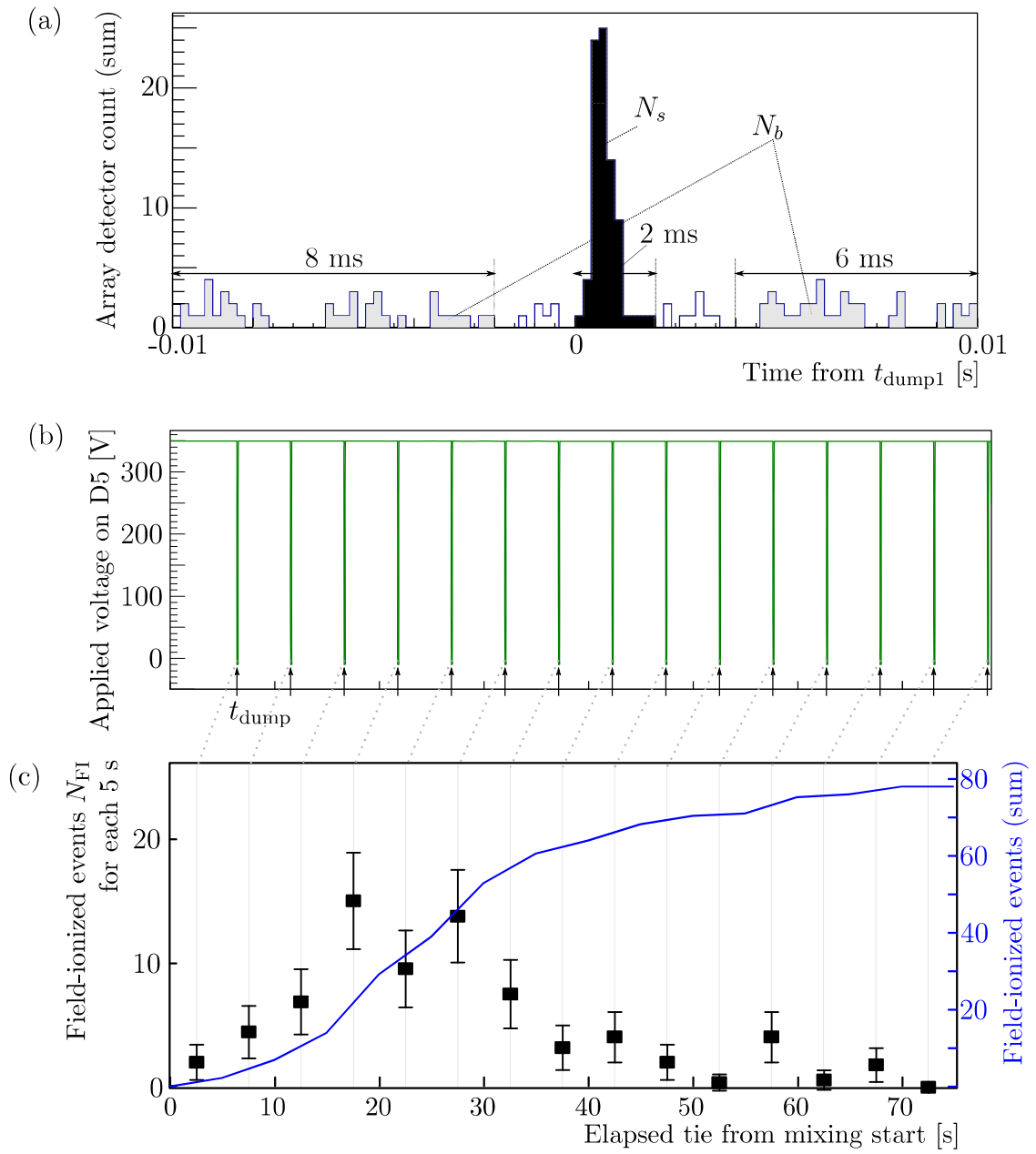

Figure 2.22: (a) The sum of array detector count for 15 cycles at $t_{\mathrm{dump}} - 10$ ms $\leq t \leq t_{\mathrm{dump}} + 10$ ms. The peak at $t = t_{\mathrm{dump}}$ corresponds to annihilations of antihydrogen-oriented antiprotons which are released at $t = t_{\mathrm{dump}}$ and annihilate at the inner wall of the scusp-MRE. The number of candidate events N_s and background events N_b are defined by the filled region. (b) The applied voltage on D5 electrode of the scusp-MRE, where the field ionization well is located, as a function of time. The field ionization well is kept for each 5 s at $V_{\mathrm{D5}} = 350$ V and collapsed at $V_{\mathrm{D5}} = 0$ V. This cycle is repeated for 15 times typically. (c) The field ionized events $N_{\mathrm{FI}} = N_s - N_b \times (2/14)$ for each 5 s as a function of time (square) and the sum of these events (blue solid line). The production rate reaches its maximum at 20 s after mixing start and decreases monotonically.

An RF field is applied in order to suppress the separation and prolong antihydrogen production. In particular, a sinusoidal electric field is applied on non-segmented U8 electrode of the scusp-MRE during mixing continuously. If localized antiprotons are accelerated and have enough energies, they can re-enter the positron plasma. The frequency and amplitude of the RF is optimized experimentally for higher antihydrogen yield at 440 kHz and 0.6 V_{p-p}. As a result, circles in Fig. 2.23 shows that the antihydrogen production continues longer with the RF excitation. The total number of field ionized events is increased by a factor of about 3.

Fig. 2.24 show the distributions of annihilation positions along the axis measured by the array detector. The filled histograms correspond to mixing without the RF excitation, while the histograms shown by thick lines correspond to mixing with the RF excitation. The histograms are summarized over time for 1 s $\leq t <$ 25 s, 25 s $\leq t <$ 50 s, 50 s $\leq t <$ 75 s, 75 s $\leq t <$ 100 s, 100 s $\leq t <$ 125 s, and 125 s $\leq t <$ 150 s (from top to bottom), respectively. The histograms are shifted vertically for visibility. The solid and dotted vertical lines correspond to the axial position of local maxima and minimum of the nested well as shown on top.

Both histograms show peaks at the center of the nested well where positrons exist in first several tens of seconds. However, the distribution of annihilation positions without the RF excitation becomes broad as time passes, which suggests that antiprotons lose energy and also exist in local maxima of the nested well where positrons do not exist. On the other hand, with the RF excitation, antiprotons still exist in the center of the nested well, where positrons exist, even after 100 s, which explains the continuous production shown by circles in Fig. 2.23.

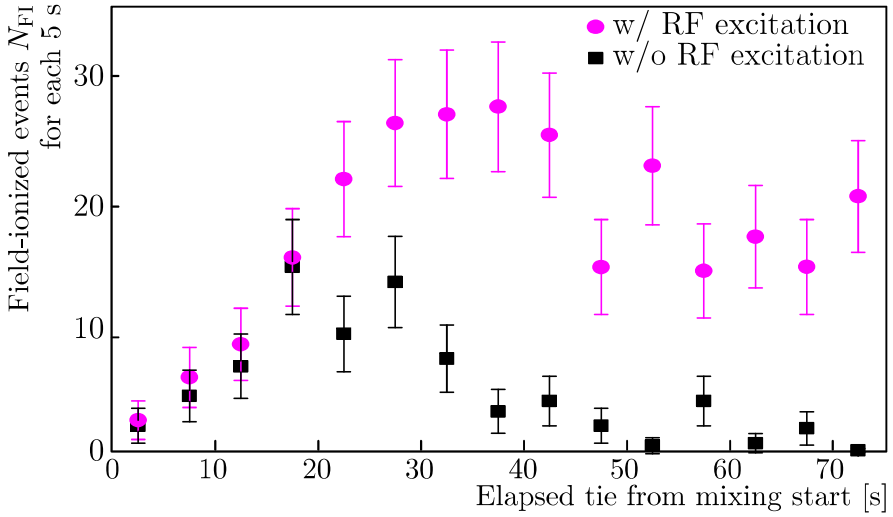

Figure 2.23: The field ionized events for each 5 s as a function of time with RF excitation (circle) and without RF excitation (square). The antihydrogen production continues longer with the RF excitation and the total number of field ionized events is increased by a factor of ~ 3.

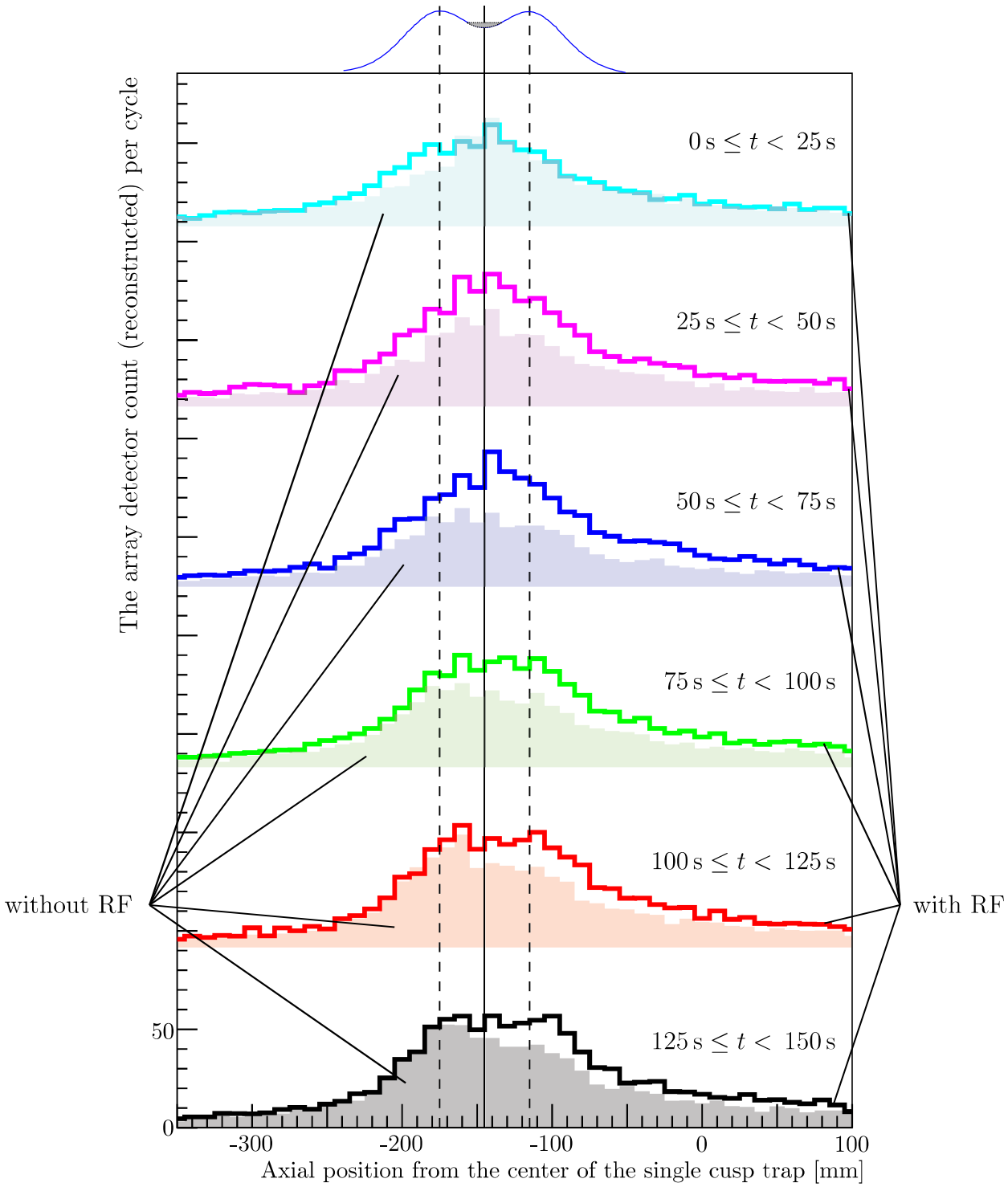

Figure 2.24: The distributions of annihilation positions along the axis measured by the array detector. The filled histograms show the data without the RF excitation. The histograms by thick lines show the data with the RF excitation. The histograms are summarized over time for every 25 s and shifted vertically for visibility. The solid and dotted vertical lines correspond to the axial position of local maxima and minimum of the nested well as shown on top. Both histograms show peaks at the center of the nested well where positrons exist in first several tens of seconds. However, the distribution of annihilation positions without the RF excitation becomes broad as time passes, which suggests that antiprotons lose energy and also exist in local maxima of the nested well where positrons do not exist. On the other hand, with the RF excitation, antiprotons still exist in the center of the nested well, where positrons exist, even after 100 s, which explains the continuous production shown by circles in Fig. 2.23.

2.3 Detection of antihydrogen beams

The produced antihydrogen atoms with the RF excitation are extracted to the antihydrogen detector located at the end of the experimental setup. This section explains about the detection of antihydrogen atoms by the antihydrogen detector.

In order to know the absolute value of the energy deposit in the BGO, a calibration should be done. It is done by comparison between simulations using a toolkit called GEANT4 [62] and experimental data of cosmic rays and pions [58]. The reason why cosmic rays and pions are used is that they can be distinguished from others by specific event selections as follows. The pions travelling through two plastic scintillators named front and back as shown in Fig. 2.18(a) can be distinguished by choosing the events accompanied by two coincidence counts at the two scintillator plates. The energy deposit on the BGO crystal by the pions shows a peak of minimum ionizing particle. The cosmic muons travelling top to bottom can be distinguished by choosing the events accompanied by one coincidence count at the top scintillator plate. The energy deposit on the BGO crystal by the cosmic muons shows a peak of minimum ionizing particle.

Figure 2.25(a) shows a comparison of the energy distribution on the BGO crystal between measurements mainly caused by cosmic rays and simulation results of cosmic rays using GEANT4 with CRY package [58]. Double coincidence events, which are defined as the events accompanied by two or more coincidence counts at surrounding plastic scintillator plates, for the measurements and simulations are in good agreement with each other.

Figure 2.25(b) shows a comparison of the energy distribution on the BGO crystal between typical mixing data with the RF excitation and simulation results assuming antiprotons are isotropically emitted from the center of the production region. Simulation results are shown separately for different types of events corresponding to those shown in Fig. 2.19(a)-(d). Thick solid line shows the total distribution. Double coincidence events for the measurements and for the simulations are also in good agreement with each other.

Therefore detection efficiency can be estimated by GEANT4 which depends on the threshold of the energy deposit to define an event as a candidate. The detection efficiency is estimated at ~ 45 % for the energy threshold at 40 MeV [58].

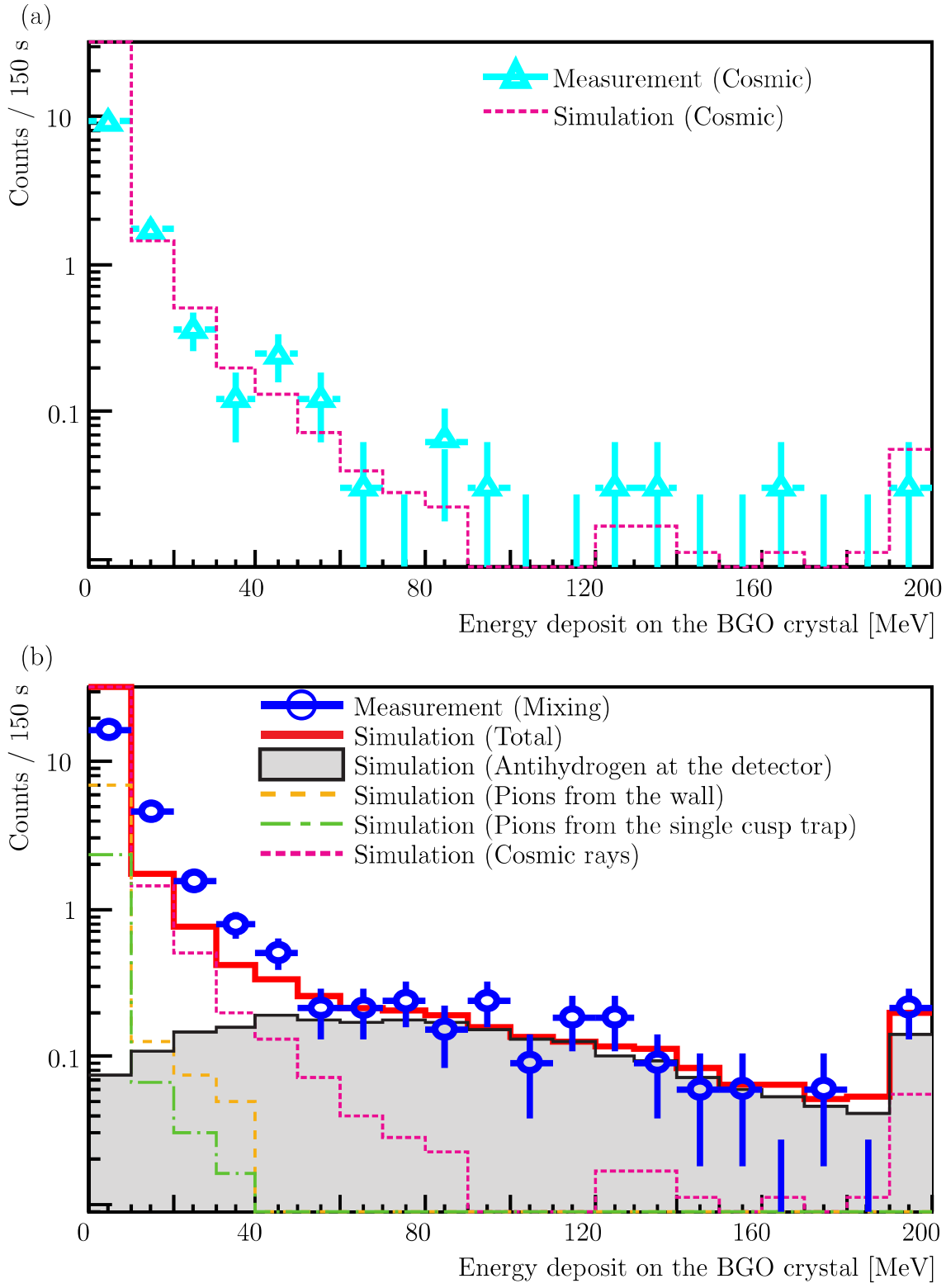

Figure 2.25: Comparison of the energy distribution in the BGO crystal between measurements and simulations using GEANT4. (a) is for cosmic rays and (b) is for mixing data of the double coincidence events which are defined as the events accompanied by two or more coincidence counts at surrounding plastic scintillator plates. Simulation results are shown separately for different types of events corresponding to those shown in Fig. 2.19(a)-(d). Measurements and simulations are in good agreement with each other. Figures are adapted from [58].

Figure 2.26 shows the measured distribution of energy deposit on the BGO crystal for double coincidence events. Events with higher energy deposition is observed during the mixing, while those with lower energy deposition is dominant for background events. Background events are estimated by measurements during cooling of antiprotons by electrons in the single cusp trap, in order to consider not only the cosmic rays but also pions resulted from antiproton annihilations within the single cusp trap.

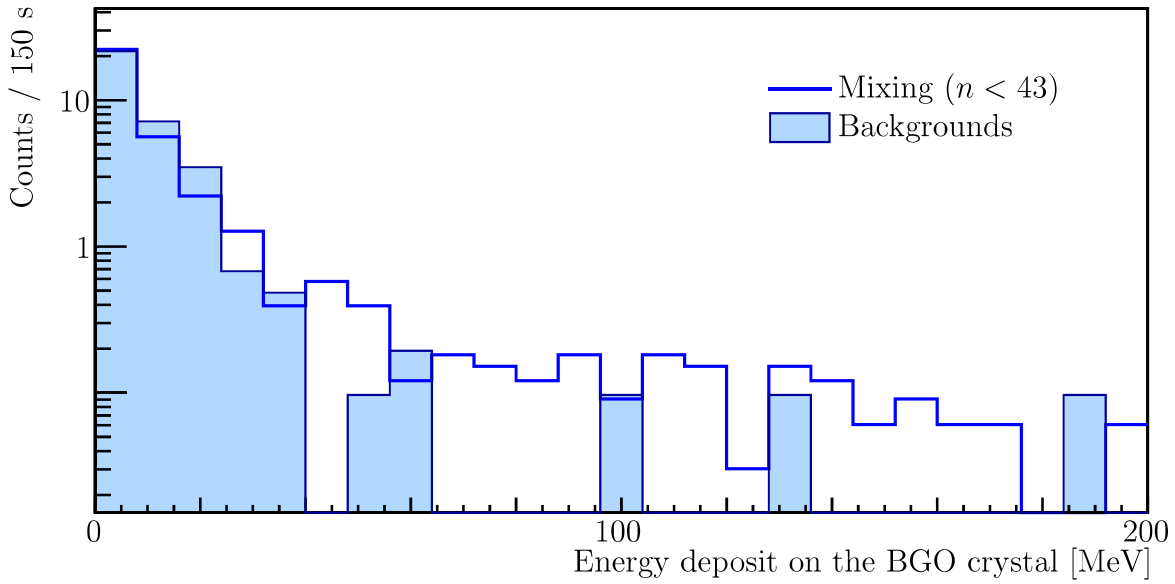

Figure 2.26: The measured distribution of energy deposit on the BGO crystal for the double coincidence events, quoted from [63]. Events with higher energy deposition is observed during the mixing, while those with lower energy deposition is dominant for background events. Background events are estimated by measurements during cooling of antiprotons by electrons in the single cusp trap, in order to consider not only the cosmic rays but also pions resulted from antiproton annihilations within the single cusp trap.

Table 2.2 shows a summary of detected events when the energy threshold is set at 40 MeV. Atomic states of antihydrogen atoms are roughly estimated by using the field ionization technique just before the detector. The cylindrical electrodes in front of the BGO crystal are used to prepare the electric field. Two conditions with averaged electric field at 94 V/cm and 452 V/cm are compared. The applied electric fields ionize antihydrogen atoms with principal quantum numbers higher than 43 and 29, respectively. The value is averaged over radial positions because the electric field produced by the cylindrical electrodes is not uniform.

Table 2.2: Summary of the double coincidence events above 40 MeV detected by the antihydrogen detector. Atomic states of antihydrogen atoms are roughly estimated by using the field ionization technique using the cylindrical electrodes in front of the BGO crystal.

Atomic states	Measurement time [s]	Double coincidence events above 40 MeV
$n \leq 43$	4950	99
$n \leq 29$	2100	29
Background	1550	6

Statistical significance of the difference between the number of candidates during mixing and background measurements can be evaluated as follows. Assuming Poisson distribution, the likelihood function as a function of expected signal count rate s and background rate b can be defined as

$$L(s, b \,|\, s_0, t_s, b_0, t_b) = \frac{\exp(-s_0 t_s)(s_0 t_s)^{(s+b)t_s}}{\Gamma((s+b)t_s)} \times \frac{\exp(-b_0 t_s)(b_0 t_s)^{bt_s}}{\Gamma(bt_s)} \tag{2.18}$$

where $s_0 t_s$ is the number of observed candidates, t_s is the measurement time for the observation of candidates, $b_0 t_b$ is the number of observed background, t_b is the measurement time for the observed background. Figure 2.27 shows a filled contour plot of the likelihood function for the case of $n \leq 43$. Solid lines show $L(s, b) = L_{68\%}$ and $L(s, b) = L_{99\%}$ which are defined as

$$\begin{aligned} \frac{\int\int L(s, b \,|\, L \geq L_{68\%})\, ds\, db}{\int\int L(s, b)\, ds\, db} &= 68\% \\ \frac{\int\int L(s, b \,|\, L \geq L_{99\%})\, ds\, db}{\int\int L(s, b)\, ds\, db} &= 99\% \end{aligned} \tag{2.19}$$

, respectively. According to this analysis, the number of the candidate events is estimated to be 81^{+19}_{-20} for $n \leq 43$ and 21^{+10}_{-9} for $n \leq 29$ (CL 68%) within the corresponding measurement time, respectively. The region where the signal count is zero (only background events) is outside of the filled region surrounded by the solid line $L(s, b) = L_{99\%}$, which means background-only hypothesis is rejected at 1 % significance level.

Therefore it is concluded that antihydrogen atoms are successfully detected at 2.7 m downstream from the production region at this level, which is a first step to the spectroscopy in the magnetic-field-free region [63].

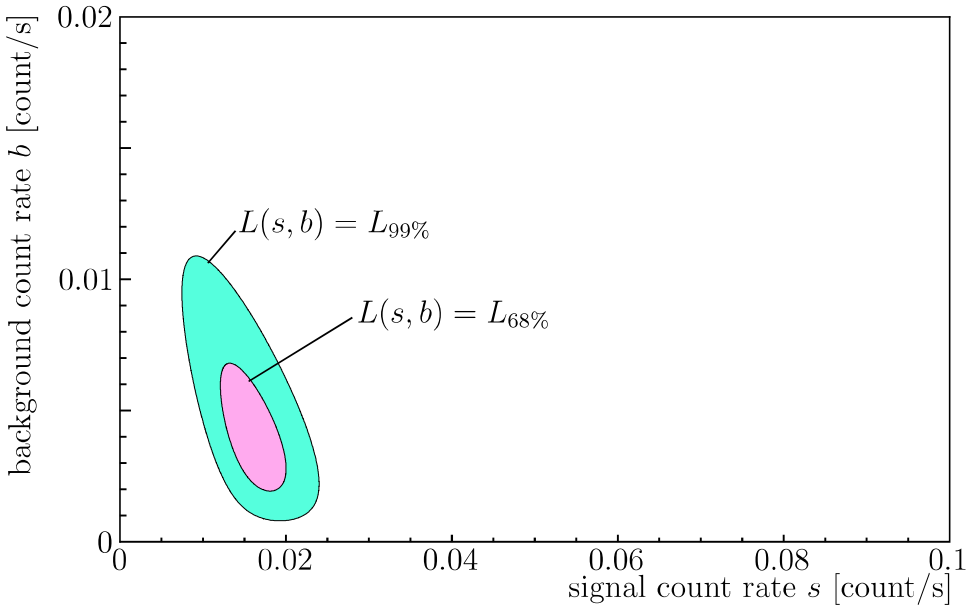

Figure 2.27: The contour plot of the likelihood function $L(s, b)$ as a function of signal count rate s and background rate b for antihydrogen atoms with $n \leq 43$ and backgrounds shown in Tab. 2.2. Solid lines show $L(s, b) = L_{68\%}$ and $L(s, b) = L_{99\%}$ (see Eq. (2.19)). The region where the signal count is zero (only background events) is outside of the filled region surrounded by the solid line $L(s, b) = L_{99\%}$, which means background-only hypothesis is rejected at 1 % significance level.

2.4 Unexpectedly broad energy spread of antiprotons at the injection into the single cusp trap

The time evolution of antihydrogen production gives an important insight for the proposed spectroscopy.

As shown in Fig. 2.22(c), the antihydrogen production rate decreases at the mixing start, when antiprotons are injected into positrons, and then gradually increases. It suggests that positron temperature increases by the injection of antiprotons and decreases gradually because of the cyclotron radiation, which implies that the relative energy of antiprotons with positrons is large and positrons are heated up.

The energy distribution of the injected antiprotons is actually measured as shown in Fig. 2.28(a). The number of trapped antiprotons are counted repeatedly with a different height of the potential barrier at the entrance of the single cusp trap. Since only those with higher energy than the barrier can be trapped, the trapped number as a function of the barrier height gives the energy distribution. Figure 2.28(b) shows the result. Solid line shows a fitting result by integral of a gaussian distribution shown by dashed line. The energy spread is unexpectedly broad compared with the temperature of antiprotons in the MUSASHI trap which is estimated about sub eV [51].

This is undesirable for the proposed spectroscopy. Figure 2.29 shows a schematic diagram of antiproton injection into a positron plasma which is confined in the center of the nested well. Magenta lines represent the energy distributions of antiprotons and filled regions correspond to fractions of available antiprotons for antihydrogen production. When the energy spread of the injected antiprotons is broad, the relative energy of antiprotons compared with the potential level of the positron plasma have to be large in order to trap antiprotons as many as possible to produce antihydrogen atoms as many as possible. As a result, positrons are heated up which leads to low production rate and production of antihydrogen atoms with large kinetic energy. In fact, this is the critical point for the spectroscopy at high precision. Chapter 3 describes about it in detail.

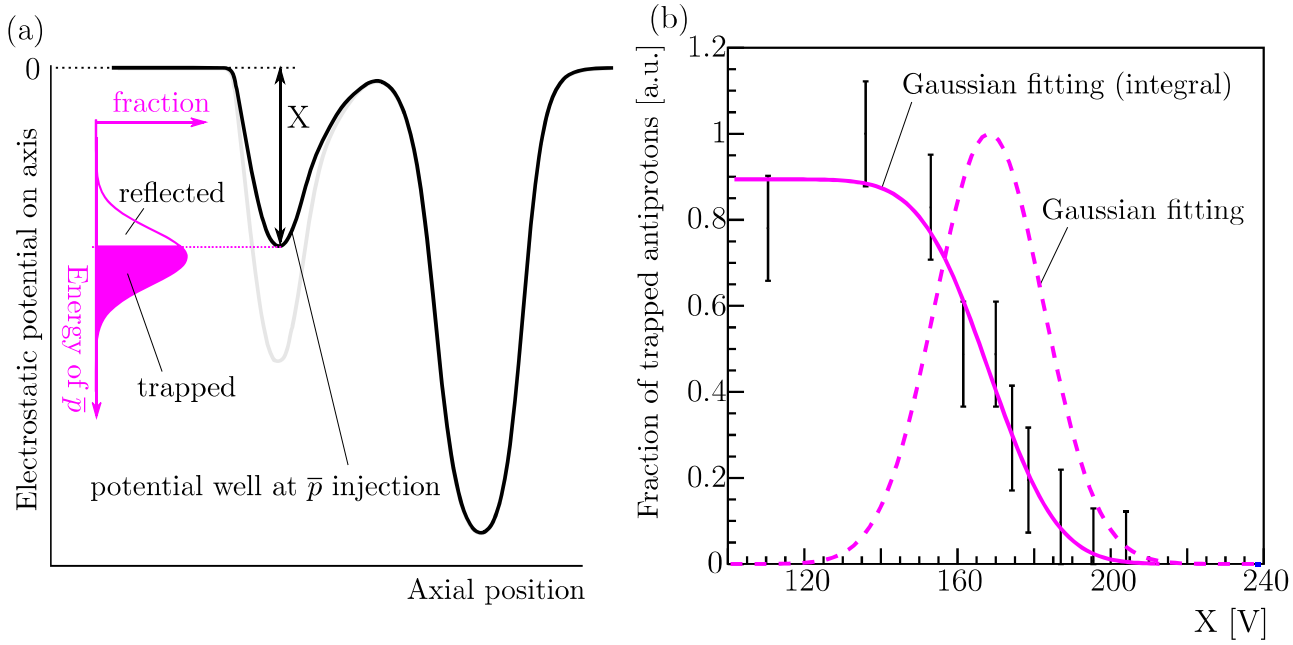

Figure 2.28: (a) The measurement principle of the energy distribution of antiprotons at the entrance of the single cusp trap. The number of trapped antiprotons are counted repeatedly with a different height of the potential barrier at the entrance. Since only those with higher energy than the barrier can be trapped, the trapped number as a function of the barrier height gives the energy distribution. (b) The number of trapped antiprotons as a function of the barrier height. Solid line shows a fitting result by integral of a gaussian distribution shown by dashed line. The energy spread is unexpectedly broad compared with the temperature of antiprotons in the MUSASHI trap which is estimated about sub eV [51].

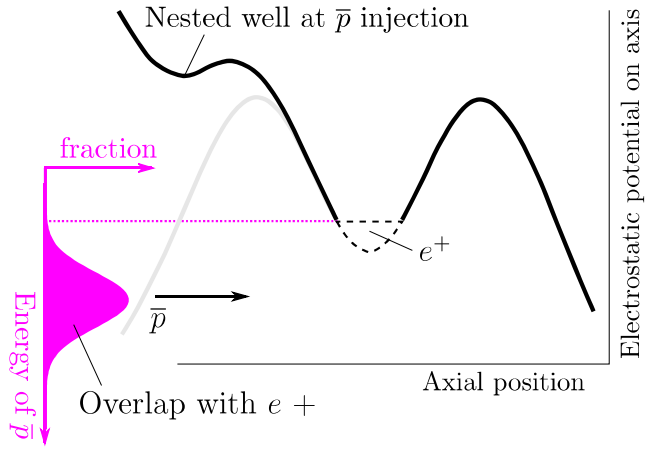

Figure 2.29: Schematic diagrams of antiproton injection into a positron plasma confined in the nested well. When the energy spread of the injected antiprotons is broad, the relative energy of antiprotons compared with the potential level of the positron plasma have to be large in order to trap antiprotons as many as possible to produce antihydrogen atoms as many as possible. As a result, positrons are heated up which leads to low production rate and production of antihydrogen atoms with large kinetic energy.

Chapter 3

Antihydrogen production towards the spectroscopy

In chapter 2, we described the successful production of antihydrogen atoms and its detection by a detector placed 2.7 m downstream of the production region. In order to conduct an antihydrogen spectroscopy with high precision, intense beams of highly spin-polarized antihydrogen in its ground state are necessary.

Slower antihydrogen atoms benefit us because it well make spin-polarization higher as it spends longer time in the cusp magnetic field gradient, so that the focusing (or defocusing) effect is stronger, and because it well make population of the ground state larger as it has longer time to cascade down from high Rydberg states to the ground state. In order to make slower, cooler antihydrogen atoms, the energy distribution of antiproton beam needs to be smaller as shown in Fig. 3.1. We modified the extraction scheme of antiprotons from the MUSASHI trap, and constructed a new antiproton transport line from the MUSASHI trap to the antihydrogen production region. Both are described in sections 3.1.1 and 3.1.2. In addition, as described in section 3.1.3, the antihydrogen production trap is replaced with a double cusp trap so that the beams of antihydrogen have higher spin-polarization. A new antiproton annihilation monitor with higher spatial resolution is installed. A newly designed antihydrogen detector is installed with a field ionizer in front so that we can measure the population of antihydrogen in the low-lying excited states. These are described in sections 3.1.4, 3.1.5, and 3.1.6.

Section 3.2 describes the improvement of the energy distribution of antiprotons, and section 3.3 describes the improved production rate of antihydrogen atoms as the result of the obtained smaller energy distribution. Section 3.4 describes the observation of antihydrogen

atoms in low-lying excited states, which is an important step for realization of spectroscopy experiment. Section 3.5 reports an inconsistency found in several antiproton/antihydrogen counters, and discusses non-isotropic distribution of antihydrogen atoms as a possible explanation. Section 3.6 reports an unexpected decrease of antihydrogen yield when we increase the density (and number) of positrons, and discusses the effect of self-field of positrons. Section 3.7 discusses the observed early stoppage of the antihydrogen production, and the spatial separation of antiprotons and positrons. Finally in section 3.8, a new mixing scheme between antiprotons and positrons based on the discussion in section 3.6 and 3.7, and a new de-excitation scheme for antihydrogen atoms are proposed.

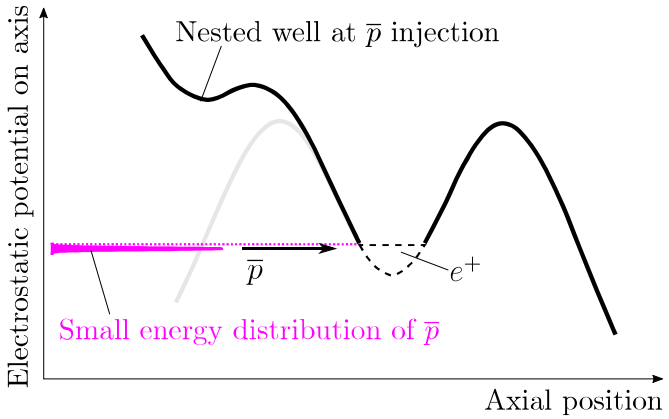

Figure 3.1: Schematic diagrams of antiproton injection with narrow energy spread into a positron plasma confined in the nested well.

3.1 Setup

Figure 3.2 shows the schematic view of the experimental setup including the positron accumulator, positron transport line, MUSASHI trap (antiproton trap), antiproton transport line, double cusp trap, field ionizer, and antihydrogen detector. The single cusp trap is replaced with the double cusp trap. In order to focus on antihydrogen production, the field ionizer and the antihydrogen detector are connected just after the double cusp trap for larger solid angle of the detector viewed from antihydrogen atoms produced in the double cusp trap. The positron accumulator and positron transport line are the same as described in chapter 2.

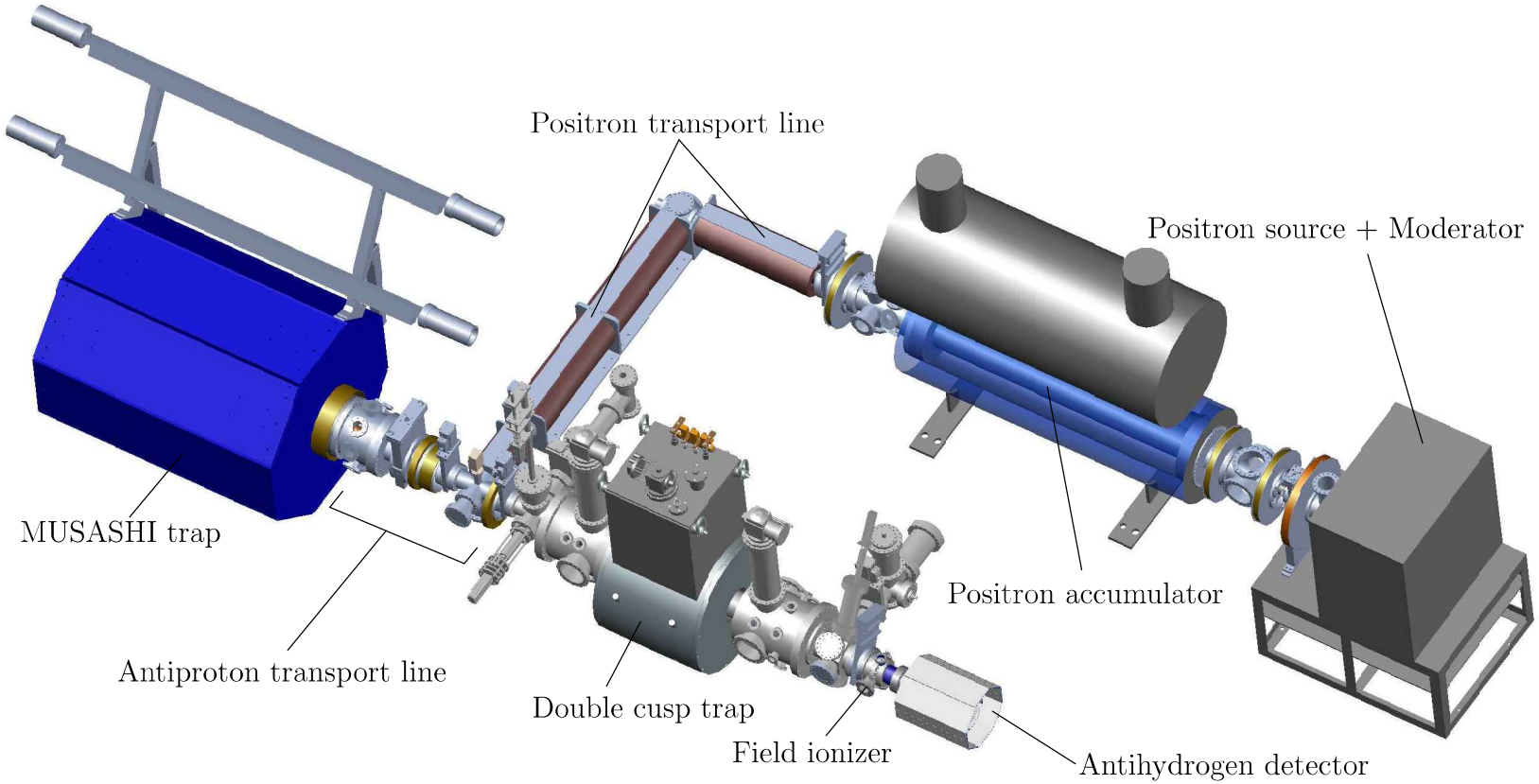

Figure 3.2: A schematic view of the experimental setup including the positron accumulator, positron transport line, MUSASHI trap (antiproton trap), antiproton transport line, double cusp trap, field ionizer, and antihydrogen detector. The single cusp trap is replaced with the double cusp trap. In order to focus on antihydrogen production, the field ionizer and the antihydrogen detector are connected just after the double cusp trap for larger solid angle of the detector viewed from antihydrogen atoms produced in the double cusp trap. The positron accumulator and positron transport line are the same as described in chapter 2.

3.1.1 MUSASHI trap with extraction of antiprotons for narrow initial energy spread

This section contains what is expected to be published within 5 years.

3.1.2 Antiproton transport line for adiabatic transport of antiprotons to keep the energy distribution

This section contains what is expected to be published within 5 years.

3.1.3 The double cusp trap for higher spin-polarization

The single cusp trap where antihydrogen atoms are produced in chapter 2 is replaced with the double cusp trap for higher spin-polarization.

The double cusp magnetic field has a better focusing power for antihydrogen atoms than the single cusp magnetic field. Figure 3.10 shows a cross sectional view of the double cusp trap and a magnetic field distribution of the double cusp magnet. There are three coils working as two pairs of anti-Helmholtz coils, a main coil at the center and two mirror coils. The coils are made of one superconducting wire and all connected, while its winding direction is opposite for the main coil. The magnet is surrounded by a magnetic shield made of massive iron of ~ 1000 kg. Figure 3.11 shows a circuit diagram of power supplies for the magnet. One power supply for all coils and additional power supplies for each of the two mirror coils are used. This double-cusp configuration with the massive iron magnetic shield also makes a leak magnetic field smaller, which is important for a precision spectroscopy.

The focusing performance of the magnet can be calculated using a total radial momentum Δp_r transferred to an antihydrogen atom given by [55]

$$\Delta p_r = \int_{-\infty}^{\infty} F_r \frac{dt}{dz} dz = \int_{-\infty}^{\infty} \frac{F_r}{v_z} dz. \tag{3.3}$$

where F_r is the radial force acting on the beam. Figure 3.12(a) shows the calculated intensity of antihydrogen beams at the expected position of the microwave cavity as a function of kinetic energy of antihydrogen atoms. The low-field seekers (LFS) are focused by the magnetic field gradient, while the high-field seekers (HFS) are defocused, which means more LFS and less HFS reach the expected position of the cavity as described before. The double cusp magnetic field has a better focusing power than the single cusp and the difference of the intensity between low-field seekers and high-field seekers is larger for the double cusp magnetic field. Fig. 3.12(b) shows the estimated spin-polarization $(f_{\mathrm{LFS}} - f_{\mathrm{HFS}})/(f_{\mathrm{LFS}} + f_{\mathrm{HFS}})$ from the calculation for the double cusp magnetic field. The spin-polarization for the single cusp magnetic field is shown together (same as Fig. 2.14(c)).

Even if antihydrogen atoms have the same kinetic energy, the higher spin-polarization can be achieved by using the double cusp magnetic field than the single cusp.

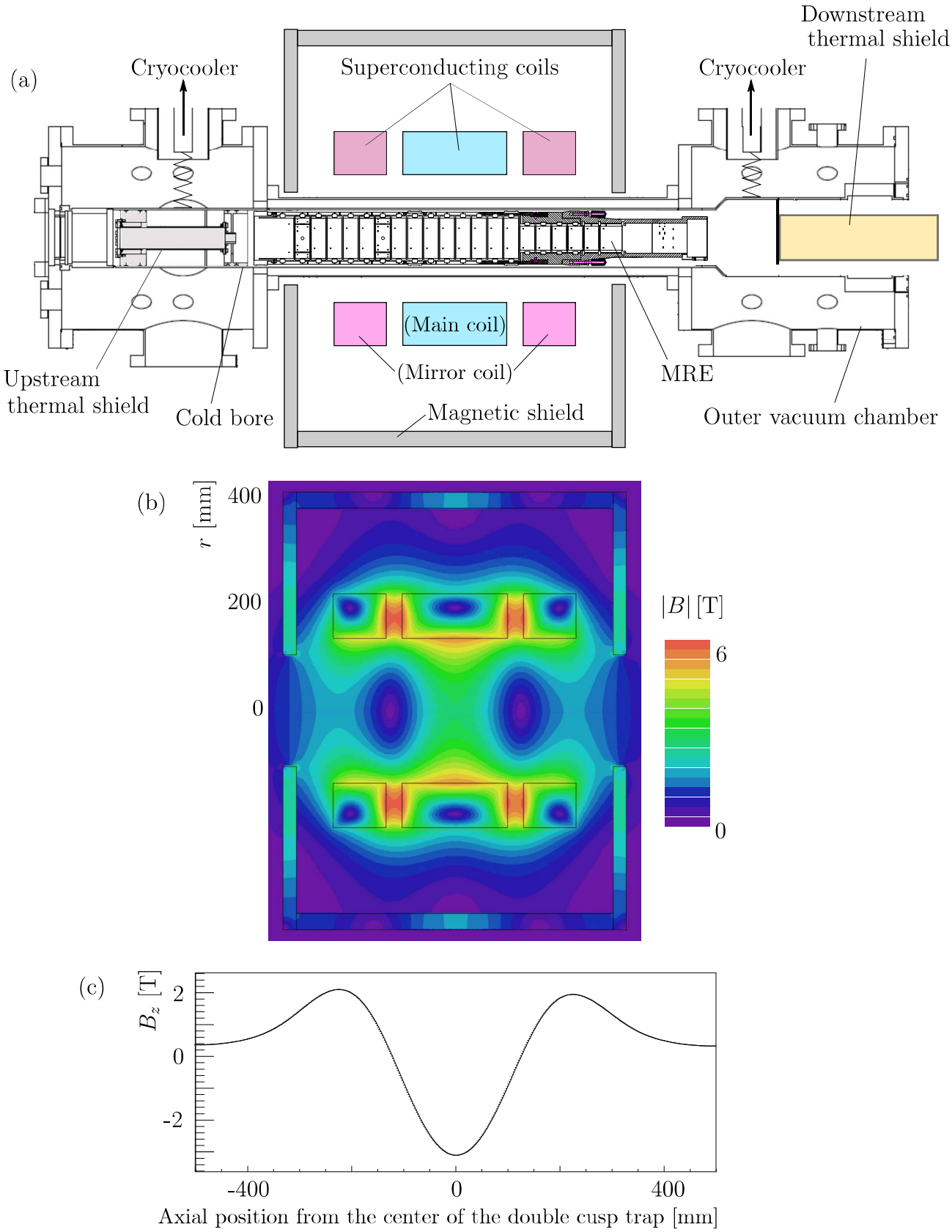

Figure 3.10: (a) A cross sectional view of the double cusp trap. There are three coils working as two pairs of anti-Helmholtz coils. The magnet is surrounded by a magnetic shield made of iron. Two-dimensional distribution of the magnetic field strength (b) and B_z distribution on axis (c) of the double cusp magnet.

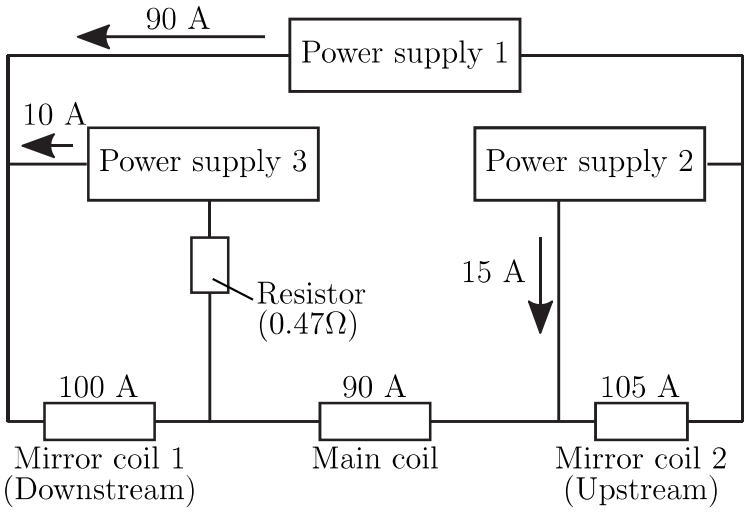

Figure 3.11: A circuit diagram of power supplies for the double cusp magnet.

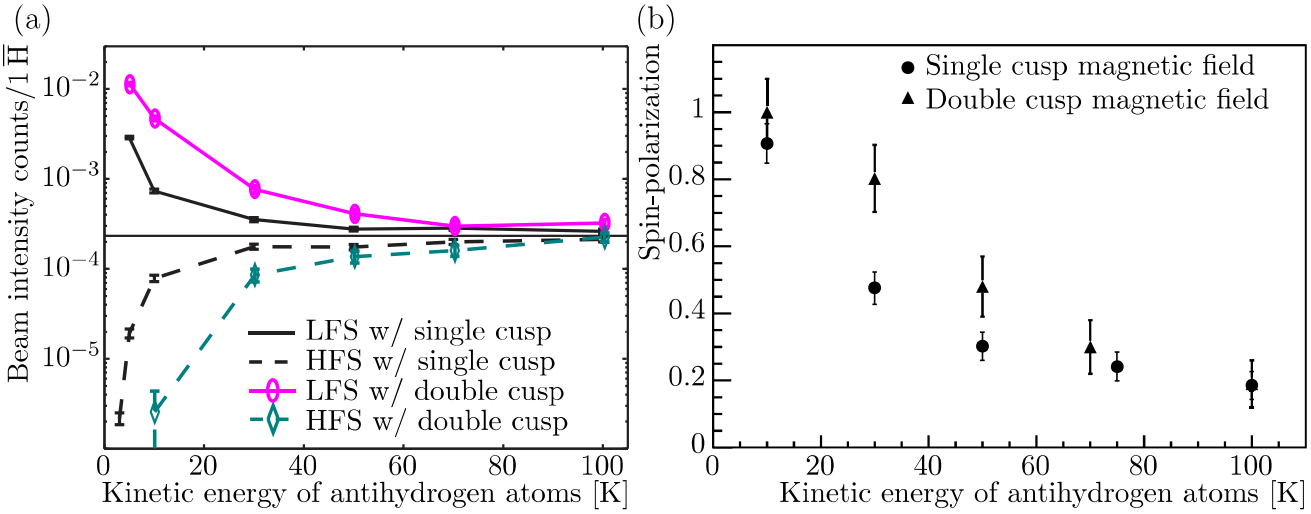

Figure 3.12: (a) The calculated intensity of antihydrogen beams at the expected position of the microwave cavity as a function of kinetic energy of antihydrogen atoms. The low-field seekers (LFS) are focused by the magnetic field gradient, while the high-field seekers (HFS) are defocused, which means more LFS and less HFS reach the expected position of the cavity. The double cusp magnetic field has a better focusing power than the single cusp and the difference of the intensity between LFS and HFS is larger for the double cusp magnetic field. (b) The estimated spin-polarization from the calculation for the double cusp magnetic field. The spin-polarization for the single cusp magnetic field is shown together (same as Fig. 2.14(c)). Even if antihydrogen atoms have the same kinetic energy, the higher spin-polarization can be achieved by using the double cusp magnetic field than the single cusp. Figures are adapted from [65].

Necessary modifications and developments about the double cusp trap are explained as follows.

In the double cusp magnetic field, the position of the local maximum of the magnetic field is shifted to the upstream side. Since positrons are stably confined at the local maximum, the center of the nested well should be located there. A longer MRE compared with the scusp-MRE, named dcusp-MRE, is designed in order to manipulate the potential under the double cusp magnetic field. Figure 3.13(a) shows a schematic drawing and Fig. 3.13(b) shows a picture of the dcusp-MRE and its support structure. There are 21 electrodes named U11 - U1, D1 - D10 from upstream to downstream. U10 and U5 are segmented azimuthally into four. Electrodes are made of aluminum with its surface coated by gold. A part of the support structure is made of copper.

There is a mechanism for better thermal contact between the dcusp-MRE and the cold bore wall to cool down the dcusp-MRE further. Parts with the shape of four separated-cylinder are prepared as a component of the support structure of the dcusp-MRE as shown in Fig. 3.13(a). The radius of the electrodes at downstream side becomes smaller to prepare the separated-cylinder part, keeping the same solid angle of the antihydrogen detector from the production region. Figure 3.14(a) shows a picture of the part. These parts with soft metal sheets made of indium (0.3 mmt) are inserted between the cold bore wall and the support structure of the dcusp-MRE using rods as shown in Fig. 3.14(b)(c). Foils made of copper and silver are also inserted to avoid adhesion. The indium sheets in between are pressed and deformed to fill gaps after inserted, which leads to a better thermal contact. Figure 3.14(d) shows a picture of the deformed sheet. Although the dcusp-MRE becomes longer than the scusp-MRE, the cold region of the bore is limited. The dcusp-MRE is placed so that it has a thermal contact only with the cold region.

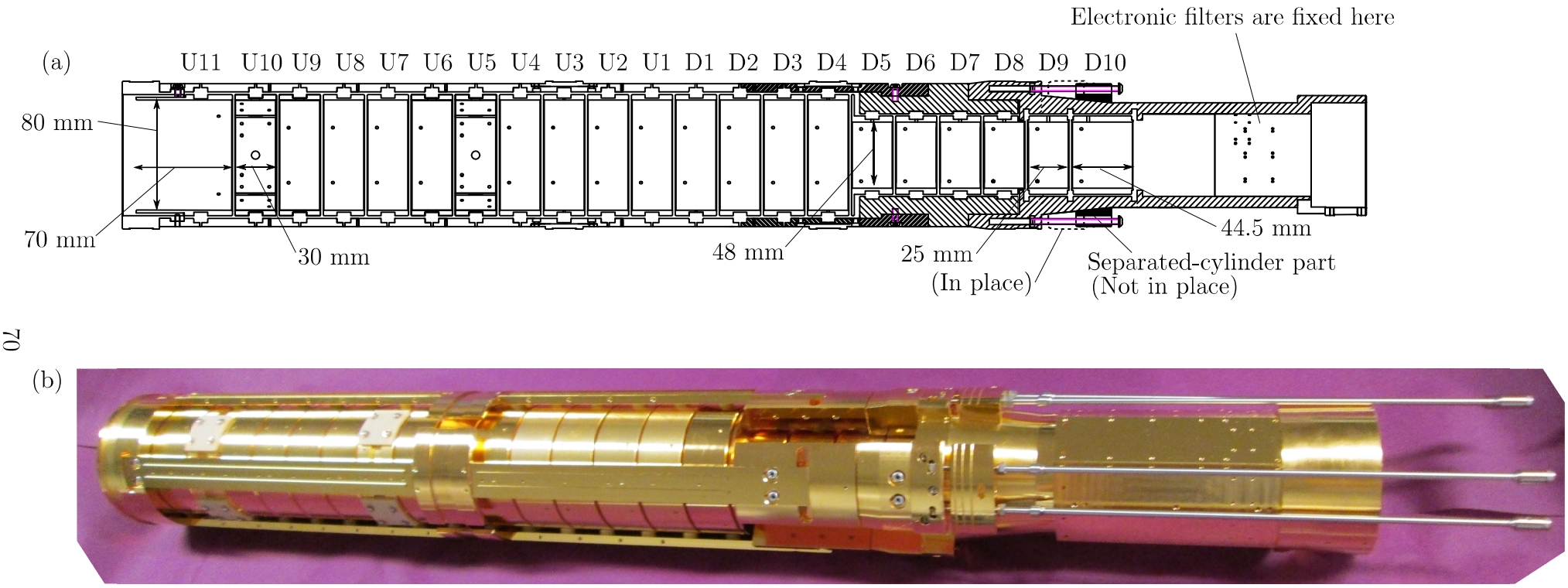

Figure 3.13: (a) A schematic drawing of the dcusp-MRE and its support structure. There are 21 electrodes named U11 - U1, D1 - D10, U10 and U5 are segmented azimuthally into four. Dotted line shows the position of the separated-cylinder part after inserted to be in place for better thermal contact. Several electronic filters are fixed on the surface of the support structure (described later). (b) A picture of the dcusp-MRE.

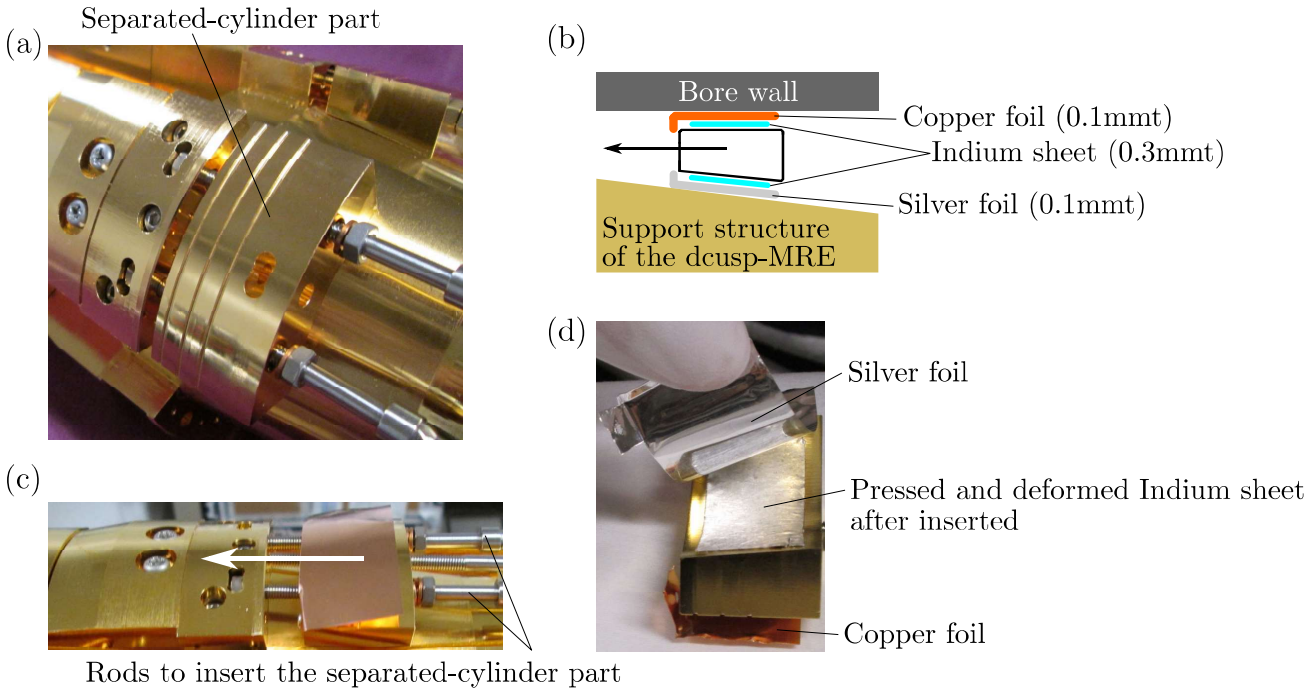

Figure 3.14: (a) A picture of the separated-cylinder part which is prepared as a component of the support structure of the dcusp-MRE for better thermal contact between the dcusp-MRE and the cold bore wall to cool down the dcusp-MRE further. (b) A schematic drawing of the part with soft metal sheets made of indium (0.3 mmt) between the cold bore wall and the support structure of the dcusp-MRE. Foils made of copper and silver are also inserted to avoid adhesion. (c) A picture of them with the rods to insert them between the wall and the support. (d) A picture of the pressed and deformed indium sheet after inserted.

Several electronic filters to reduce electric noise coming from the outside are connected to upstream electrodes of the dcusp-MRE because the noise can cause heating of trapped particles. The filters are fixed on the surface of the support structure of the dcusp-MRE and cooled down to cryogenic temperatures via thermal contact. Table 3.4 shows a summary of the cryogenic filters. Figure 3.15 shows four types of circuit diagrams of the cryogenic filters. Figure 3.15(a) shows a combination of Schottky barrier diodes and RC filters. When the noise with a small amplitude below a certain threshold and high frequency comes from outside, the current does not go through the diodes and the noise is cut off by the low-pass RC filters. On the other hand, when a pulsed voltage enough above the threshold and high frequency is applied, the current go through the diodes. Thus it is capable for both a noise rejection and a fast switching which is necessary for catching of particles.

Figure 3.15(b) shows the circuit diagram of the LC filters for applying rotating-wall electric field. The cut off frequency is 12 MHz. RC filters are not used because dissipation of energy through a resistor induce a diocotron motion of a plasma which should be avoided for a stable confinement.

Although it is not applied in this thesis, some setup for excitation and detection of plasma oscillation are installed as shown in Fig. 3.15(c) and (d), respectively. By applying RF for excitation of plasma oscillation through U9 or U6, the oscillation can be detected from U8. The voltage-control switch shown in Fig. 3.15(c) can be used for applying RF periodically. The detection of plasma oscillation using the same technique is reported in [66]. The RF terminal is connected to the GND for antihydrogen production described in this thesis.

All filters are arranged on PCB boards and placed as shown in Fig. 3.16 (view from downstream). The octagon at the center corresponds to the surface of the downstream side of the dcusp-MRE. For azimuthally segmented electrodes, four electrodes are named as A, B, C, and D clockwise (view from downstream).

Table 3.4: A list of electronic filters fixed on the support structure of the dcusp-MRE and connected electrodes.

Cryogenic filters	Connected electrodes	Diagram
Diode bridges+RC filters	U11, U4, U3, U2, U1	(a)
LC filters	U10, U5 (each of segmented electrodes)	(b)
Diode bridges+RC filters+switch	U9, U6	(c)
Diode bridges+RC filters+RF detection	U8	(d)
No filter	D1 - D10	-

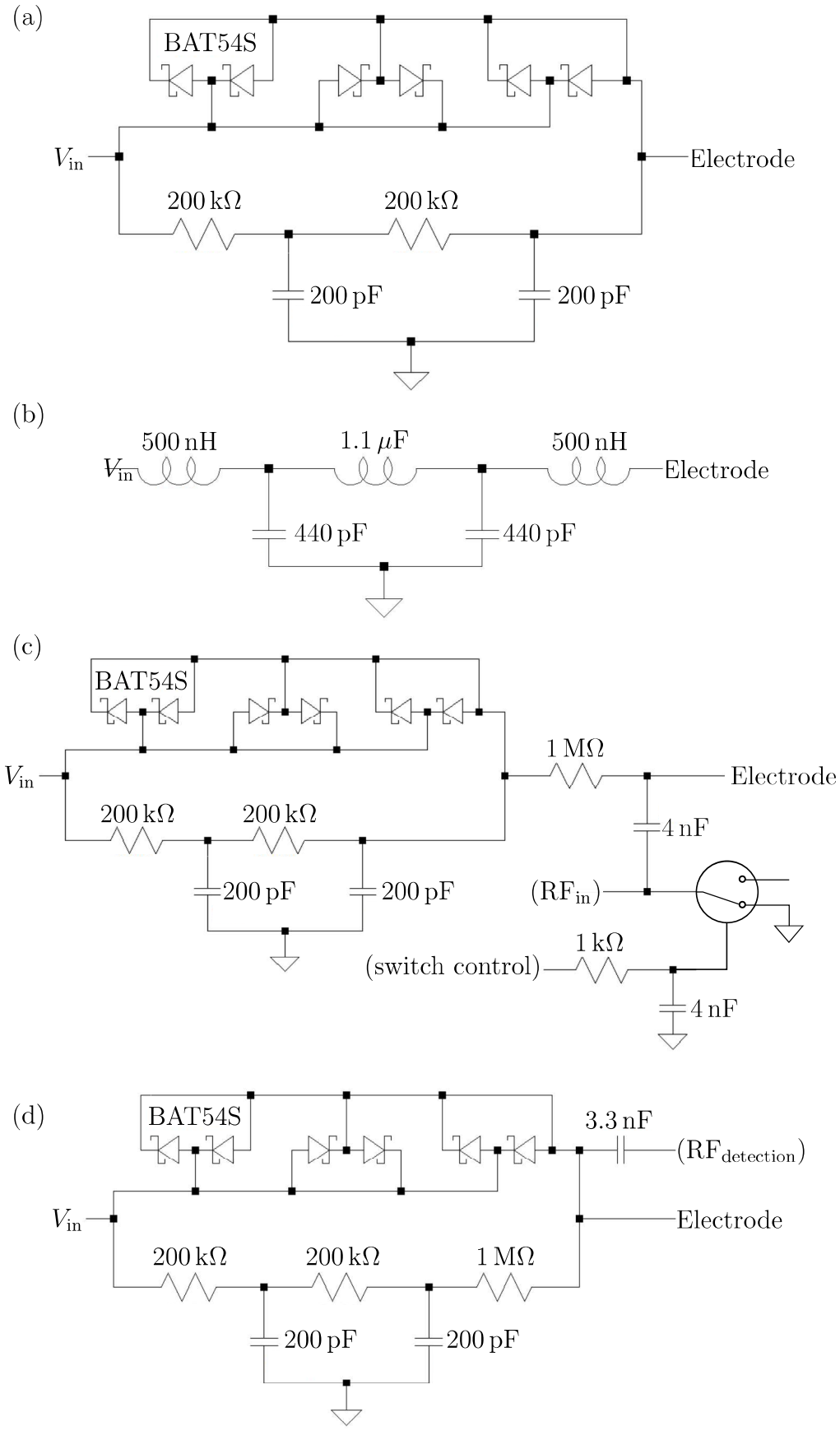

Figure 3.15: Circuit diagrams of the electronic filters to reduce electric noise coming from the outside, which are connected to upstream electrodes of the dcusp-MRE. (a) Diode bridges and RC filters. (b) LC filters. (c) Diode bridges, RC filters, and RF switch. (d) Diode bridges, RC filters, and RF detection terminal.

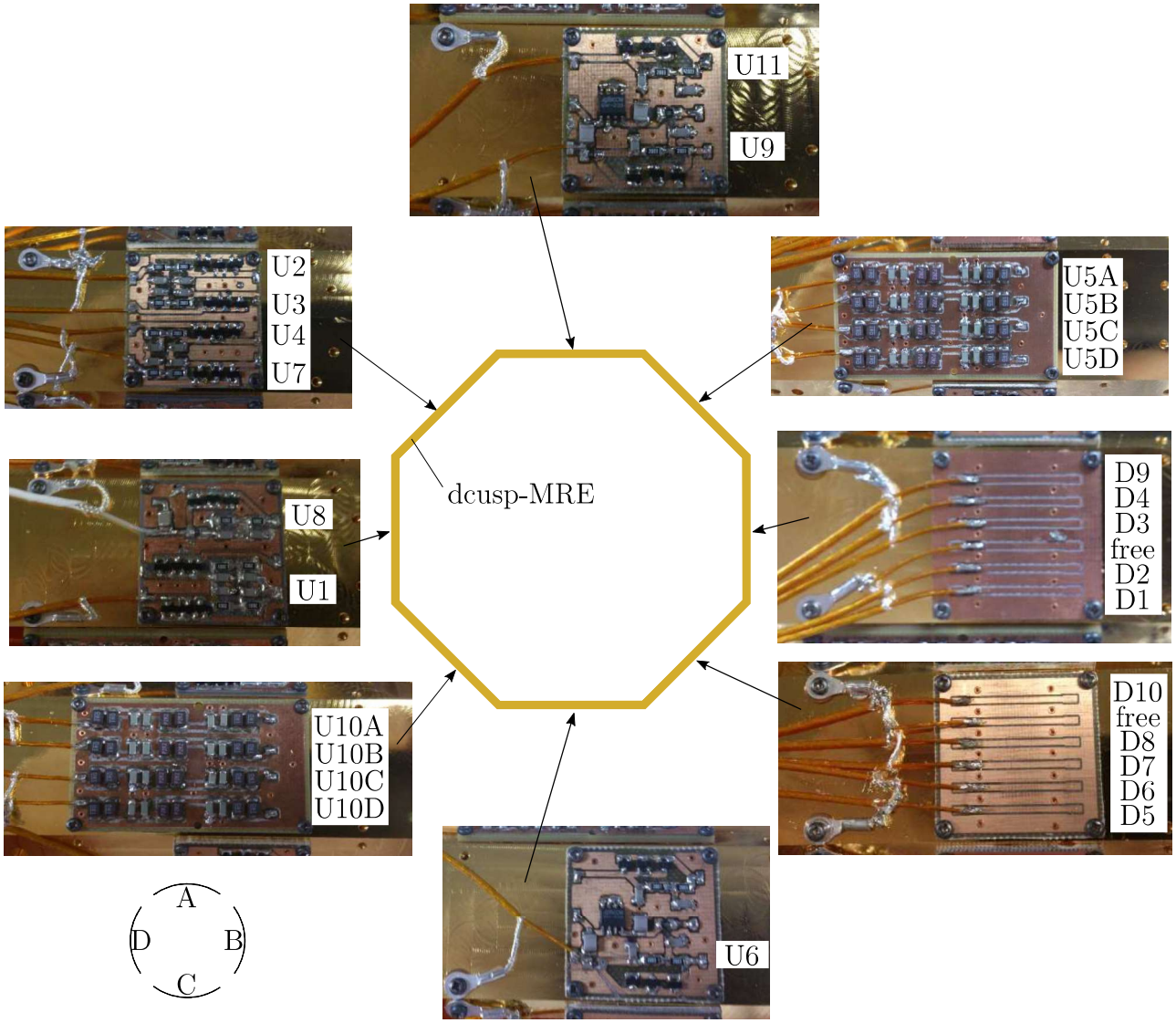

Figure 3.16: Pictures of the electronic filters. Their placements, looking from downstream side, are shown. The octagon at the center corresponds to the surface of the support structure of the dcusp-MRE.

Two thermal shields at upstream and downstream side of the dcusp-MRE are modified for more effective design. Regarding the upstream thermal shield, the center cylinder is black-Ni-plated. Thermal radiation from the room temperature upstream side is absorbed during reflection repeatedly on the inner wall of the cylinder to avoid the radiation from entering inside the dcusp-MRE. Figure 3.17 show pictures of the modified upstream thermal shield.

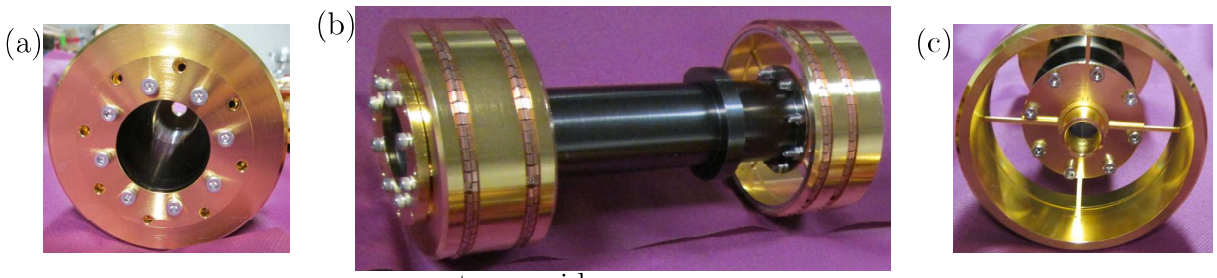

Figure 3.17: The view from upstream (a), side view (b), and view from downstream (c) of the modified upstream thermal shield.

Regarding the downstream thermal shield, the movable shield in chapter 2 is replaced with a cylinder-type shield shown in Fig. 3.18(a). The movable shield is not enough for extraction of antihydrogen atoms to downstream side, because the temperature of the dcusp-MRE increases up to 17 K when the shield is opened, due to the thermal radiation from the room temperature downstream side. The inner surface of the new shield is black-Ni-plated and carved many fine grooves in order to diffuse thermal radiation from the downstream. Figure 3.18(b) shows that it looks dark inside the cylinder due to the diffusion. The temperature of the dcusp-MRE is lowered down to 13.5 K with the cylinder-type shield. Since the temperature rise is suppressed, the evaporation of the frozen hydrogen on the surface of the dcusp-MRE and bore wall is reduced, which prevents deterioration of the vacuum. Background events for antihydrogen production due to annihilations of antiprotons with residual gas, is expected to be reduced.

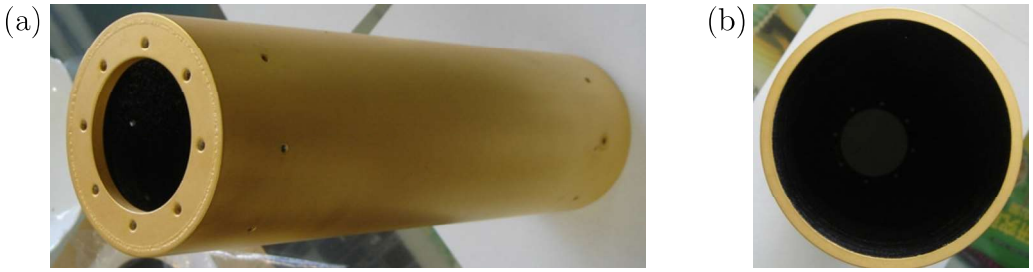

Figure 3.18: (a) A picture of the cylinder-type downstream thermal shield. (b) A view from downstream of the downstream thermal shield. It looks dark because the radiation is diffused.

3.1.4 ASACUSA MicroMEGAS Tracker to detect annihilations within the double cusp trap

An annihilation position sensitive detector called ASACUSA MicroMEGAS Tracker(AMT) is placed between the outer vacuum chamber of the cold bore and the double cusp magnet. The AMT is composed of two half-cylinder layers of the MicroMEGAS detector and one layer of eight plastic scintillator bars between them. Figure 3.19 shows main components and principle of operation of the MicroMEGAS. The MicroMEGAS is mainly composed of cathode made of kapton with copper on both sides, anode strips made of gold-coated copper, and a stainless steel woven micro-mesh. The mixed gas of Argon (90 %) and Isobutane (10 %) slowly flows within the MicroMEGAS. The electric field between the cathode and micro-mesh is 8 kV/cm and the electric field between the micro-mesh and anode-strips is 40 kV/cm as typical values. When a charged particle produces electrons through ionization of the mixed gas, the electrons are accelerated to the micro-mesh. They are amplified by producing secondary electrons in the thin region with higher electric field between the micro-mesh and anode strips. The amplified electrons are collected through anode strips (248 strips in axial direction and 448 strips in circumferential direction).

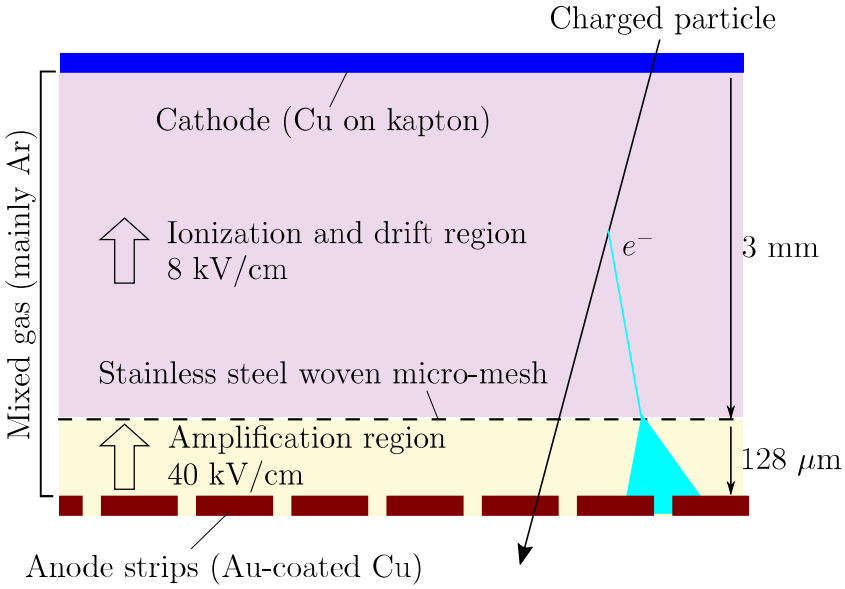

Figure 3.19: The main components of the MicroMEGAS including the cathode made of kapton with copper on both sides, anode strips made of gold-coated copper, and a stainless steel woven micro-mesh. A charged particle produces electrons through ionization of the mixed gas of Argon (90 %) and Isobutane (10 %), the electrons are accelerated to the micro-mesh by the electric field of 8 kV/cm and amplified by producing secondary electrons in the thin region with 40 kV/cm between the micro-mesh and anode strips. The amplified electrons are collected through anode strips.

Figure 3.20(a) shows a cross-sectional schematic view of the position of the AMT. The plastic scintillators are used to know the timing of the hit by the charged particle and produce a trigger to start data acquisition. Figure 3.20(b) shows a schematic view of the AMT including the support structure. Since the MicroMEGAS is normally used as a flat sheet, this curved structure is not straightforward and some development is required [67].

From a simulation including the magnetic field of the double cusp trap, a vertex resolution of about 7 mm is obtained [67], which is sufficient for discrimination between annihilations on the wall of the dcusp-MRE and inside the trap with residual gas which is mainly composed of hydrogen. The discrimination is important, because confined antiprotons annihilate with residual gas around the trap axis, while antihydrogen atoms and extracted antiprotons to the zero-magnetic-field position (mainly for counting the number) annihilate at the wall of the dcusp-MRE. Figure 3.20(c) and (d) show reconstructed 2-dimensional annihilation positions perpendicular to the beam axis, for the extracted antiprotons to the zero-magnetic-field position and for the confined antiprotons, respectively. Dashed line corresponds to the inner surface of upstream electrodes of the dcusp-MRE with their radius of 4 cm. Since the multiple scattering with the material between the dcusp-MRE and the detector affect the resolution, the AMT is less affected compared with the array detector which is placed outside of the magnet. The resolution is much better especially for the radial positions than the array detector. Further details are described in [67] [68].

When antiprotons annihilate inside the double cusp trap, released pions are detected by plastic scintillator plates surrounding the bore which is originally prepared for triggering of the data acquisition of the AMT. When two or more out of eight plates detect annihilations coincidently, the event is defined as a double coincidence count. The detection efficiency of an antiproton annihilation is more than 90 % for the double coincidence counts when it annihilate on the wall of the dcusp-MRE at the position of zero magnetic field. This double coincidence counts are called AMT scintillator counts hereafter.

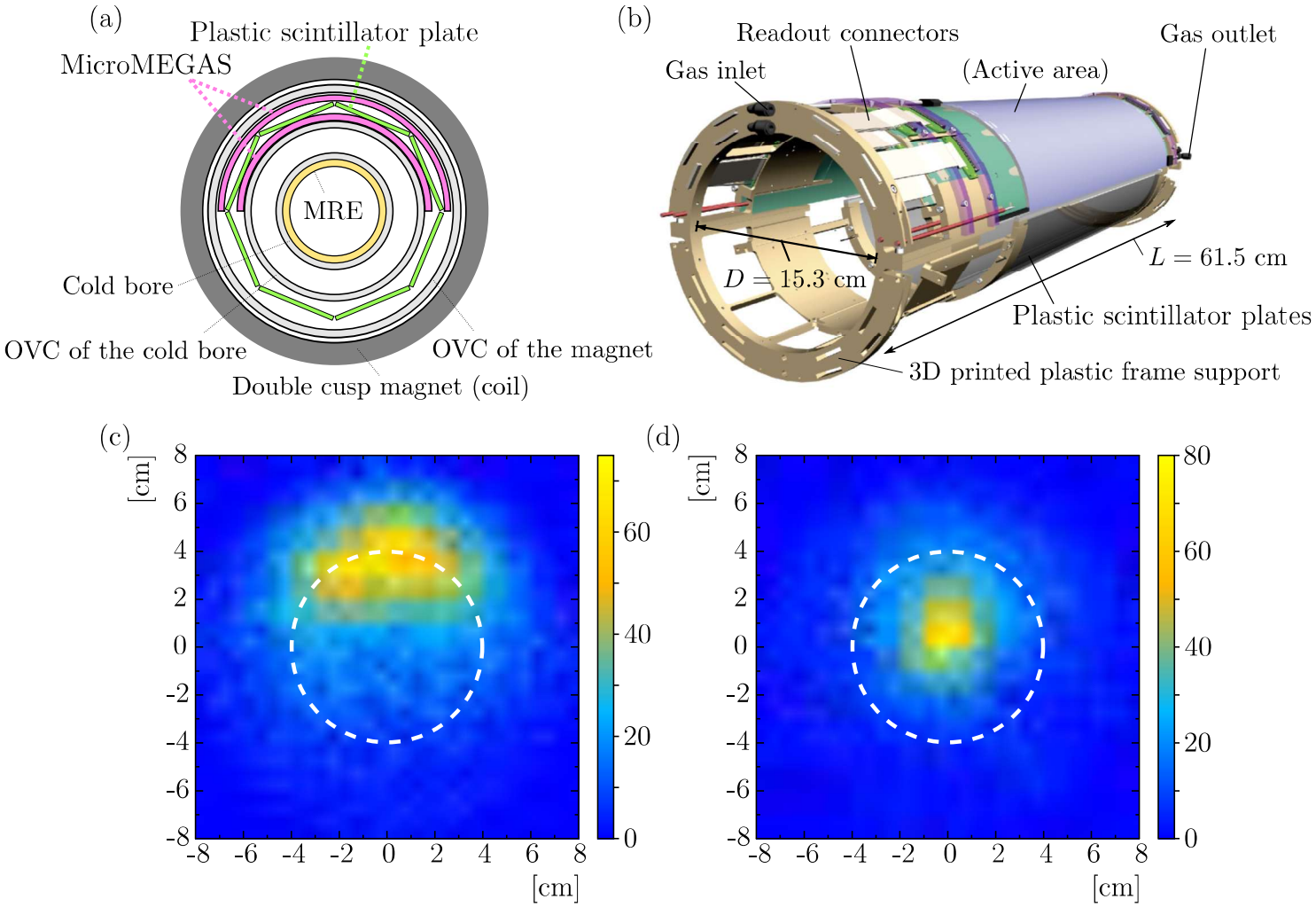

Figure 3.20: (a) The schematic diagram of the position of the AMT between the outer vacuum chamber of the cold bore and the magnet. (b) The schematic view of the AMT including the support structure adapted from [67]. (c)(d) Reconstructed 2-dimensional annihilation positions perpendicular to the beam axis, for the extracted antiprotons to the zero-magnetic-field position(c) and for the confined antiprotons(d), respectively. Dashed line corresponds to the inner surface of upstream electrodes of the dcusp-MRE with their radius of 4 cm. Figures are adapted from [69].

3.1.5 Field ionizer to investigate atomic states just before the antihydrogen detector

The field ionizer is installed at outside of the double cusp trap to investigate atomic states of antihydrogen atoms using the field ionization technique. Since a high electric field is required to monitor low-lying excited states as shown in Eq.(2.16), the field ionizer is designed to be capable for high electric field.

Figure 3.21(a) shows a schematic view of the field ionizer, mainly composed of two BeCu meshes with transparency of 95 % at a distance of 10.5 ± 0.5 mm. It is placed on the beam axis where the vacuum is $\sim 10^{-9}$ mbar. Each metal mesh is fixed at a metal ring and the ring is connected to a feedthrough to apply a voltage by a power supply from outside vacuum. The meshes produce an uniform electric field. We can monitor the principal quantum number independent on the radial positions, while it is not the case for the cylindrical electrodes used in chapter 2. By applying a positive high voltage $+V$ on a mesh at upstream side and a negative high voltage $-V$ on the other mesh at downstream side, an uniform high electrostatic field is produced, which avoids bare antiprotons from travelling down to the antihydrogen detector. Figure 3.21(b) a show picture of the actual setup. The ring is distant from the surrounding duct surface by 2 cm. Figure 3.21(c) shows a zoomed view of the coupling of the feedthrough and the ring.

Figure 3.21(d) shows a required voltage for the field ionizer to ionize an antihydrogen atom as a function of the principal quantum number. Two lines correspond to different distances between meshes. When ± 5 kV is applied, antihydrogen atoms of with $n \geq 14$ are ionized.

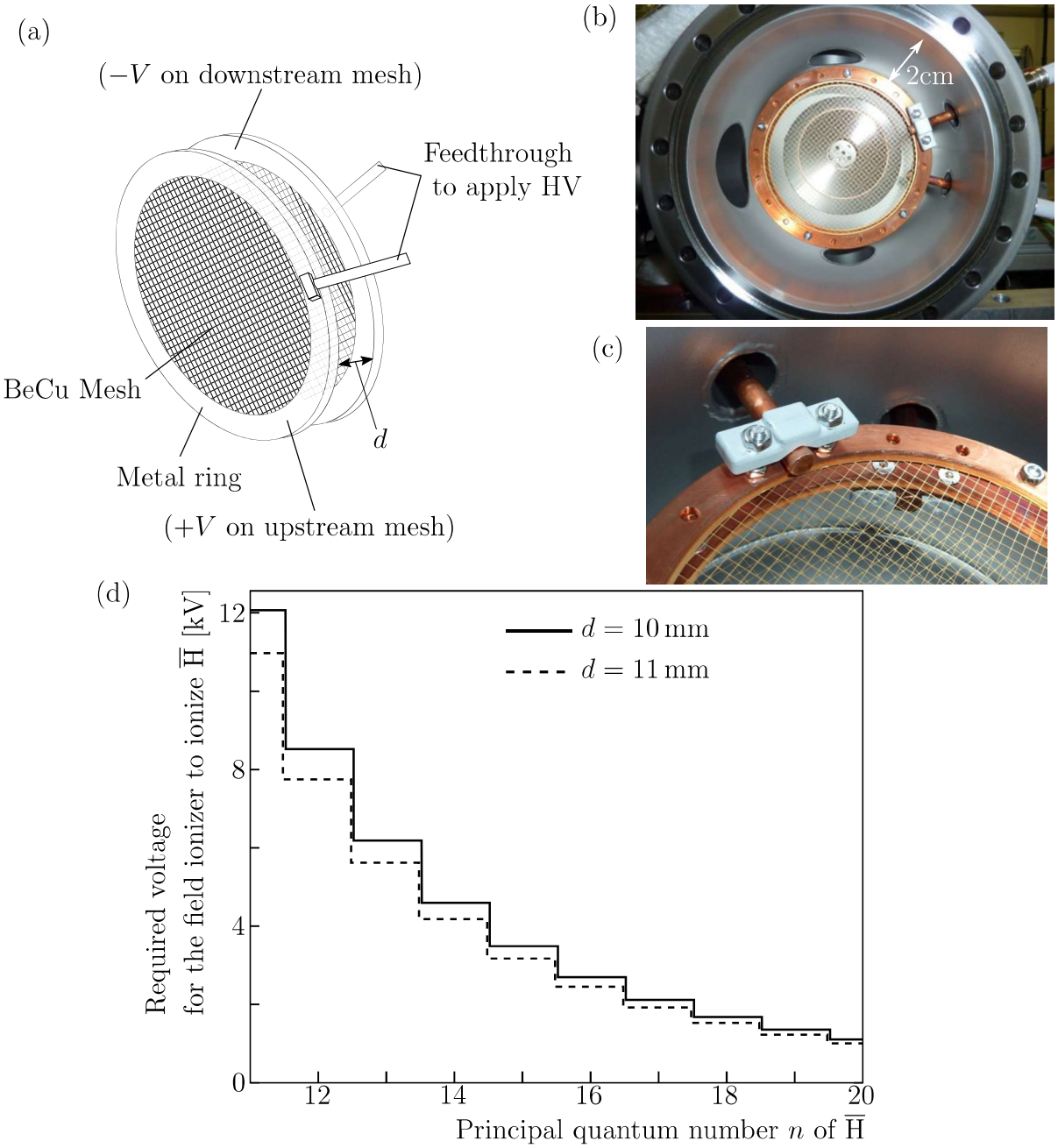

Figure 3.21: (a) A schematic drawing of the field ionizer mainly composed of two BeCu meshes with transparency of 95 % at a distance of 10.5 ± 0.5 mm. By applying a positive high voltage $+V$ on a mesh at upstream side and a negative high voltage $-V$ on the other mesh at downstream side, an uniform high electrostatic field is produced, which avoids bare antiprotons from travelling down to the antihydrogen detector. The principal quantum number of antihydrogen atoms can be monitored independently on the radial positions. (b) A picture of the actual setup. The metal ring around the metal mesh is distant from the surrounding duct surface by 2 cm. (c) A zoomed view of the coupling of the feedthrough and the ring. (d) A required voltage for the field ionizer to ionize an antihydrogen atom as a function of its principal quantum number n. Solid line and dashed line correspond to the distance between meshes of 10 mm and 11 mm, respectively. When ± 5 kV is applied, antihydrogen atoms of with $n \geq 14$ are ionized. Figures are adapted from [70].

3.1.6 Antihydrogen detector using the BGO with position sensitivity and hodoscope

This section contains what is expected to be published within 5 years.

3.2 Measurement of the energy distribution of antiprotons

The energy distribution of antiprotons at the exit of the MUSASHI trap, and at the injection point into the double cusp trap are measured.

3.2.1 Energy distribution just after the extraction from the MUSASHI trap

This section contains what is expected to be published within 5 years.

3.2.2 Energy distribution at the injection into the double cusp trap

This section contains what is expected to be published within 5 years.

3.3 Antihydrogen production in the double cusp trap with higher production rate

A typical mixing cycle is summarized as follows.

Figure 3.28 shows the potential configurations at the double cusp trap for preparation of positrons. Positrons are transported to the double cusp trap from the positron accumulator every 40 s repeatedly for 20 - 30 times until $\sim 10^8$ positrons are confined inside. Figure 3.28(a) shows that a potential well $\phi_{e^+\mathrm{catch}}$ is prepared and the upstream side of the well is opened for a short time and quickly switched back for positron catching. The rotating-wall electric field (3.2 MHz, 5V) is applied on positrons in the potential well during the accumulation. Figure 3.28(b) shows that the potential well $\phi_{e^+\mathrm{catch}}$ is changed to a nested-well configuration $\phi_{e^+\mathrm{evap}}$ after the positron accumulation. In order to increase the reproducibility, in other words, to keep the number of positrons and potential level within the positron plasma at the same level among different mixing cycles, more positrons than required are accumulated at first and then the excess is thrown away. Figure 3.28(c) shows that the upstream side of the nested well is opened until a certain level for a short time and switched back. Figure 3.28(d) shows that the potential configuration is shifted to the negative side $\phi_{e^-\mathrm{thr}}$ and then unintentionally trapped electrons at the local potential maxima at both sides of the positrons are thrown away by a potential manipulation. By shifting the configuration to the negative side, electrons have enough energy to go out of the nested well. The electrons can be produced via ionization of residual gas by injected positrons during the accumulation time of several tens of minutes. It should be removed because the electrons tend to coexist with antiprotons due to the same charge, cool down antiprotons without interaction with positrons, and enhance the axial separation between positrons and antiprotons which decreases antihydrogen yield. Finally the nested well configuration ϕ_{nested1} is prepared for antiproton injection as shown in Fig. 3.28(e).

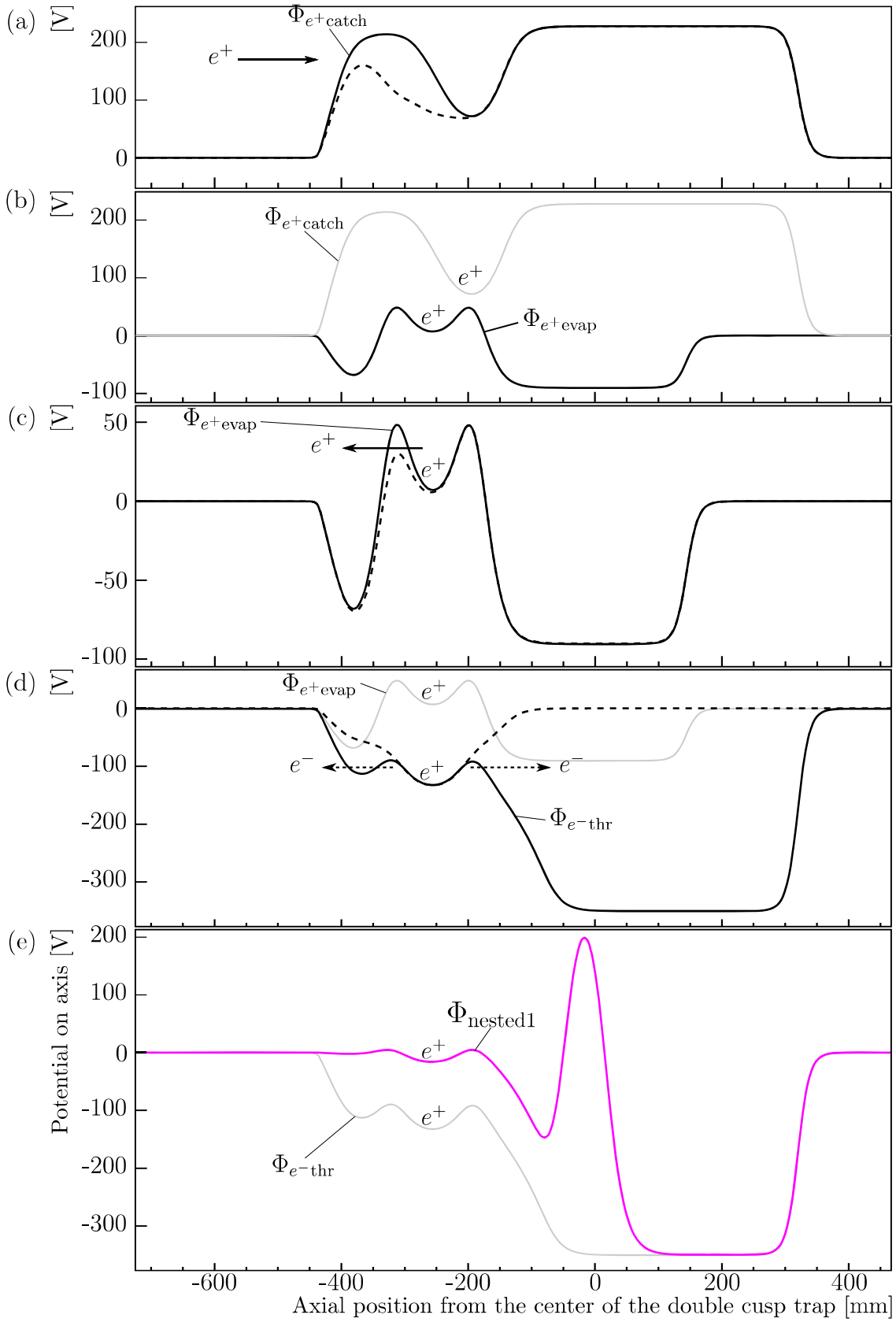

Figure 3.28: Potential configurations at the double cusp trap for preparation of positrons. They are transported from the positron accumulator every 40 s repeatedly and trapped in the double cusp trap (a), a nested-well configuration is prepared (b), part of positrons are thrown away in order to increase the reproducibility (c), the unintentionally trapped electrons at the local potential maxima at both sides of the positrons are thrown away (d), and then the nested well configuration is prepared for antiproton injection (e).

When antiprotons are injected into the double cusp trap, the upstream side of the nested well is opened by applying pulsed voltage and quickly switched back after antiprotons enter the double cusp trap as shown in Fig. 3.29(a). At the timing of the switch back, a part of them is out of the nested well on the point of entering inside because of the relatively long bunch length as described before. In order to avoid heating up of them by the applied pulse, the pulse height is optimized to be as small as possible, keeping the trapping efficiency high enough. The upstream edge of the nested well is deepened 50 ms after the injection of antiprotons in order to approximate a harmonic well at the upstream edge of the confinement region of the nested well for a stable confinement of antiprotons as shown in Fig. 3.29(b). The deepened nested well ϕ_{nested2} is kept for antihydrogen production. The mixing start is defined as the timing of the antiproton injection. The typical time duration of one mixing cycle is about 25 s.

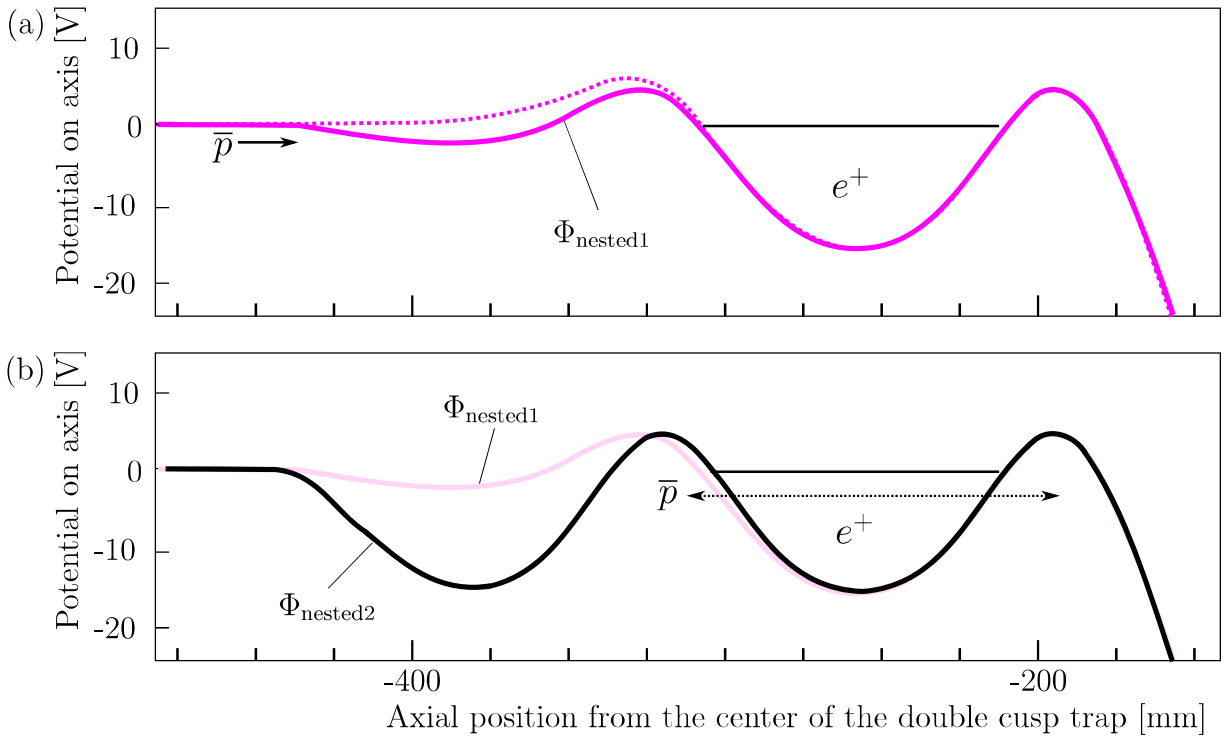

Figure 3.29: Potential configurations at the double cusp trap for injection of antiprotons to produce antihydrogen atoms. (a) When antiprotons are injected into the double cusp trap, the upstream side of the nested well is opened and quickly switched back. (b) The potential is modified from ϕ_{nested1} to ϕ_{nested2} after 50 ms in order to approximate a harmonic well at the upstream edge of the confinement region of the nested well for a stable confinement of antiprotons. ϕ_{nested2} is kept for antihydrogen production for 25 s as the typical time duration of one mixing cycle.

After 25 s of the mixing, the number of remained antiprotons are counted. The remained antiprotons are extracted as follows. The nested well is shifted to the negative side and then the downstream side of the nested well is opened slowly as shown in Fig. 3.30. Antiprotons which are not localized in the upstream side of the nested well are extracted to the downstream. They are expected to annihilate at the inner wall of the dcusp-MRE around zero magnetic field point and detected by surrounding AMT scintillator plates. Positrons in the center of the nested well is still kept confined.

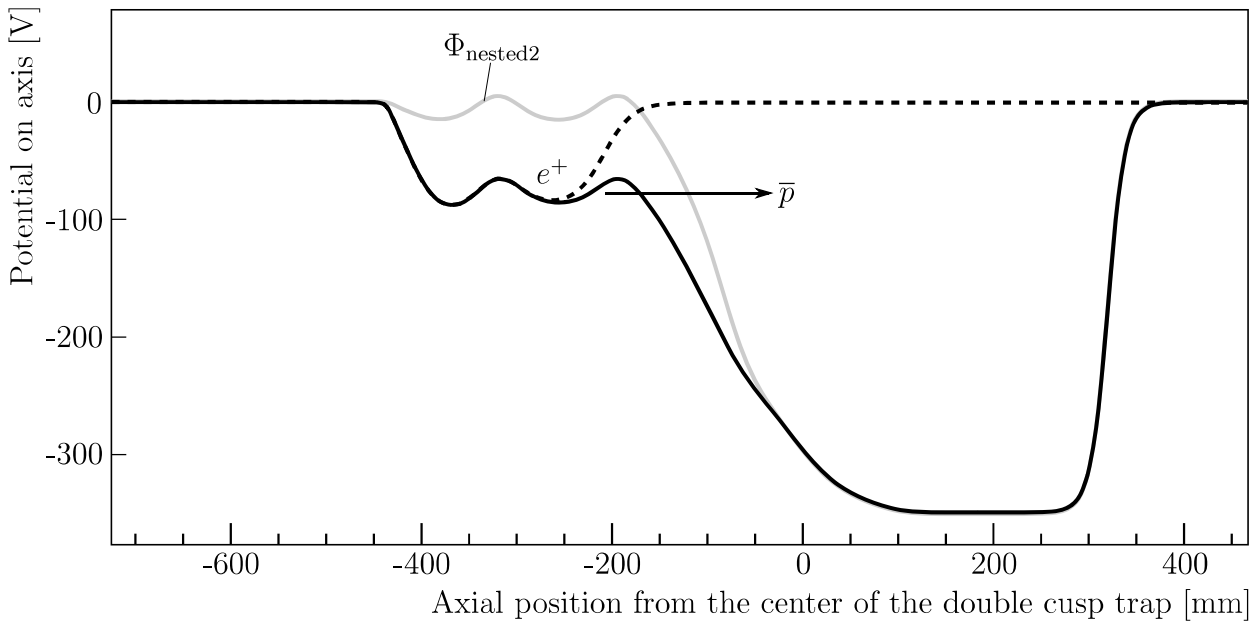

Figure 3.30: Potential configurations at the double cusp trap after mixing. The nested well is negatively shifted and the downstream side is opened slowly. Antiprotons which are not localized in the upstream side of the nested well are released.

At the last moment, the radius and the number of remained positrons are measured. The upstream side of the nested well is collapsed and positrons are confined in a harmonic well and then the positrons are extracted to the MCP-PS at the upstream side of the double cusp trap. The extracted number of positrons is quite stable without no significant loss during the mixing cycle. Therefore the remained positrons are reused for the next mixing cycle for several times. In order to keep the number of positrons, several accumulation cycles of positrons are added to the reused positrons instead of 30 times of accumulation cycles. The excess is thrown away as shown in Fig. 3.28(c). With this cycle of reuse and adding, the number of positrons are kept stable and the period of one run is greatly reduced. The averaged number and radius of positrons extracted after typical 27 mixing runs are 110 ± 4 million and 1.4 ± 0.2 mm.

Antihydrogen production is investigated at the double cusp trap by detection of annihilations.

Figure 3.32(a) shows AMT scintillator counts during 1 mixing averaged over 24 typical mixing cycles in order to evaluate annihilations within the double cusp trap, as a function of elapsed time from antiproton injection (mixing start). AMT scintillator counts increases especially for first several seconds of the mixing with positrons. Control experiments with the same procedures without positrons are also performed. Figure 3.31 shows a modified nested well called mimic potential which is prepared for the control experiments in order to imitate the potential level within a positron plasma as shown in Fig. 3.31. Otherwise, much less antiprotons can be trapped in the nested well because most of them are reflected at the potential barrier at the center of the nested well without the space charge of positrons. The AMT scintillator counts are averaged over 10 cycles as shown in Fig. 3.32(b). The increase in AMT scintillator counts for first several seconds is not observed for the mixing without positrons, which correspond to annihilations related to antihydrogen production. A small increase without positrons at the very first moment can be explained by the annihilations of antiprotons which are not confined in the nested well including those reflected at the entrance of the double cusp trap due to long bunch length and/or large radial position.

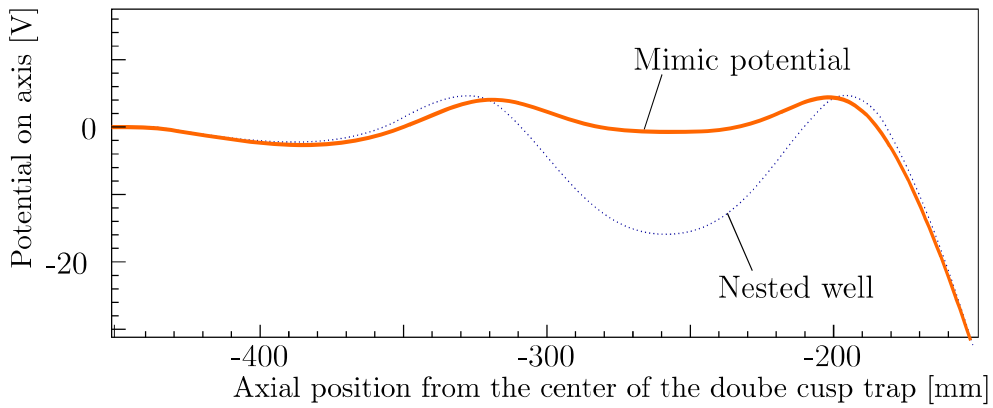

Figure 3.31: The electrostatic potential on axis called mimic potential to imitate the potential level within the positron plasma, which is used for measurements shown in Fig. 3.32(b).

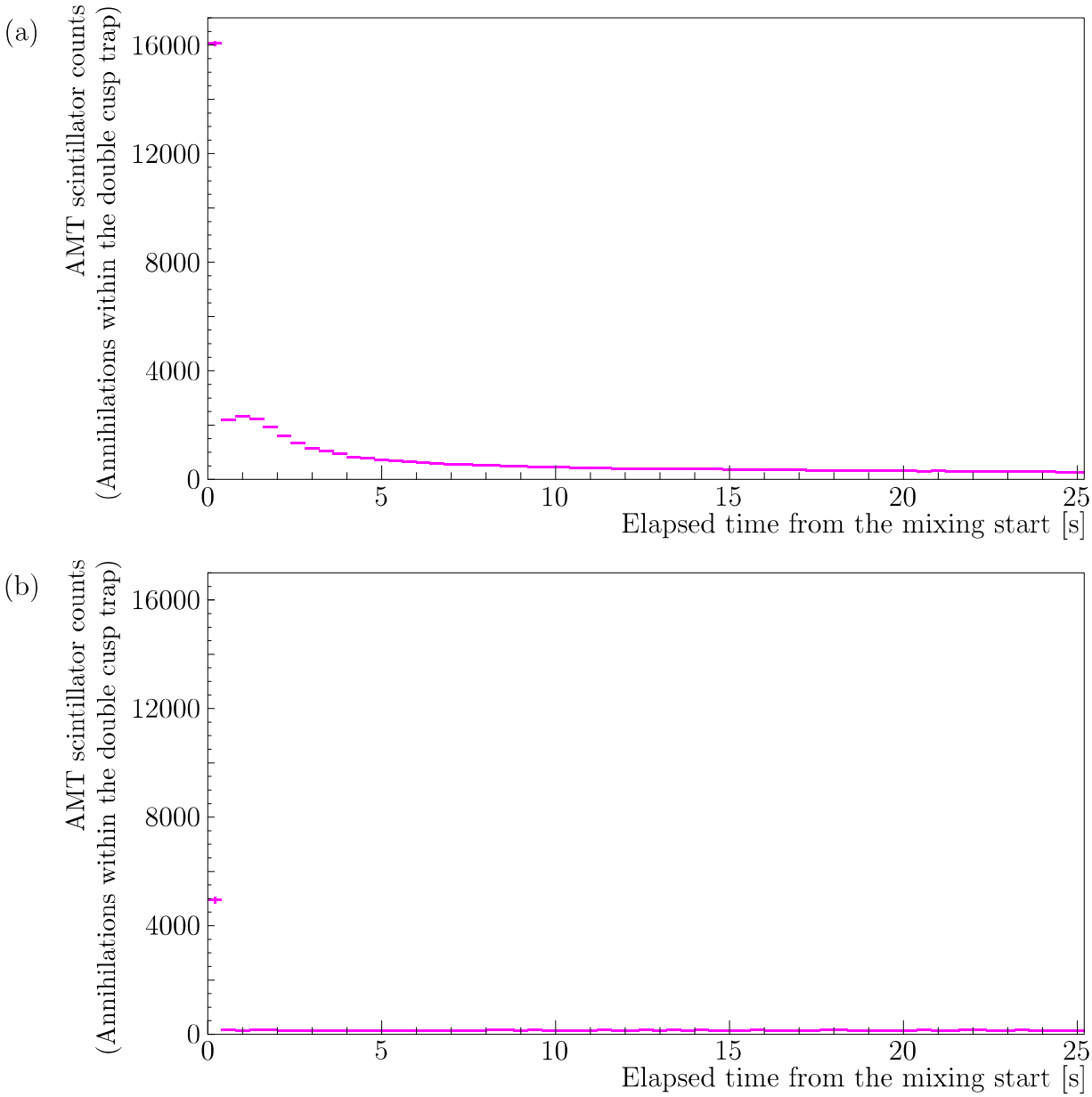

Figure 3.32: (a) The AMT scintillator counts during a typical mixing (averaged over 24 mixing cycles). (b) The AMT scintillator counts during a mixing without positrons (averaged over 10 cycles). AMT scintillator counts increases especially for first several seconds of the mixing with positrons, while the increase is not observed for the mixing without positrons, which correspond to annihilations related to antihydrogen production. A small increase without positrons at the very first moment can be explained by the annihilations of antiprotons which are not confined in the nested well including those reflected at the entrance of the double cusp trap due to long bunch length and/or large radial position.

The field ionization technique is also used to detect antihydrogen production inside the double cusp trap. Figure 3.33(a) shows the potential configurations with the nested well at upstream side, and the field ionization well at downstream side. Figure 3.33(b) and (c) show the axial magnetic field and the electric field strength on axis, respectively. When the trapped antihydrogen-oriented antiprotons in the field ionization well are released, they are expected to annihilate on the inner surface of the dcusp-MRE, at around zero magnetic field point.

The time structure of antihydrogen production is monitored by dumping trapped antihydrogen-oriented antiprotons in the field ionization well (FI well) periodically. Figure 3.34(a) shows a typical applied voltage on U1 electrode as a function of time where the FI well is prepared. When 350 V is applied, the FI well is kept, while trapped antihydrogen-oriented antiprotons in the FI well are dumped when -350 V is applied. As shown in Fig. 3.34(a), the FI well is kept for 0.5 s for first 4 cycles, and kept for 5 s for latter 4 cycles typically. The dump period is longer in the first four cycles due to technical limitations. Figure 3.34(b) shows a typical AMT scintillator counts at the timing of the first dump t_{dump1}. The number of field-ionized events per dump N_{FI} is defined as

$$N_{\mathrm{FI}} = N_s - N_b \times (20\,\mathrm{ms}/140\,\mathrm{ms}) \tag{3.12}$$

where the number of candidate events N_s is the sum of the filled region for 20 ms (from t_{dump1} to $t_{\mathrm{dump1}}+20$ ms) and the number of background events N_b is the sum of the filled region for 140 ms in total, for 80 ms (from $t_{\mathrm{dump1}} - 100$ ms to $t_{\mathrm{dump1}} - 20$ ms) and for 60 ms (from $t_{\mathrm{dump1}} + 40$ ms to $t_{\mathrm{dump1}} + 100$ ms). The factor of (20 ms / 140 ms) corresponds to the normalization factor of the background events.

Figure 3.34(c) shows the total number of field-ionized events (adding the number of field-ionized events per dump at each dumping cycle) as a function of time for the case of the typical mixing cycle. The antihydrogen production rate corresponds to the slope.

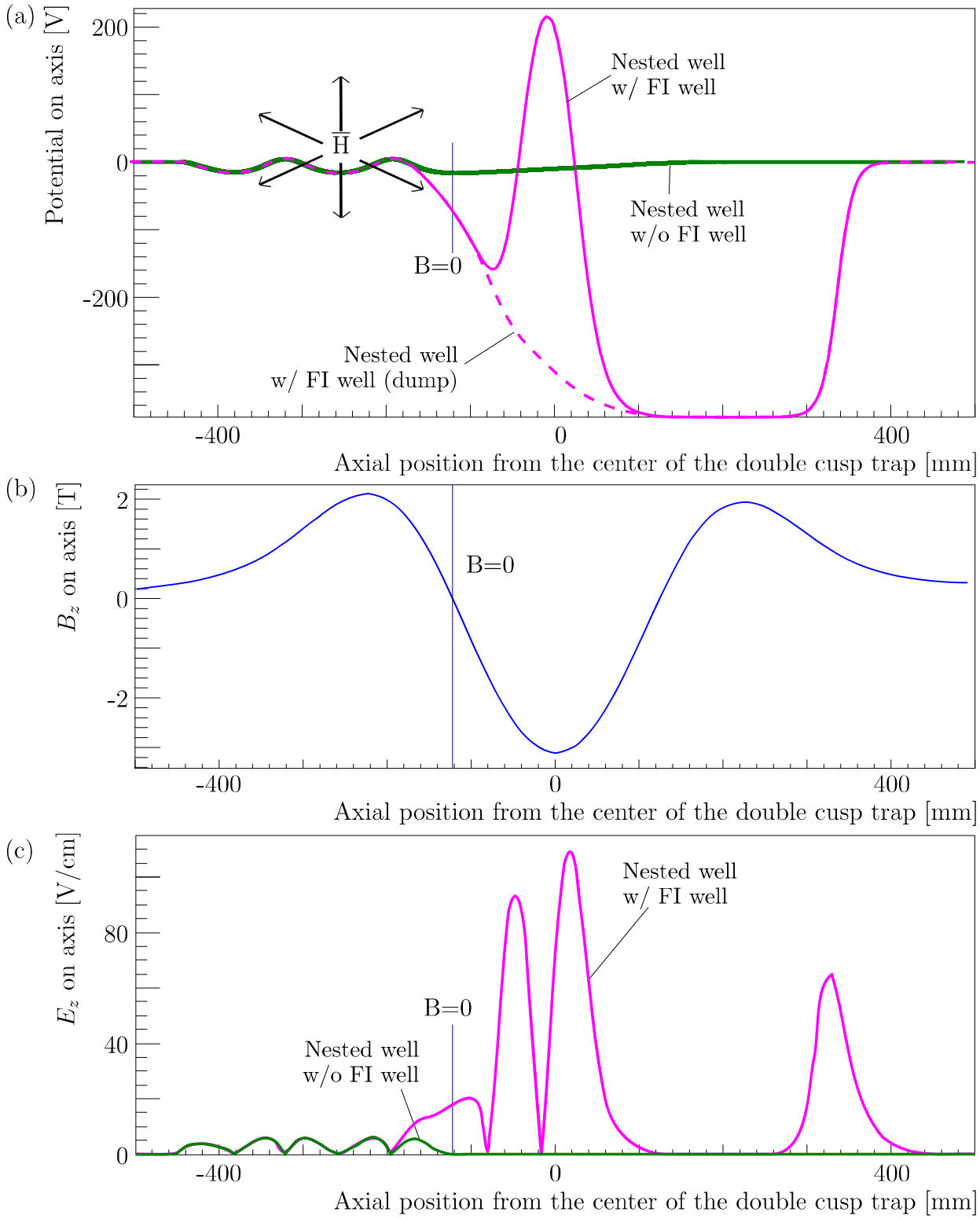

Figure 3.33: (a) Potential configurations at the double cusp trap for mixing. Magenta dotted lines show the nested well with the field ionization well (FI well). Magenta dashed lines show the potential configuration for dumping the trapped antihydrogen-oriented antiprotons inside the FI well. Green solid line show the nested well without the FI well. (b) The magnetic field along the axis at the double cusp trap. (c) The electric field along the axis. Magenta and green solid line correspond to the nested well with and without the FI well.

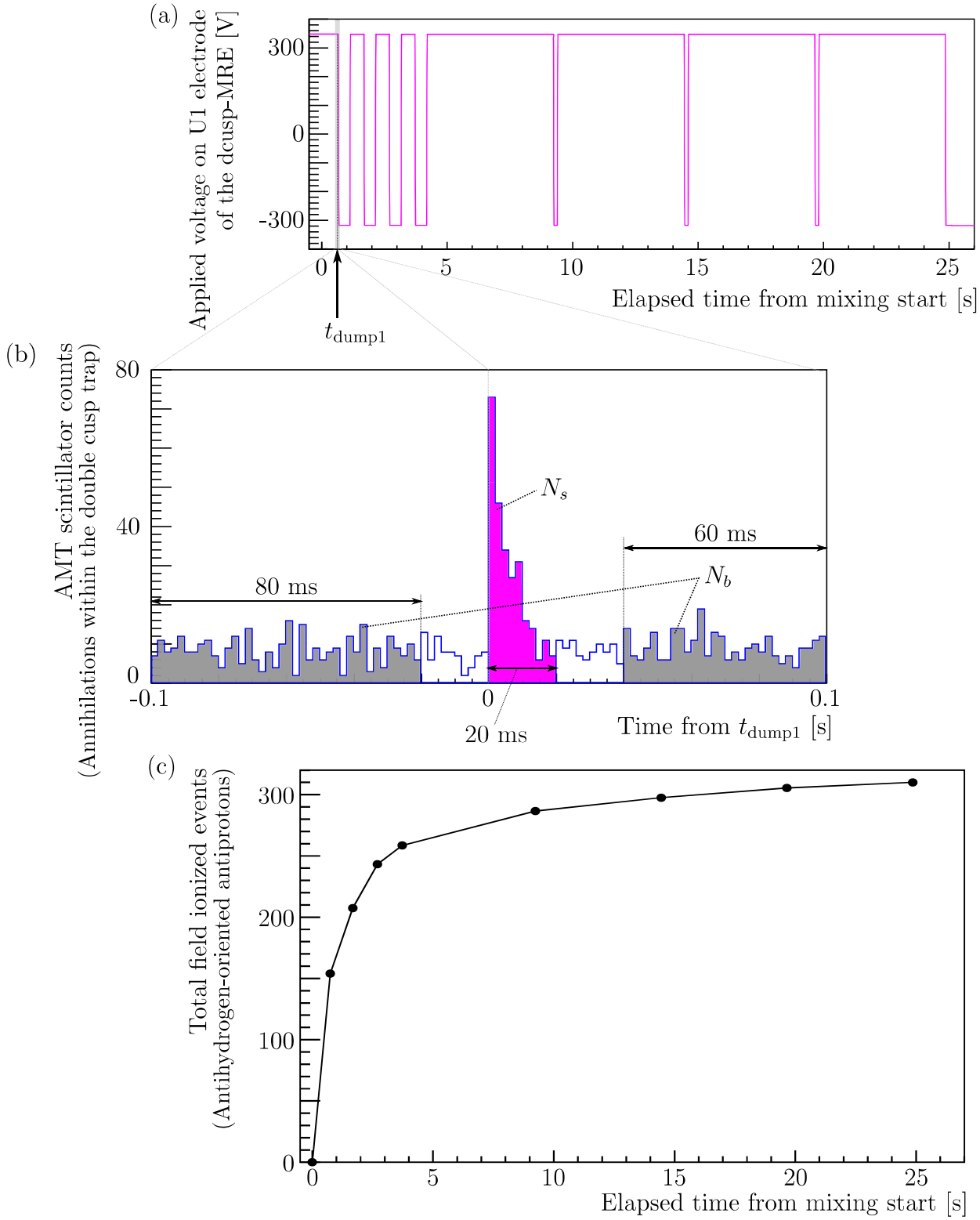

Figure 3.34: (a) The applied voltage on U1 electrode as a function of time for a typical dumping cycle. When 350 V is applied, the FI well is kept, while trapped antihydrogen-oriented antiprotons in the FI well are dumped when -350 V is applied. (b) The AMT scintillator counts at the timing of the first dump t_{dump1}. (c) The total number of field-ionized events (adding the number of field-ionized events per dump at each dumping cycle) as a function of time for the case of the typical mixing cycle. The antihydrogen production rate corresponds to the slope.

As described before, the relative energy between antiprotons and positrons is important to increase antihydrogen production rate and produce antihydrogen atoms with small kinetic energy. In order to minimize the relative energy, the potential level within positron plasma should be adjusted to the injection energy of antiprotons, in addition to the achieved antiproton injection with narrow energy spread. Although the potential level can be estimated from the number and the radius measured after the mixing, it is difficult to know the condition at the exact timing of the mixing start. Thus it is optimized experimentally as follows.

AMT scintillator counts and field-ionized events are measured as the nested well is shifted by V_s in order to optimize the level. The number of injected antiprotons are constant within ~ 10 %. Figure 3.35(a) shows AMT scintillator counts as a function of time for $V_s = -2, 0, 4$ V. Each histogram shows a drop in AMT scintillator counts and a delayed peak at several seconds after the mixing start. The drops and delayed peaks are shifted to a later time for larger V_s, which means larger relative energy. It is explained from the fact that heating of positrons is suppressed when the relative energy is small, which means the drop in production rate is suppressed.

Figure 3.35(b) shows the total number of field-ionized events as a function of time. It shows that the first increase in the field-ionized events is at maximum when $V_s = 0$ V and the fraction of a few seconds after mixing start grows as V_s increases. It can be explained as follows. As V_s increases, the potential barrier for injected antiprotons are lowered and more antiprotons can enter the positron plasma. However, the travelling time of antiprotons within the positron plasma becomes shorter because antiprotons are less decelerated. On the other hand, heating of positrons is increased as V_s increases. The dependence is determined by both effects. For example, the first increase in the field-ionized events is the smallest for $V_s = 4$ V due to heating of positrons while the total number is larger than that of $V_s = -2$ V because more antiprotons are trapped.

We set the relative level at $V_s = 0$ V because the first increase in the field-ionized events is the largest and the drop in AMT scintillator counts is not so large.

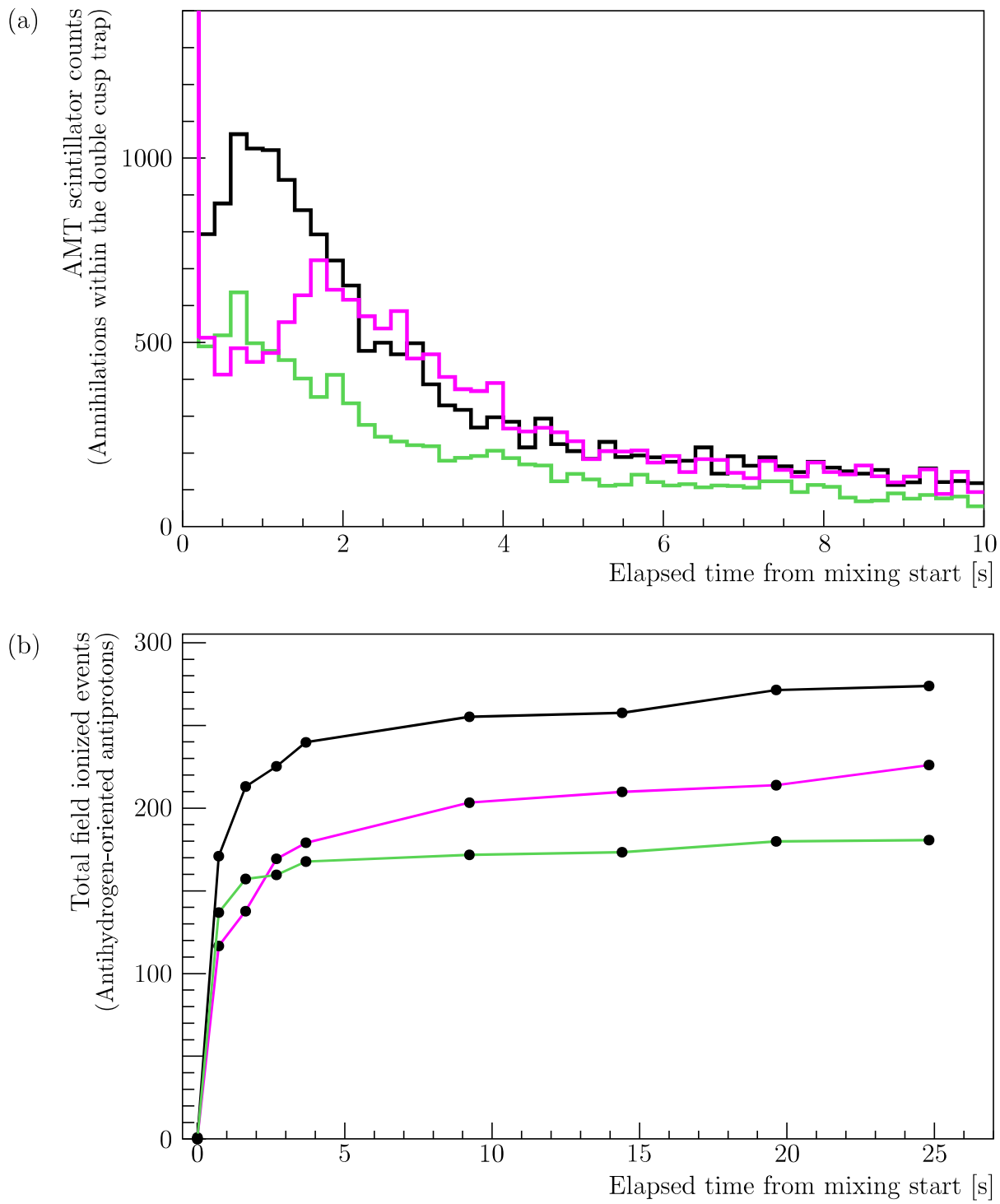

Figure 3.35: (a) The AMT scintillator counts as a function of time until 10 s from the mixing start. The green, black, magenta lines correspond to the mixing with $V_s = -2, 0, 4$ V, respectively. Each histogram shows a drop in AMT scintillator counts and a delayed peak at several seconds after the mixing start. The drops and delayed peaks are shifted to a later time for larger V_s due to heating of positrons. (b) The total number of field-ionized events as a function of time. The dependence is determined by the number of antiprotons entering the positron plasma, travelling time of antiprotons within the positron plasma, and heating of positrons. We set the relative level at $V_s = 0$ V because the first increase in the field-ionized events is the largest and the drop in AMT scintillator counts is not so large.

Figure 3.36 shows the total field-ionized events as a function of time, together with those measured in chapter 2. The new scheme corresponds to the adiabatic transport scheme explained in this chapter. The old scheme corresponds to the non-adiabatic transport scheme used in chapter 2. Although field-ionized events are counted by the AMT scintillator for the new scheme and by the array detector for the old scheme, the counts are normalized considering the detection efficiency so that they are comparable. The production rate increases drastically within 500 ms for the new scheme. The rate is larger than the value of the old scheme by a factor of 100 for the first 0.5 s. As described before, the energy spread of antiprotons is narrower by a factor of $\sim 1/100$ at the injection into the antihydrogen production region with the new scheme, compared with the old scheme as summarized in Tab. 3.7. The time evolution of antihydrogen production indicates that the heating of positrons is greatly reduced by the new scheme, keeping the relative energy small between positrons and antiprotons, which is the main target of this chapter as described at the beginning. This intense production of antihydrogen atoms can contribute to improvement of the S/N ratio of the detection of antihydrogen atoms at the antihydrogen detector because the main backgrounds are cosmic rays whose rate is constant.

In addition, antihydrogen atoms with small kinetic energy should be produced from the antiprotons with narrow energy spread by the new transport scheme. Considering that recombinations start when the velocity of positrons and antiprotons are comparable, the kinetic energy of antihydrogen atoms is primarily determined by the energy distribution of antiprotons. When recombinations in the nested well are considered, the velocity of antiprotons is determined by the relative energy against the potential level within the positron plasma. For example, it should be noted that recombinations can start even with the relative energy of several tens of eV assuming the positron temperature of 180 ± 50 K [56] and lead to production of antihydrogen atoms at several tens of eV. Assuming the injection energy of the antiproton beam is ideally optimized at the potential level within the positron plasma, the relative energy correspond to the energy spread of antiprotons, regardless of the value of the injection energy itself. Considering the relative energy of sub eV with the new scheme, the kinetic energy of antihydrogen atoms is expected to be smaller by a factor of 10 even if the optimization of the relative level varies within a few eV.

Table 3.7: A summary of the transport conditions of antiprotons. The new scheme corresponds to the adiabatic transport scheme explained in this chapter. The old scheme corresponds to the non-adiabatic transport scheme used in chapter 2.

Scheme	Float voltage at MUSASHI	Electrostatic lens	Magnetic field on axis			Energy spread of $\overline{p}$ at $\overline{\mathrm{H}}$ production region
			Coil T	Coil A	Coil B	
new	-1.5 V	w/o	0.15 T	0.12 T	0.12 T	$\sigma \sim 20$ eV
previous	-150 V	w/	-	0.012 T	0.012 T	$k_B T \sim 0.25$ eV

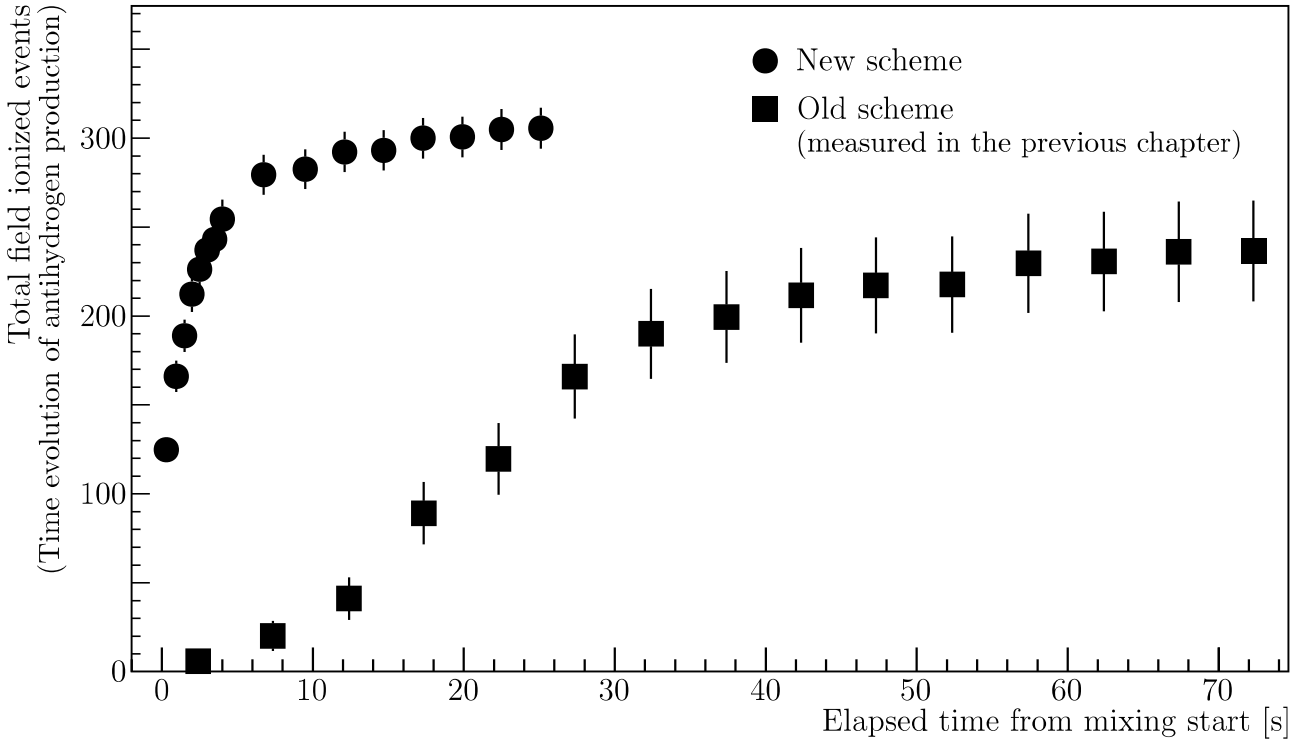

Figure 3.36: The total number of field-ionized events as a function of time with the new adiabatic transport scheme explained in this chapter (circle), together with those measured in chapter 2 with the old non-adiabatic transport scheme (square). Although field-ionized events are counted by the AMT scintillator for the new scheme and by the array detector for the old scheme, the counts are normalized considering the detection efficiency so that they are comparable. The time evolution of the antihydrogen production drastically changes. The production rate is larger than the value of the old scheme by a factor of 100 for the first 0.5 s. As described before, the energy spread of antiprotons is narrower by a factor of $\sim 1/100$ at the injection into the antihydrogen production region with the new scheme, compared with the old scheme as summarized in Tab. 3.7. The heating of positrons is greatly reduced by the new scheme, keeping the relative energy small between positrons and antiprotons, which is the main target of this chapter as described at the beginning. This intense production of antihydrogen atoms should improve the S/N ratio of the detection of antihydrogen atoms at the antihydrogen detector because the main backgrounds are cosmic rays which are propotional to the measurement time. Antihydrogen atoms with small kinetic energy are also expected.

3.4 Detection of antihydrogen atoms in low-lying excited states at the antihydogen detector

This section contains what is expected to be published within 5 years.

3.5 Possible non-isotropic distribution of antihydrogen atoms

This section contains what is expected to be published within 5 years.

3.6 Space-charge effect of positron plasma on trapping efficiency of antiprotons

It is generally expected that the higher the positron density is, the higher the production rate of antihydrogen atoms becomes. This is because the three-body recombination rate of antiproton and positron is propotional to the square of the positron density (Eq. 2.12). But it is observed that the increased positron density does not result in the increased number of antihydrogen atoms. Indeed, the number of trapped antiprotons in the nested well decreased with higher positron density. In this chapter, we discuss the reason behind this peculiar behaviour.

Figure 3.43 shows the number of trapped antiprotons in the nested well for three positron conditions, low density ($\rho \sim 1.0 \times 10^8\ e^+/\mathrm{cm}^3$), normal density ($\rho \sim 6.0 \times 10^8\ e^+/\mathrm{cm}^3$), and high density ($\rho \sim 8.0 \times 10^8\ e^+/\mathrm{cm}^3$) as a function of the injection energy of antiprotons to positron plasma. The three positron conditions are summarized in Tab. 3.9. The number of trapped antiprotons are measured by counting the number of remaining antiprotons in the downstream well of the nested well after the mixing (as explained in section 3.3, Fig. 3.30), and then doubled for compensating not-counted remaining antiprotons in the upstream well, assuming antiprotons are trapped in both upstream well and downstream well equally after mixing. The injection energy is defined as the relative energy of antiprotons to the potential level inside the positron plasma on the beam axis, and the estimation takes account of the space charge of the positron plasma. Figure 3.43 shows that the number of trapped antiprotons in the nested well with higher-density positron plasma is almost half of that with normal-density plasma. The dependence on the injection energy becomes weak as the density becomes higher.

Table 3.9: Summary of three positron conditions.

Case	Total number	Density	Radius
Lower	60×10^6	$1.0 \times 10^8/\mathrm{cm}^3$	2.0 mm
Normal	120×10^6	$6.0 \times 10^8/\mathrm{cm}^3$	1.0 mm
Higher	190×10^6	$8.0 \times 10^8/\mathrm{cm}^3$	1.1 mm

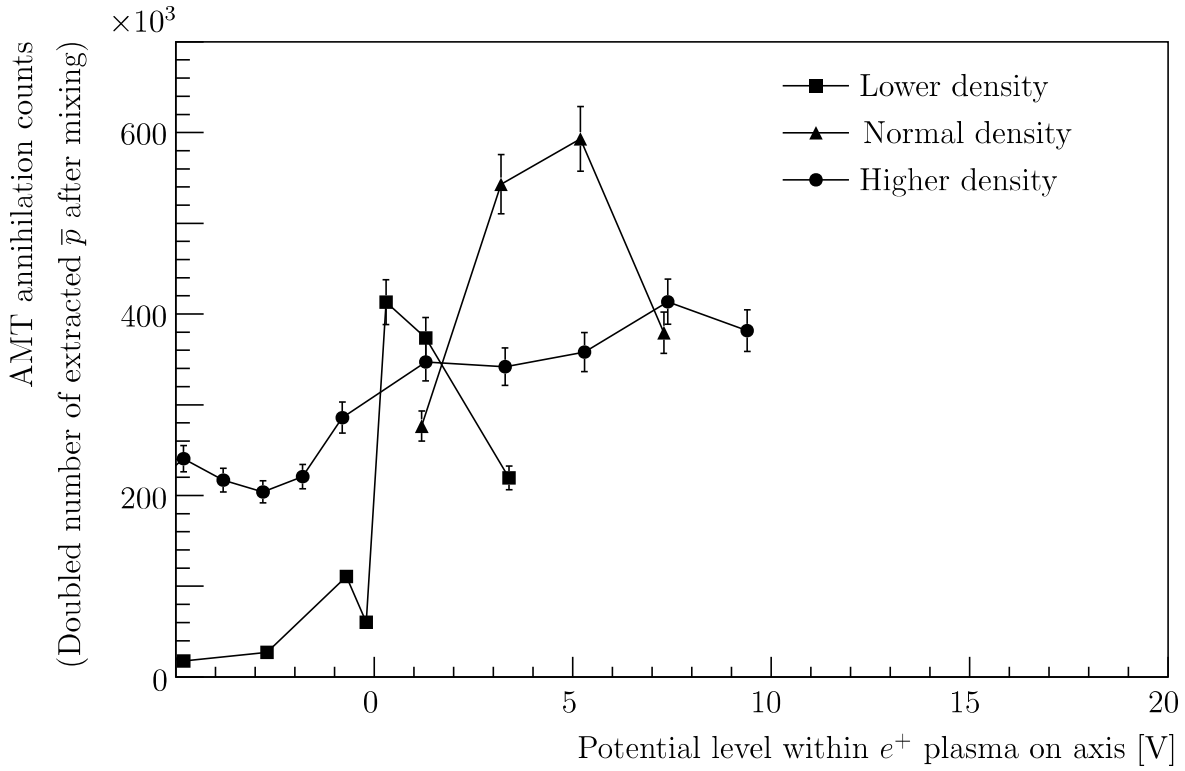

Figure 3.43: The number of trapped antiprotons in the nested well for three positron conditions, low density, normal density, and high density (summarized in Tab. 3.9) as a function of the injection energy of antiprotons to positron plasma. The number of trapped antiprotons in the nested well with higher-density positron plasma is almost half of that with normal-density plasma. The dependence on the injection energy becomes weak as the density becomes higher.

This peculiar behavior can be explained by effect of the space charge of positron plasma on the injection energy of off-axis antiprotons. Figure 3.44(a) shows two-dimensional electrostatic potential distribution around the center of the nested well with positron plasma with normal density of 6×10^8 e^+/cm^3 is stored. We assume that the positron plasma is in a rigid-rotor equilibrium. Contour lines are shown every 0.5 V and the potential increases as the filled color becomes from blue to yellow. It is noted that the electrostatic potential inside the positron plasma is flat on axis, but not so off-axis. There is also a difference between the potential on axis and off axis. Similar calculations are carried out for positron plasmas with high and low densities, and Fig. 3.44(b) shows the results of the radial dependence of the electrostatic potential at the center of the nested well. Black dotted, solid, and dashed lines correspond to positron plasma with low, normal, and high density, respectively. Magenta vertical lines show the radius of each positron plasma. The filled region shows the possible radius of antiprotons entering inside the dcusp-MRE without hitting the surrounding materials. For each density, we assumed rigid-rotor equilibrium for the positron plasma, with the potential depth of its virtual harmonic well is set to the difference between the plateau and the bottom of the nested well potential on axis. We note that the effective relative energy of antiprotons with respect to the potential on axis is different at each radial position of antiprotons. For example, the difference at $r = 1$ mm is 3 V compared to the potential plateau on axis for normal-density positron plasma, which is 10 times larger than the energy spread of injected antiprotons.

In order to investigate the effect of space charge on the trapping efficiency, trajectories of antiprotons in the nested well are calculated for each positron density. In the trajectory calculation, the antiprotons are assumed to be uniformly distributed within a spheroid with radius of 3 mm and length of 50 mm, and to have a temperature of 3000 K before being injected to the nested well. Trajectories are calculated with the static magnetic field and electric field, including the float voltage at the MUSASHI trap of -1.5 V and the modified potential inside the double cusp trap. The number of trapped antiprotons are estimated as the number of antiprotons which survive and are within the double cusp trap by the time the upstream side of the potential well is closed to confine antiprotons. In the calculation, we close the potential well after 155 μs from injection, same timing as the experiment.

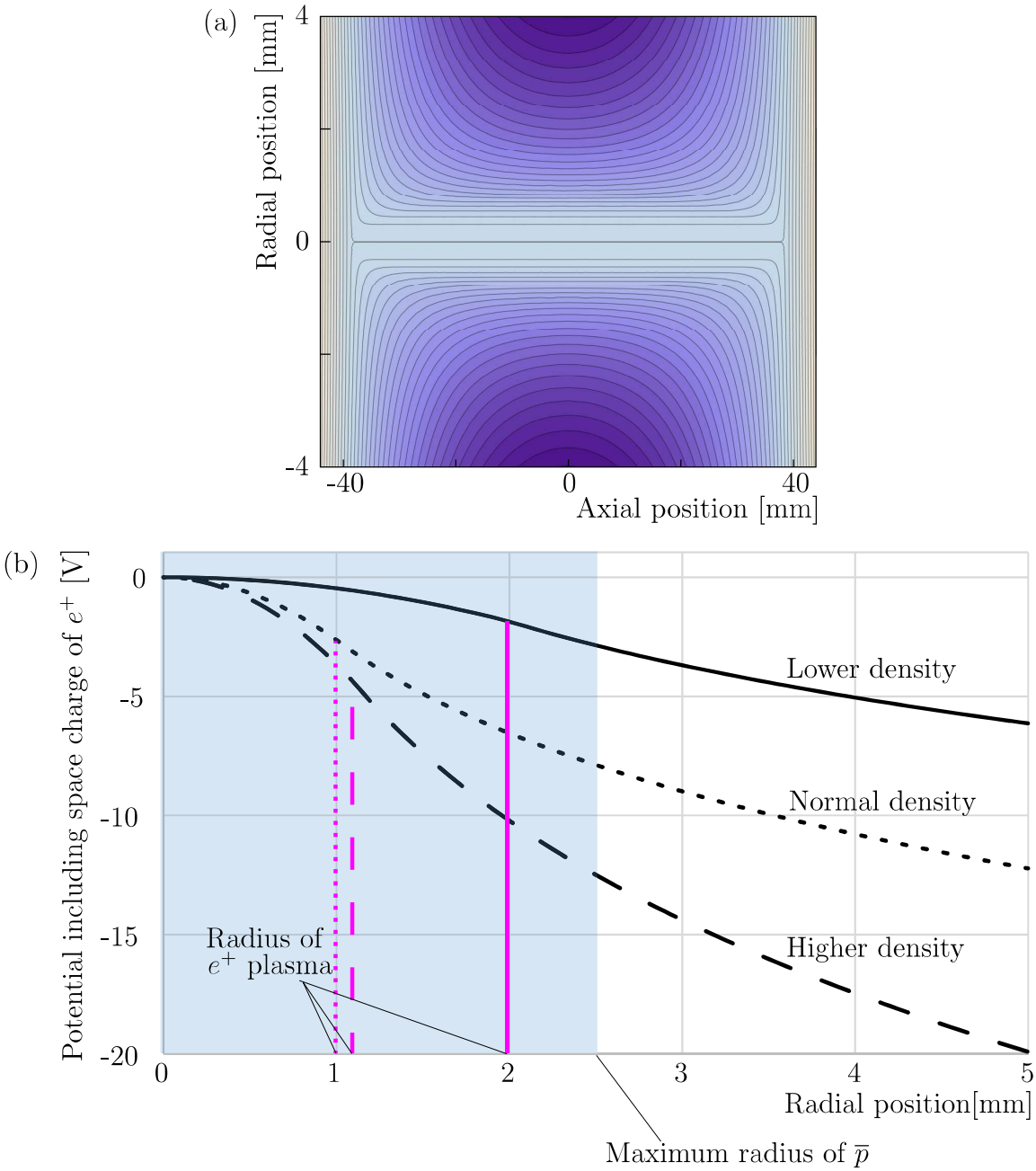

Figure 3.44: (a) The two-dimensional electrostatic potential distribution around the center of the nested well with positron plasma with normal density is stored, assuming that the positron plasma is in a rigid-rotor equilibrium. Contour lines are shown every 0.5 V and the potential increases as the filled color becomes from blue to yellow. (b) The radial dependence of the electrostatic potential at the center of the nested well. Black dotted, solid, and dashed lines correspond to positron plasma with low, normal, and high density, respectively. Magenta vertical lines show the radius of each positron plasma. The filled region shows the possible radius of antiprotons entering inside the dcusp-MRE without hitting the surrounding materials. We note that the effective relative energy of antiprotons with respect to the potential on axis is different at each radial position of antiprotons.

Figure 3.45(a) shows the estimated number of trapped antiprotons as a function of the potential plateau on axis. When the plateau level is lower than the float voltage, most of the antiprotons are reflected by the nested well, and not trapped. When the kinetic energy of antiprotons is close to the potential level of within the positron plasma, the antiprotons' speed becomes slower, and their travelling time within the double cusp trap becomes longer. This makes the number of trapped antiprotons higher. When the kinetic energy far exceeds the potential level, the antiprotons move fast, and reflected by the downstream side of the nested well and escape toward upstream before the trap is closed. This results in the decrease of the number of trapped antiprotons.

We note that the lower the density of positron plasma becomes, the steeper the change of number of trapped antiprotons in both simulations (Fig. 3.45(a)) and measurements (Fig. 3.45(b)). It is also noted that the maximum number of trapped antiprotons with high density plasma is about half of that with normal-density plasma in both simulations and measurements. These observations can be explained by the radial dependence of the modified potential because of the space charge of positron plasma. As shown in Fig. 3.44(b), the potential barrier for antiprotons at around the center of the nested well is the lowest on axis and becomes higher as going away from the axis, and the difference is larger for high density positron plasma. This means that the effective spread of the injection energy of antiprotons with finite radial size becomes broader for high-density plasma. This broader energy spread of the antiprotons is responsible for the lower maximum trapping efficiency of antiprotons with high density positron plasma, because antiprotons close to the fringe of the positron plasma will be reflected back by the positron plasma when the potential level is at the best condition for the antiprotons on axis, and the antiprotons close to the axis will escape the nested well as they travel at faster speed when the potential level is at the best condition for the antiprotons at the fringe. The broader energy spread makes trapping efficiency less dependent of the potential level on axis.

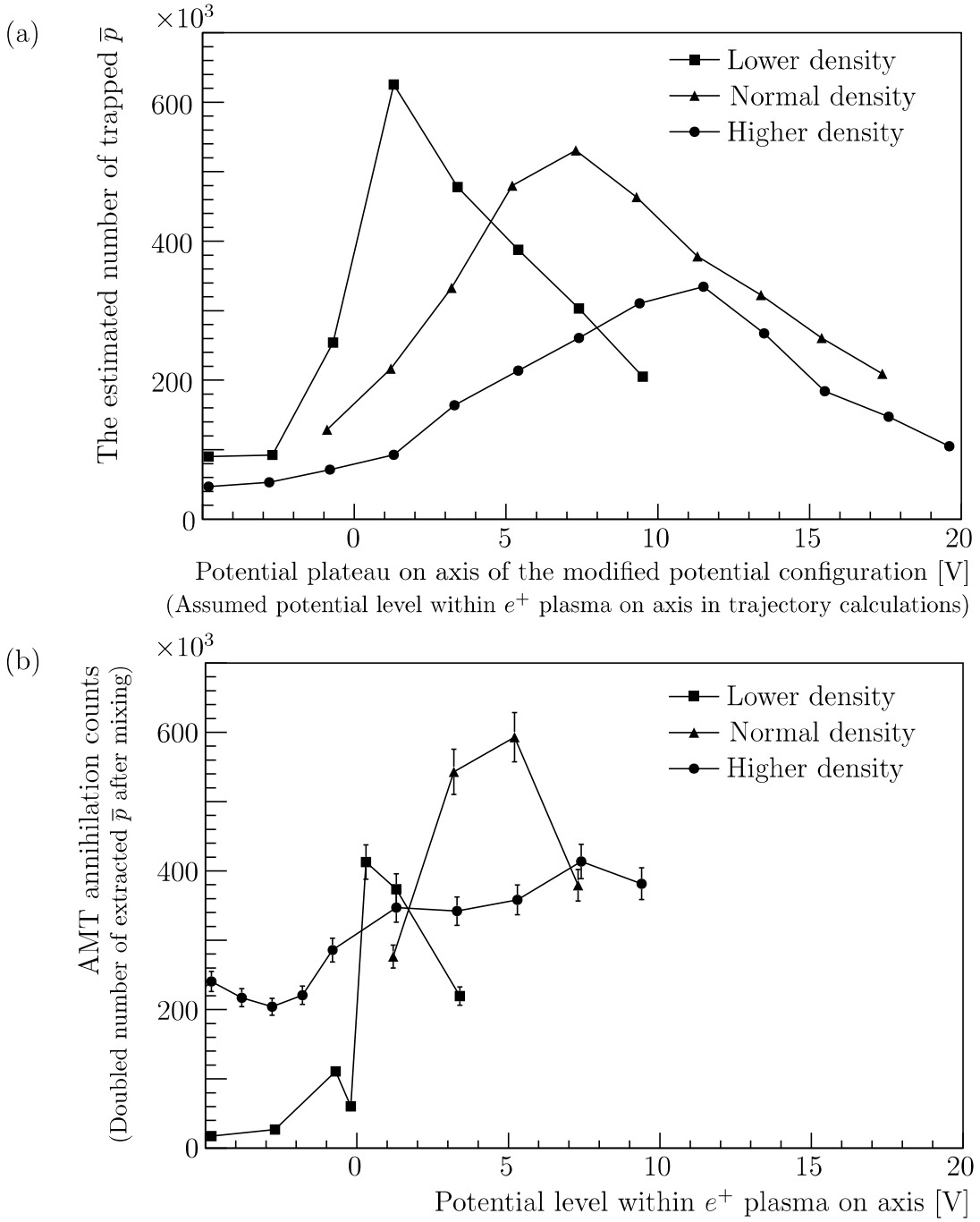

Figure 3.45: (a) The estimated number of trapped antiprotons as a function of the potential plateau on axis. (b) The number of trapped antiprotons measured after mixing (same as Fig. 3.43). In both simulations and measurements, the lower the density of positron plasma becomes, the steeper the change of number of trapped antiprotons, and the maximum number of trapped antiprotons with high density plasma is about half of that with normal-density plasma.

The large effective energy spread of the incoming antiprotons causes undesirable heating of positron plasma. This effect is estimated by considering the energy transfer between antiprotons and positrons. Assuming the radial motions and axial motions of positrons are well coupled, the change of the temperature of antiprotons and positrons can be expressed as [50]

$$\frac{dE_{\overline{p}}(t)}{dt} = -S(T_e(t), E_{\overline{p}}(t)), \tag{3.14}$$

$$\frac{dT_e(t)}{dt} = \frac{2}{3k_B}\frac{S(T_e(t), E_{\overline{p}}(t))}{N_e} - \frac{T_e(t)}{\tau_{rad}} \tag{3.15}$$

where $E_{\overline{p}}$ and T_e is the temperature of antiprotons and positrons, S is the energy transfer rate. The second term of Eq.(3.15) represents the cooling due to cyclotron radiation. In following calculation, the initial temperature of positron plasma is set to 0.01 eV ($\sim$ 116 K).

Figure 3.46(a) shows the calculated temperature of normal-density positron plasma as a function of elapsed time from the start of mixing, when the potential of the positron plateau is set to 3.2 V. The inner subfigure shows a zoomed view of the first 0.01 second. The temperature rises from the initial temperature ($\sim$ 116 K) to its maximum ($\sim$ 135 K) within the first a few ms and recovers to the initial temperature after a few seconds. Figure 3.46(b) shows the maximum temperature of the positron plasma of each density as a function of the positron plateau level. The temperature of low-density plasma increases up to $\sim$ 350 K, while there is much less increase of the temperature of high-density plasma. This is mainly because the difference of the number of positrons which shared the excess energy brought by antiprotons.

Once the trapping efficiency of the antiprotons and the temperature of the positron plasma is calculated, one can estimate the number of synthesized antihydrogen atoms, assuming the recombination rate is propotional to $\rho_{e^+}^2 T_{e^+}^{-4.5}$. Figure 3.47(a) and (c) show the estimated number of produced antihydrogen atoms within first 0.7 second and within 25 second, respectively. Figure 3.47(b) and (d) show the measured field-ionized events at 1st dump and the total field-ionized events, corresponding to the two calculations above. We note that our calculation roughly reproduce the trend of the measured data, in which the number increases at first as the potential plateau is increased, and then decrease gradually after the peak. But the largest discrepancy lays in the ratio of the number of antihydrogen produce in 25 sec and that produced in first 0.7 sec. In calculation, the number of antihydrogen produced in first 25 sec is about 50 times larger than that produced in first 0.7 sec, whereas in the observation, the ratio is an order of two to three. This discrepancy can be qualitatively explained by the spatial separation

of antiprotons and positrons described in Sec. 3.7.

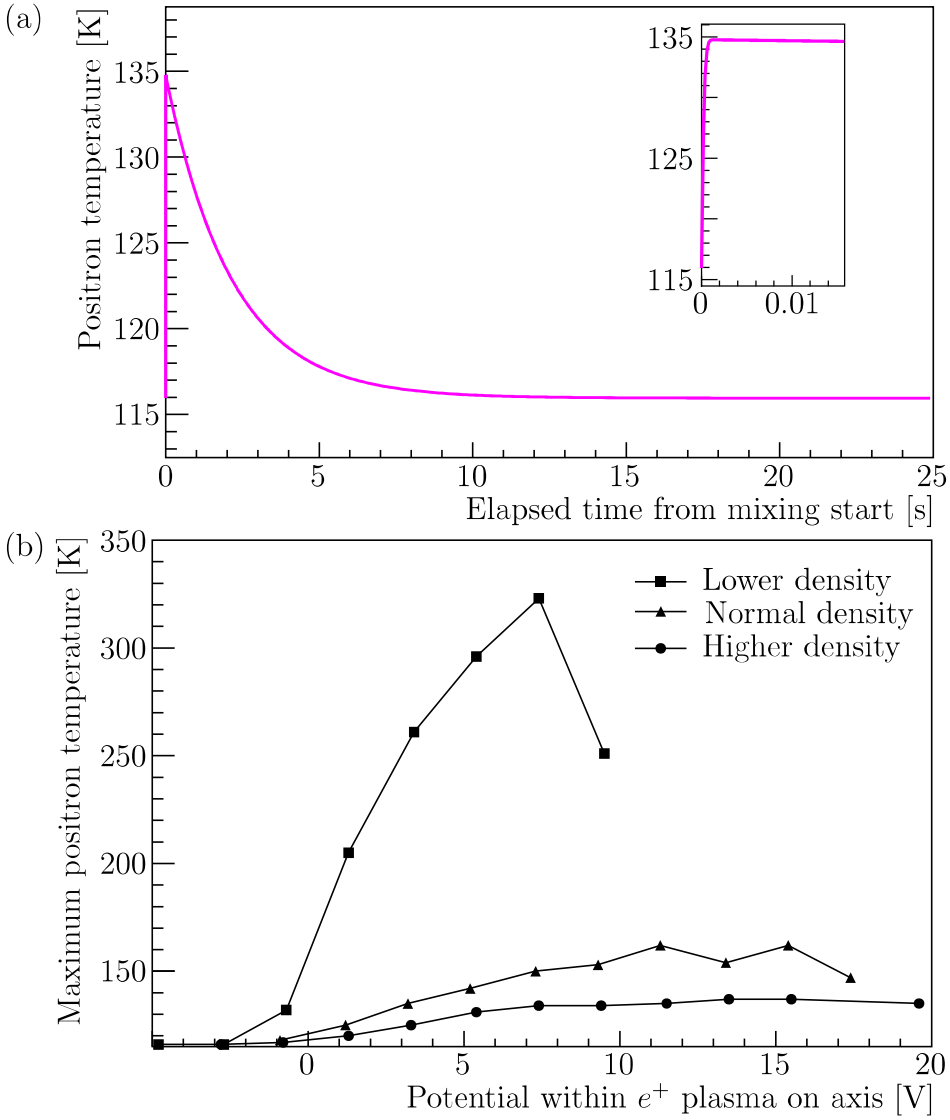

Figure 3.46: (a) The calculated temperature of normal-density positron plasma as a function of elapsed time from the start of mixing, when the potential of the positron plateau is set to 3.2 V. The inner subfigure shows a zoomed view of the first 0.01 s. The temperature rises from the initial temperature ($\sim$ 116 K) to its maximum ($\sim$ 135 K) within the first a few ms and recovers to the initial temperature after a few seconds. (b) The maximum temperature of the positron plasma of each density as a function of the positron plateau level. The temperature of low-density plasma increases up to $\sim$ 350 K, while there is much less increase of the temperature of high-density plasma.

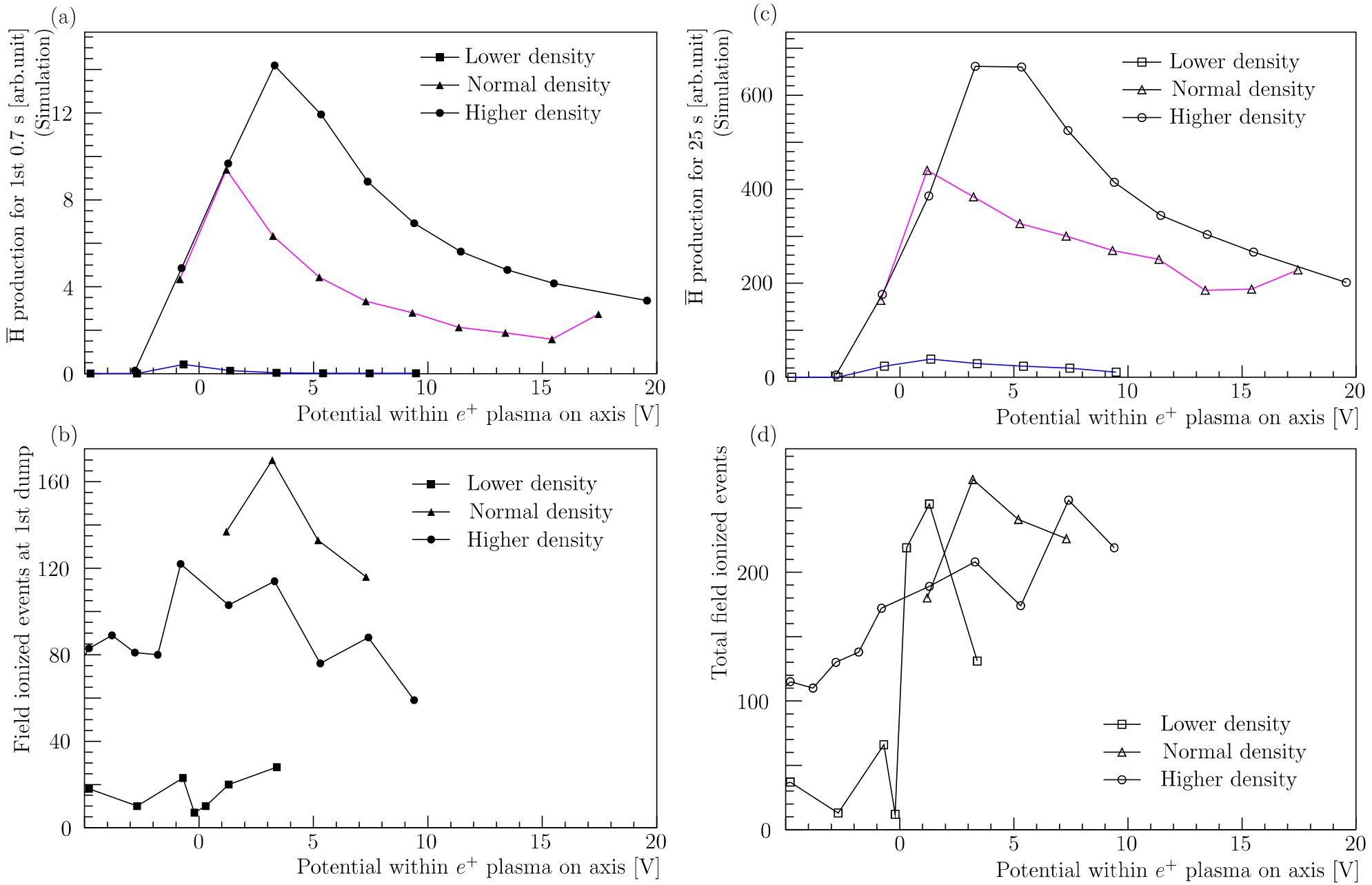

Figure 3.47: (a) and (c) show the estimated number of produced antihydrogen atoms within first 0.7 second and within 25 second, respectively. (b) and (d) show the measured field-ionized events at 1st dump and the total field-ionized events, corresponding to the two calculations above.

3.7 Separation between antiprotons and positrons

As described in chapter 3.3, we observe intense production rate of antihydrogen immediately after the antiprotons are injected into positrons in the nested trap and the mixing between antiprotons and positrons starts. But it is observed that the rate of the production quickly decrease within a few seconds. We suspect this is because antiprotons lose their energy fast, and they become trapped in two potential minima (where electric potential are highest) neighboring the positrons thus spatially separated each other. In order to investigate this problem quantitatively, the number of antiprotons trapped in the potential well on the downstream side of the nested well is measured as follows. Figure 3.48(a) show the operation of the potential configurations. Upper left figure shows the initial status in the measurement. The region filled with red corresponds to antiprotons. Some of them are travelling back and forth withing the nested well, the rest are trapped in two potential minima on the upstream side and the downstream side of the area where positrons are trapped. Next, the upstream side of the nested well is opened. The antiprotons travelling within the nested well, and the trapped in the upstream side are released. Then the downstream side of the nested well is slowly opened so that the antiprotons trapped in the downstream side are released slowly. They annihilate at the zero-magnetic field point because they travel along the magnetic field lines. The number of annihilation are counted by AMT scintillators. This operation is repeated while changing the timing of the opening of the upstream side of the nested well. Figure 3.48(b) show the operation of the potential configurations to measure the number of the antiprotons initially trapped in the nested well. All of the trapped antiprotons are released slowly downstream, and the number of annihilation are counted by AMT scintillators.

Assuming antiprotons are trapped in equal numbers in the upstream and downstream side of the nested well, the fraction of antiprotons which contribute to production of antihydrogen are estimated. Figure 3.49 shows the fraction as a function of time. It shows that only approximately 30 % of antiprotons are available for antihydrogen production after initial 500 ms, which means around 70 % of antiprotons are spatially separated from positrons. The same tendency is observed regardless of the positron density.

A possible origin of the cooling process of antiprotons is electrons in antiproton cloud, which have same sign of charge, thus could coexist in same region. But the number of trapped electrons with antiprotons is measured to be around 5×10^4, which is 10 times less than the number of antiprotons. It is difficult to explain the quick cooling and separation solely by the

electron cooling of antiprotons estimated by Eq.(3.15).

It is also shown in Fig. 3.49 that the speed of separation is much slower when there is no positrons in the nested well. In this measurement, a mimic potential to approximate the space charge of positron is prepared and same procedure explained above is repeated. This result shows the separation of antiprotons is closely related to interaction between antiprotons and positrons.

Another possible explanation is this is caused by the change of effective potential for antiprotons because of the radial expansion of the positron plasma. Figure 3.50(a) shows the radial profile of the positron plasma immediately after it is confined at the center of the nested well potential, while Fig. 3.50(b) shows the profile obtained after a typical mixing run. Table 3.10 shows the summary of the number of positrons and the radius of the positron plasma for both cases after several measurements. This radial expansion can be caused by the Diocotron instability excited by antiproton injection [75]. When the radius of the positron plasma becomes large, the density of the plasma decreases, and the space charge effect decreases, which increase the effective potential barrier for antiprotons at the center of the nested well. The antiprotons could be pushed into the potential minima, and spatially separated from positrons. This hypothesis explains why the rapid separation happens only when positrons are in the nested well, but more detailed study is needed to understand the rapid separation.

Table 3.10: Comparison of radius and the number of positrons.

Timing	Number of e^+	Radius of e^+ plasma	Averaged cycles
Just after confinement	110 ± 10	0.73 ± 0.03 mm	20
After mixing	110 ± 4	1.5 ± 0.2 mm	27

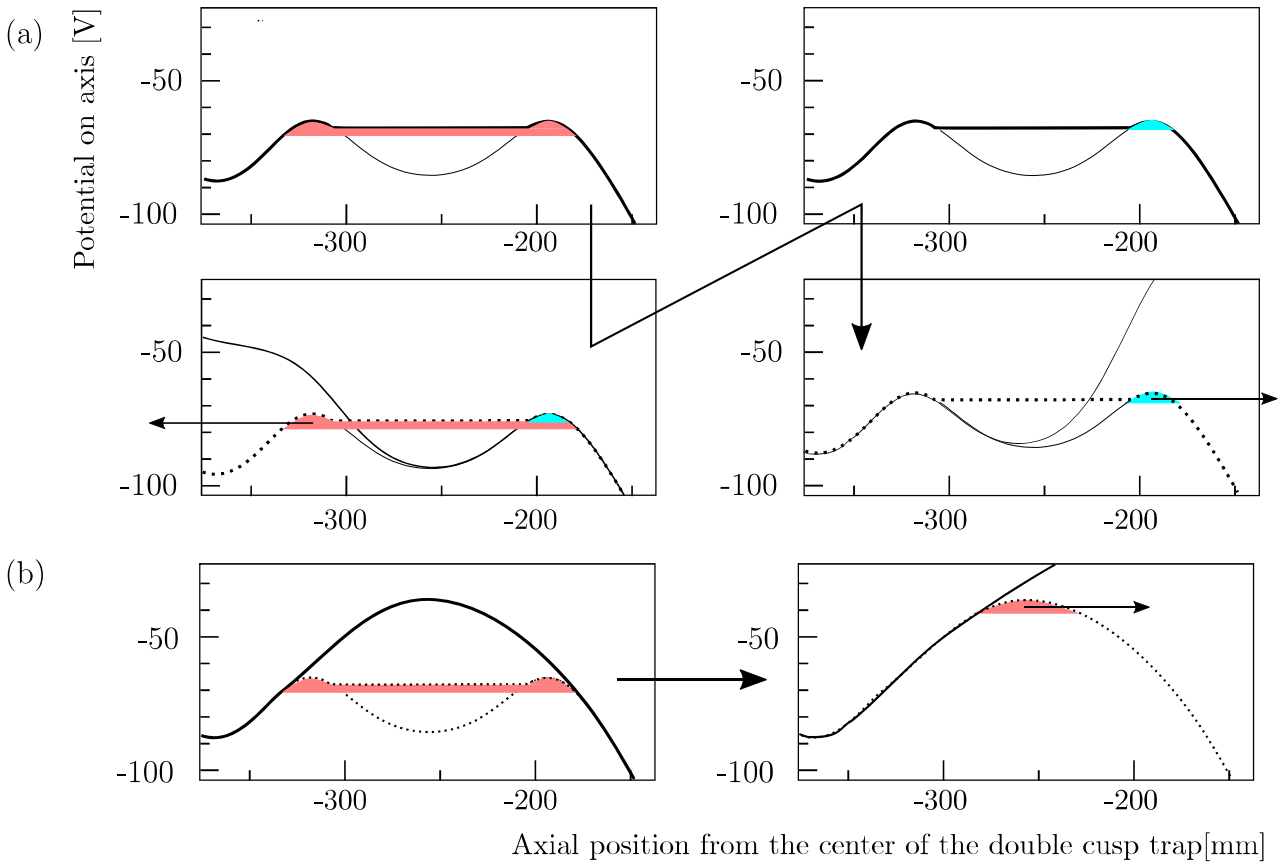

Figure 3.48: (a) The operation of the potential configurations in order to measure the number of antiprotons trapped in the potential well on the downstream side of the nested well. Upper left figure shows the initial status in the measurement. The region filled with red corresponds to antiprotons. Some of them are travelling back and forth withing the nested well, the rest are trapped in two potential minima on the upstream side and the downstream side of the area where positrons are trapped. Next, the upstream side of the nested well is opened. The antiprotons travelling within the nested well, and the trapped in the upstream side are released. Then the downstream side of the nested well is slowly opened so that the antiprotons trapped in the downstream side are released slowly. (b) The operation of the potential configurations in order to measure the number of the antiprotons initially trapped in the nested well. All of the trapped antiprotons are released slowly downstream.

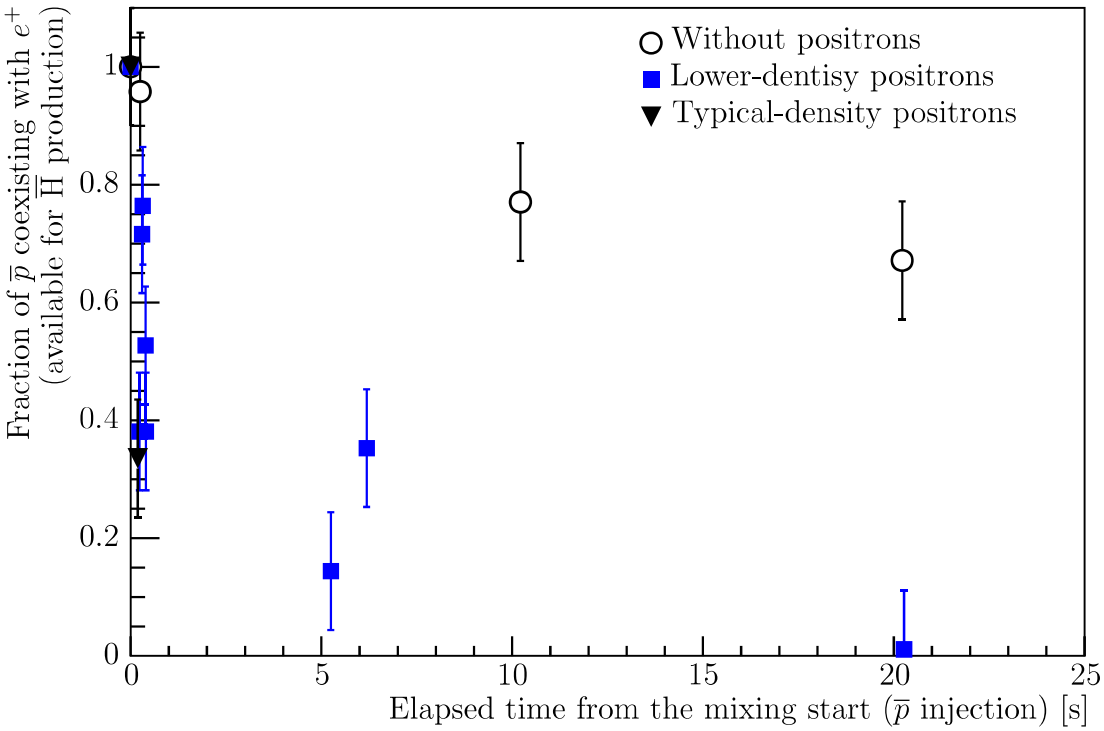

Figure 3.49: The fraction of antiprotons which contribute to production of antihydrogen are estimated as a function of time, assuming antiprotons are trapped in equal numbers in the upstream and downstream side of the nested well. Only approximately 30 % of antiprotons are available for antihydrogen production after initial 500 ms, which means around 70 % of antiprotons are spatially separated from positrons. The same tendency is observed regardless of the positron density. The speed of separation is much slower when there is no positrons in the nested well.

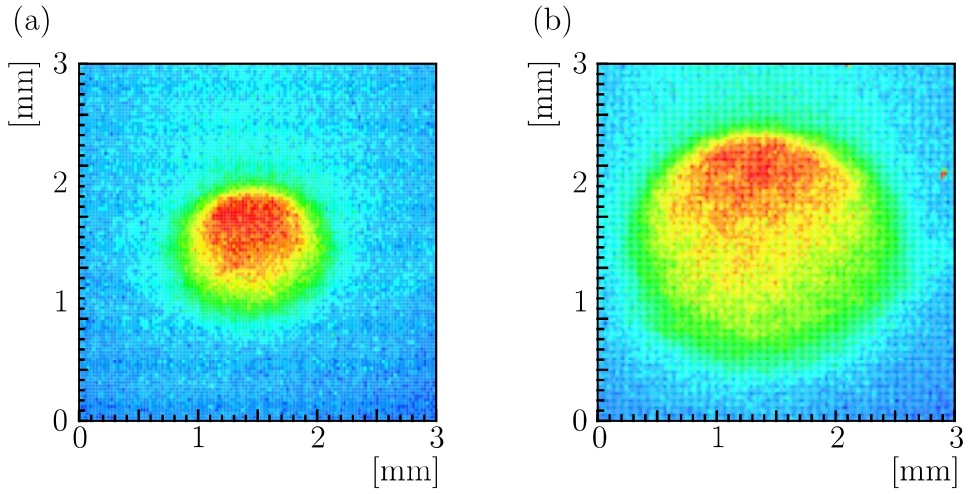

Figure 3.50: (a) The radial profile of the positron plasma immediately after it is confined at the center of the nested well potential. (b) The radial profile of the positron plasma obtained after a typical mixing run.

3.8 Future prospects

The goal of our experiment is to measure the hyperfine splitting of the ground state of antihydrogen atom with relative uncertainty of 10^{-6} or 1.4 kHz. The number of antihydrogen atoms required for this purpose is estimated as following [35].

For the measurement of the ground-state hyperfine splitting of hydrogen atoms in an equivalent apparatus described in chapter 1, the statistical precision δ for σ_1 transition given by Eq.(1.16)

$$\delta \sim \frac{1}{T_{\rm int}\sqrt{N}}\frac{\sigma_R}{\Delta_R} \tag{1.16}$$

where $T_{\rm int}$ is the interaction time which in our case, the travelling time through the cavity, N is the number of the frequency data points, Δ_R is the count rate drop, and σ_R is the average error bar of a data point in the spectrum. σ_R/Δ_R is given by

$$\frac{\sigma_R}{\Delta_R} \sim \frac{\sqrt{N_{\overline{\rm H}}}}{\frac{1}{2}\frac{1}{2}\frac{2p}{p+1}N_{\overline{\rm H}}} \tag{3.16}$$

where $N_{\overline{\rm H}}$ is the total number of events at the antihydrogen detector, p is the spin-polarization. Here we assume that at the microwave cavity, the half of antihydrogen atoms are in the ground state, and the other half are in the state with $F = 1,\ m = 1$. The spin-polarization is given by

$$p = \frac{f_{\rm LFS} - f_{\rm HFS}}{f_{\rm LFS} + f_{\rm HFS}} \tag{3.17}$$

as described before and the reduction factor in Eq.(3.16) is given by

$$\frac{2p}{p+1} = \frac{f_{\rm LFS} - f_{\rm HFS}}{f_{\rm LFS}}. \tag{3.18}$$

For the antihydrogen atoms with kinetic energy of 50 K, the spin-polarization of the antihydrogen beam extracted from the double cusp trap is approximately 45 % as shown in Fig. 3.12(b). $1/T_{\rm int}$ in Eq.(1.16) is 8.5 kHz for the length of our microwave cavity. Assuming that we take eight data points in a resonance curve, we need 250 events for each point, in total of 2000 $\overline{\rm H}$ events to measure the frequency of a transition with 1.2 kHz uncertainty. We need frequencies of four resonances to determine the hyperfine splitting at zero magnetic field, so 8000 $\overline{\rm H}$ events are required.

Although at this stage, we know neither the exact kinetic energy nor spin-polarization

of antihydrogen, we consider the assumption made above is reasonable. We can obtain the required number of antihydrogen in a few months beamtime by increasing the number of events per mixing by a factor of 10.

3.8.1 A proposal for higher yield

As shown in previous sections, the production rate is greatly increased, but the total yield of antihydrogen is limited by the spatial separation between antiprotons and positrons. We could use the RF excitation technique to suppress the separation, but it is not appropriate for the purpose of spectroscopy, because it randomly heats up the antiprotons, making the relative energy between antiprotons and positrons larger. It is difficult to produce antihydrogen atoms with small kinetic energy with the RF excitation.

We propose a modified mixing scheme shown in Fig. 3.51 in order to compensate the separation between antiprotons and positrons without heating. The basic idea is that we "recycle" the separated antiprotons so that all of the antiprotons contribute to the production of antihydrogen. First, the center of the nested well where positrons are confined are negatively shifted. Antiprotons are injected and trapped in the upstream side of the nested well. Trapped antiprotons are slowly injected into positrons by potential manipulations. After mixing, part of antiprotons are expected to be trapped mainly in the upstream side of the nested well in this configuration. By repeating this cycle, the remained antiprotons are able to contribute to antihydrogen production again. Considering that in our current scheme, the number of produced antihydrogen atoms is only about 5 % of the number of antiprotons remained after mixing, we can expect more than 10-fold increase of the yield of antihydrogen using this modified mixing scheme.

This proposed scheme has another advantage. Since the potential barrier is minimum on axis when antiprotons are slowly injected from the upstream side into positrons, the center part of antiprotons are primarily extracted. After the center part is extracted, antiprotons are expected to be redistributed for stability including the center part. By carefully adjusting the speed of the operation, antiprotons can be extracted continuously along the trap axis, which means the effective radius of antiprotons can be smaller. Considering the radial dependence of the space charge potential of positrons as described before, the effective relative energy between antiprotons and positrons is expected to be reduced, which leads to antihydrogen production with small kinetic energy. In addition, the excitation of Diocotron instability of the positron plasma which causes the expansion of positrons can be suppressed by injecting antiprotons along the symmetry axis of the positron plasma.

The proposed mixing scheme should yield higher number of antihydrogen atoms with smaller kinetic energy, and benefit the spectroscopy experiment greatly.

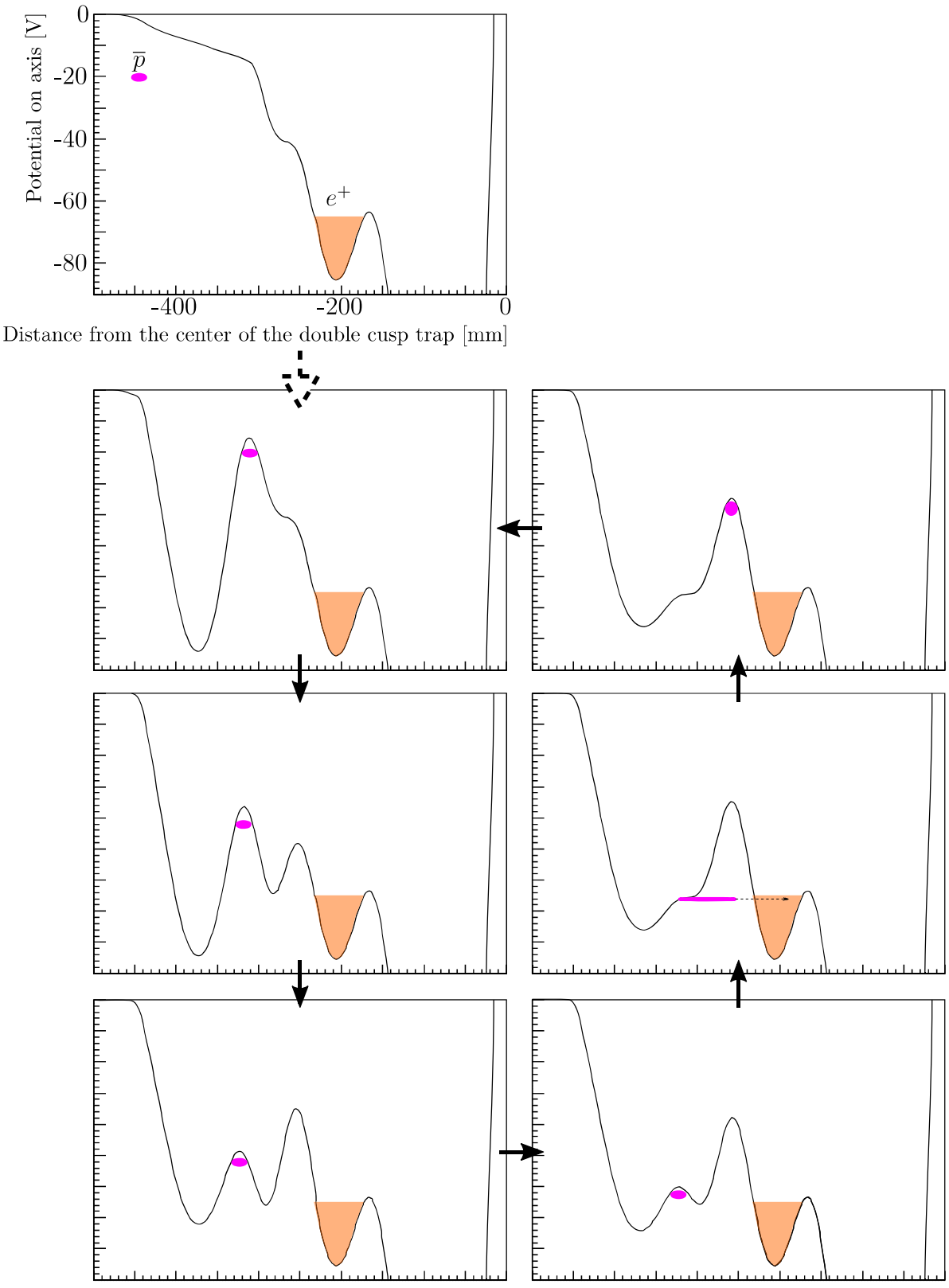

Figure 3.51: The modified mixing scheme in order to compensate the separation between antiprotons and positrons without heating ("recycle"). First, the center of the nested well where positrons are confined are negatively shifted. Antiprotons are injected and trapped in the upstream side of the nested well. Trapped antiprotons are slowly injected into positrons by potential manipulations. After mixing, part of antiprotons are expected to be trapped mainly in the upstream side of the nested well in this configuration. By repeating this cycle, the remained antiprotons are able to contribute to antihydrogen production again.

3.8.2 A proposal to increase antihydrogen population in low-lying states

Figure 3.38 shows most of antihydrogen atoms are in high Rydberg states. More population in ground state should lead to higher precision of the spectroscopy.

The population of antihydrogen atoms in ground state can be increased by lowering the positron temperature according to the calculation using classical-trajectory Monte Carlo (CTMC) method [76]. Figure 3.52 shows the calculated dependence. Considering the experimental condition of $\rho_e \sim 6\times10^8$ cm^{-3} and the estimated positron temperature before mixing at 200 K [56], the number of ground-state antihydrogen atoms increases by a factor ~ 50 if the positron temperature decreases from 200 K down to 100 K. One possibility is evaporative cooling [77] of positrons to decrease the temperature. Positrons are assumed to follow the Maxwell Boltzmann distribution at thermal equilibrium. If only hot components are removed, positrons are redistributed until thermal equilibrium. They follow a new Maxwell Boltzmann distribution with lower temperature. Since the number of positrons is decreased with the evaporative cooling, mixing conditions should be optimized carefully.

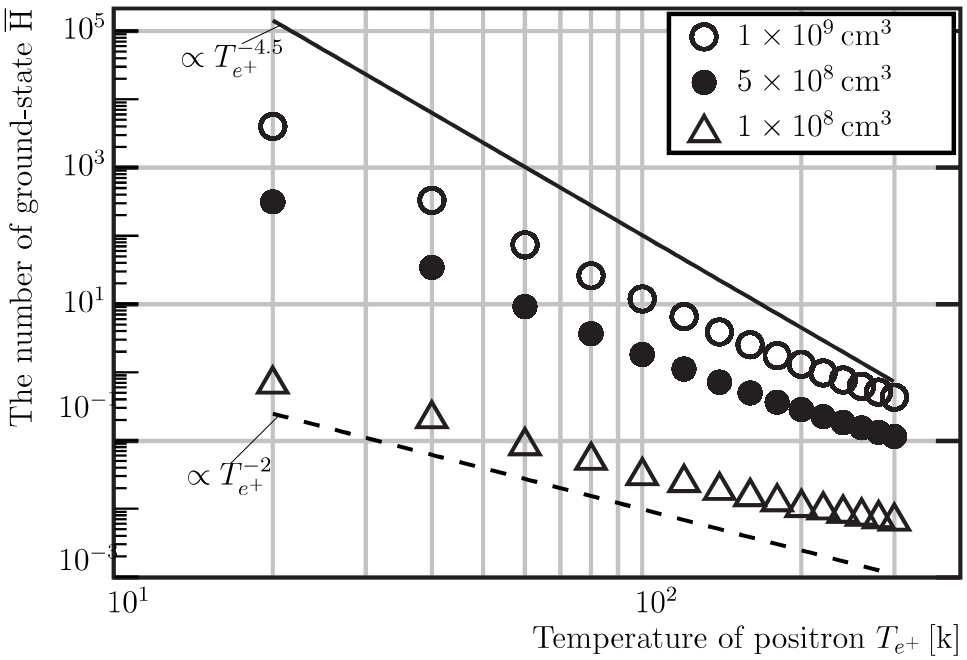

Figure 3.52: The number of ground-state antihydrogen atoms as a function of positron temperature 10 μs after mixing start, adapted from [76]. Different markers correspond to the positron density ρ_e of 1×10^9 cm^{-3} (open circle), 5×10^8 cm^{-3} (filled circle), and 1×10^8 cm^{-3} (open triangle), respectively. Considering the experimental condition of $\rho_e \sim 6\times10^8$ cm^{-3} and the estimated positron temperature before mixing at 200 K, the number of ground-state antihydrogen atoms increases by a factor ~ 50 if the positron temperature decreases down to 100 K.

In addition to the above prediction, the population of antihydrogen atoms in ground state can be increased as the length of the positron plasma becomes longer, according to the simulation [78]. Fig. 3.53 shows the population in ground state as a function of the positron plasma length at $\rho_e = 10^8$ cm^{-3} and $T_e = 100$ K. Although a long positron plasma is not feasible due to a limited trapping region in the double cusp trap, a long electron plasma to de-excite antihydrogen atoms in Rydberg states can be prepared in downstream of the production region within the dcusp-MRE. This de-excitation is helpful for our experiment where three-body recombination is a dominant process which produces more antihydrogen atoms of higher principal quantum number as described before. Considering the length of the positron plasma for typical mixing is ~ 10 cm, the ground-state level population increases by a factor of ~ 3 when an electron plasma with the same density, temperature, and the length of 10 cm is prepared in downstream side.

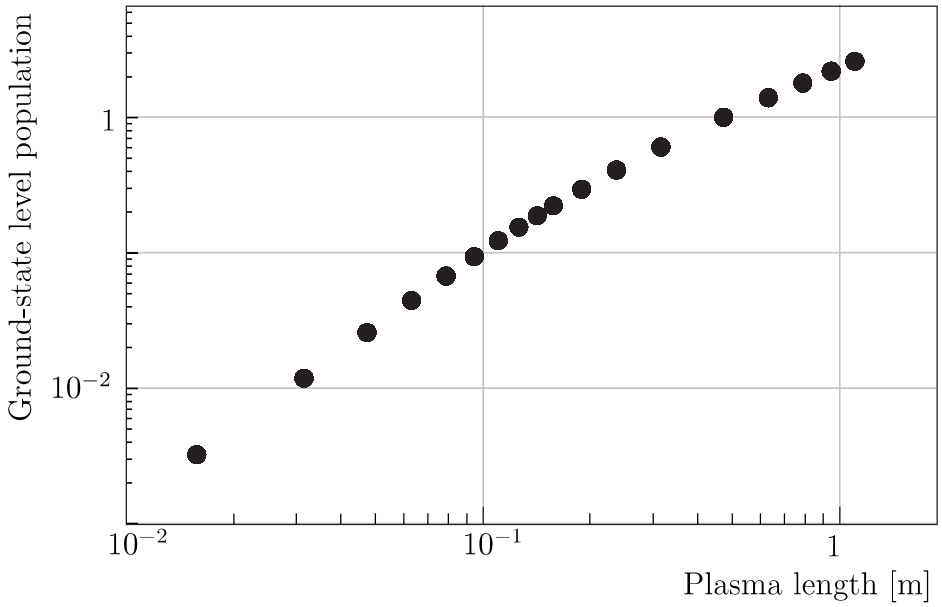

Figure 3.53: The calculated ground-state antihydrogen level population as a function of the plasma length at $\rho_e = 10^8$ cm^{-3} and $T_e = 100$ K adopted from [78]. Considering the length of the positron plasma for typical mixing is ~ 10 cm, the ground-state level population increases by a factor of ~ 3 when an electron plasma with the same density, temperature, and the length of 10 cm is prepared in downstream side.

Chapter 4

Summary

This section contains what is expected to be published within 5 years.

Appendix A

Investigation of transport of antiprotons using simulations

This section contains what is expected to be published within 5 years.

Bibliography

[1] P. A. M. Dirac. The Quantum Theory of the Electron. *Proceedings of the Royal Society A: Mathematical, Physical and Engineering Sciences*, 117(778):610–624, 1928.

[2] C. D. Anderson. The positive electron. *Physical Review*, 43(6):491–494, 1933.

[3] O. Chamberlain, E. Segre, C. Wiegand, T. Ypsilantis. Observation of Antiprotons. Technical report, Lawrence Berkeley National Laboratory, 1955.

[4] J. Alcaraz, D. Alvisi, B. Alpat, G. Ambrosi, H. Anderhub, L. Ao, A. Arefiev, P. Azzarello, E. Babucci, L. Baldini, M. Basile, D. Barancourt, F. Barao, G. Barbier, G. Barreira, R. Battiston, R. Becker, U. Becker, L. Bellagamba, P. Béné, J. Berdugo, P. Berges, B. Bertucci, A. Biland, S. Bizzaglia, S. Blasko, G. Boella, M. Bourquin, G. Bruni, M. Buenerd, J. Burger, W. Burger, X. Cai, et al. Search for antihelium in cosmic rays. *Physics Letters B*, 461(4):387–396, 1999.

[5] D. J. Fixsen. The temperature of the cosmic microwave background. *The Astrophysical Journal*, 707(2):916–920, 2009.

[6] W. Buchmüller, P. Di Bari, M. Plümacher. Cosmic microwave background, matter-antimatter asymmetry and neutrino masses. *Nuclear Physics B*, 643(1-3):367–390, 2002.

[7] A. D. Sakharov. Violation of CP in variance, C asymmetry, and baryon asymmetry of the universe. *Soviet Physics Uspekhi*, 34(5):392–393, 1991.

[8] C. S. Wu, E. Ambler, R. W. Hayward, D. D. Hoppes, R. P. Hudson. Experimental Test of Parity Conservation in Beta Decay. *Physical Review*, 105(4):1413–1415, 1957.

[9] T. D. Lee, C. N. Yang. Question of parity conservation in weak interactions. *Physical Review*, 104(1):254–258, 1956.

[10] A. Alavi-Harati, I. F. Albuquerque, T. Alexopoulos, M. Arenton, K. Arisaka, S. Averitte, A. R. Barker, L. Bellantoni, A. Bellavance, J. Belz, R. Ben-David, D. R. Bergman, E. Blucher, G. J. Bock, C. Bown, S. Bright, E. Cheu, S. Childress, R. Coleman, M. D. Corcoran, G. Corti, B. Cox, M. B. Crisler, A. R. Erwin, R. Ford, A. Glazov, A. Golossanov, G. Graham, J. Graham, K. Hagan, E. Halkiadakis, K. Hanagaki, S. Hidaka, et al. Observation of Direct CP Violation in $K_{S,L} \to \pi\pi$ Decays. *Physical Review Letters*, 83(1):22–27, 1999.

[11] V. Fanti, A. Lai, D. Marras, L. Musa, A. Bevan, T. Gershon, B. Hay, R. Moore, K. Moore, D. Munday, M. Needham, M. Parker, S. Takach, T. White, S. Wotton, G. Barr, H. Blümer, G. Bocquet, J. Bremer, A. Ceccucci, J. Cogan, D. Cundy, N. Doble, W. Funk, L. Gatignon, A. Gianoli, A. Gonidec, G. Govi, P. Grafström, G. Kesseler, W. Kubischta, A. Lacourt, S. Luitz, et al. A new measurement of direct CP violation in two pion decays of the neutral kaon. *Physics Letters B*, 465(1-4):335–348, 1999.

[12] B. Aubert, D. Boutigny, I. De Bonis, J.-M. Gaillard, A. Jeremie, Y. Karyotakis, J. P. Lees, P. Robbe, V. Tisserand, A. Palano, G. P. Chen, J. C. Chen, N. D. Qi, G. Rong, P. Wang, Y. S. Zhu, G. Eigen, P. L. Reinertsen, B. Stugu, B. Abbott, G. S. Abrams, A. W. Borgland, A. B. Breon, D. N. Brown, J. Button-Shafer, R. N. Cahn, A. R. Clark, S. Dardin, C. Day, S. F. Dow, T. Elioff, Q. Fan, I. Gaponenko, et al. Measurement of *CP*-Violating Asymmetries in B^0 Decays to *CP* Eigenstates. *Physical Review Letters*, 86(12):2515–2522, 2001.

[13] K. Abe, K. Abe, R. Abe, I. Adachi, B. S. Ahn, H. Aihara, M. Akatsu, G. Alimonti, K. Asai, M. Asai, Y. Asano, T. Aso, V. Aulchenko, T. Aushev, A. M. Bakich, E. Banas, S. Behari, P. K. Behera, D. Beiline, A. Bondar, A. Bozek, T. E. Browder, B. C. K. Casey, P. Chang, Y. Chao, K.-F. Chen, B. G. Cheon, R. Chistov, S.-K. Choi, Y. Choi, L. Y. Dong, J. Dragic, A. Drutskoy, et al. Observation of Large *CP* Violation in the Neutral *B* Meson System. *Physical Review Letters*, 87(9):091802, 2001.

[14] L. Canetti, M. Drewes, M. Shaposhnikov. Matter and antimatter in the universe. *New Journal of Physics*, 14(9):095012, 2012.

[15] Y. Fukuda, T. Hayakawa, E. Ichihara, K. Inoue, K. Ishihara, H. Ishino, Y. Itow, T. Kajita, J. Kameda, S. Kasuga, K. Kobayashi, Y. Kobayashi, Y. Koshio, M. Miura, M. Nakahata,

S. Nakayama, A. Okada, K. Okumura, N. Sakurai, M. Shiozawa, Y. Suzuki, Y. Takeuchi, Y. Totsuka, S. Yamada, M. Earl, A. Habig, E. Kearns, M. D. Messier, K. Scholberg, J. L. Stone, L. R. Sulak, C. W. Walter, M. Goldhaber, et al. Evidence for Oscillation of Atmospheric Neutrinos. *Physical Review Letters*, 81(8):1562–1567, 1998.

[16] Q. R. Ahmad, R. C. Allen, T. C. Andersen, J. D.Anglin, J. C. Barton, E. W. Beier, M. Bercovitch, J. Bigu, S. D. Biller, R. A. Black, I. Blevis, R. J. Boardman, J. Boger, E. Bonvin, M. G. Boulay, M. G. Bowler, T. J. Bowles, S. J. Brice, M. C. Browne, T. V. Bullard, G. Bühler, J. Cameron, Y. D. Chan, H. H. Chen, M. Chen, X. Chen, B. T. Cleveland, E. T. H. Clifford, J. H. M. Cowan, D. F. Cowen, G. A. Cox, X. Dai, F. Dalnoki-Veress, et al. Direct Evidence for Neutrino Flavor Transformation from Neutral-Current Interactions in the Sudbury Neutrino Observatory. *Physical Review Letters*, 89(1):011301, 2002.

[17] O. W. Greenberg. CPT Violation Implies Violation of Lorentz Invariance. *Physical Review Letters*, 89(23):231602, 2002.

[18] S. M. Carroll, J. Shu. Models of baryogenesis via spontaneous Lorentz violation. *Physical Review D - Particles, Fields, Gravitation and Cosmology*, 73(10):1–13, 2006.

[19] R. Bluhm, V. A. Kostelecký, N. Russell. CPT and Lorentz Tests in Hydrogen and Antihydrogen. *Physical Review Letters*, 82(11):2254–2257, 1999.

[20] V. A. Kostelecky, A. J. Vargas. Lorentz and CPT tests with hydrogen, antihydrogen, and related systems. *Physical Review D - Particles, Fields, Gravitation and Cosmology*, 92(5):1–39, 2015.

[21] M. Pospelov. Breaking of CPT and Lorentz symmetries. *Hyperfine Interactions*, 172(1-3):63–70, 2006.

[22] M. C. Fujiwara, G. B. Andresen, W. Bertsche, P. D. Bowe, C. C. Bray, E. Butler, C. L. Cesar, S. Chapman, M. Charlton, J. Fajans, R. Funakoshi, D. R. Gill, J. S. Hangst, W. N. Hardy, R. S. Hayano, M. E. Hayden, A. J. Humphries, R. Hydomako, M. J. Jenkins, L. V. Jørgensen, L. Kurchaninov, W. Lai, R. Lambo, N. Madsen, P. Nolan, K. Olchanski, A. Olin, A. Povilus, P. Pusa, F. Robicheaux, E. Sarid, S. S. El Nasr, D. M. Silveira, et al. Particle Physics Aspects of Antihydrogen Studies with ALPHA at CERN. In *AIP Conference Proceedings*, volume 1037, pages 208–220, 2008.

[23] C. Patrignani et al. (Particle Data Group). Review of Particle Physics. *Chinese Physics C*, 40(10):100001, 2016.

[24] G. Baur, G. Boero, a. Brauksiepe, a. Buzzo, W. Eyrich, R. Geyer, D. Grzonka, J. Hauffe, K. Kilian, M. LoVetere, M. Macri, M. Moosburger, R. Nellen, W. Oelert, S. Passaggio, a. Pozzo, K. Röhrich, K. Sachs, G. Schepers, T. Sefzick, R. Simon, R. Stratmann, F. Stinzing, M. Wolke. Production of antihydrogen. *Physics Letters B*, 368(3):251–258, 1996.

[25] M. Amoretti, C. Amsler, G. Bonomi, A. Bouchta, P. Bowe, C. Carraro, C. L. Cesar, M. Charlton, M. J. T. Collier, M. Doser, V. Filippini, K. S. Fine, A. Fontana, M. C. Fujiwara, R. Funakoshi, P. Genova, J. S. Hangst, R. S. Hayano, M. H. Holzscheiter, L. V. Jørgensen, V. Lagomarsino, R. Landua, D. Lindelof, E. L. Rizzini, M. Macri, N. Madsen, G. Manuzio, M. Marchesotti, P. Montagna, H. Pruys, C. Regenfus, P. Riedler, J. Rochet, et al. Production and detection of cold antihydrogen atoms. *Nature*, 419(October):456–459, 2002.

[26] G. Gabrielse, N. S. Bowden, P. Oxley, A. Speck, C. H. Storry, J. N. Tan, M. Wessels, D. Grzonka, W. Oelert, G. Schepers, T. Sefzick, J. Walz, H. Pittner, T. W. Hänsch, E. A. Hessels, E. A. Hessels. Background-Free Observation of Cold Antihydrogen with Field-Ionization Analysis of Its States. *Physical Review Letters*, 89(21):213401, 2002.

[27] M. Ahmadi, M. Baquero-Ruiz, W. Bertsche, E. Butler, A. Capra, C. Carruth, C. L. Cesar, M. Charlton, A. E. Charman, S. Eriksson, L. T. Evans, N. Evetts, J. Fajans, T. Friesen, M. C. Fujiwara, D. R. Gill, A. Gutierrez, J. S. Hangst, W. N. Hardy, M. E. Hayden, C. A. Isaac, A. Ishida, S. A. Jones, S. Jonsell, L. Kurchaninov, N. Madsen, D. Maxwell, J. T. K. McKenna, S. Menary, J. M. Michan, T. Momose, J. J. Munich, P. Nolan, et al. An improved limit on the charge of antihydrogen from stochastic acceleration. *Nature*, 529(7586):373–376, 2016.

[28] H. Hellwig, R. F. C. Vessot, M. W. Levine, P. W. Zitzewitz, D. W. Allan, D. J. Glaze. Measurement of the Unperturbed Hydrogen Hyperfine Transition Frequency. *IEEE Transactions on Instrumentation and Measurement*, 19(4):200–209, 1970.

[29] L. Essen, R. W. Donaldson, M. J. Bangham, E. G. Hope. Frequency of the Hydrogen Maser. *Nature*, 229(5280):110–111, 1971.

[30] N. F. Ramsey. Experiments with separated oscillatory fields and hydrogen masers. *Reviews of Modern Physics*, 62(3):541–552, 1990.

[31] C. E. Carlson, V. Nazaryan, K. Griffioen. Proton structure corrections to electronic and muonic hydrogen hyperfine splitting. *Physical Review A*, 78(2):022517, 2008.

[32] H. Nagahama, C. Smorra, S. Sellner, J. Harrington, T. Higuchi, M. J. Borchert, T. Tanaka, M. Besirli, A. Mooser, G. Schneider, K. Blaum, Y. Matsuda, C. Ospelkaus, W. Quint, J. Walz, Y. Yamazaki, S. Ulmer. Sixfold improved single particle measurement of the magnetic moment of the antiproton. *Nature Communications*, 8:14084, 2017.

[33] G. Breit, I. I. Rabi. Measurement of Nuclear Spin. *Physical Review*, 38(11):2082–2083, 1931.

[34] A. Mohri, Y. Yamazaki. A possible new scheme to synthesize antihydrogen and to prepare a polarised antihydrogen beam. *Europhysics Letters (EPL)*, 63(2):207–213, 2003.

[35] M. Diermaier. Determination of the Hydrogen Ground-State Hyperfine Splitting in a Beam and Perspectives for Antihydrogen. PhD thesis, Eingereicht an der Technischen Universität Wien, 2016.

[36] A. G. Prodell, P. Kusch. The Hyperfine Structure of Hydrogen and Deuterium. *Physical Review*, 88(2):184–190, 1952.

[37] P. Kusch. Redetermination of the Hyperfine Splittings of Hydrogen and Deuterium in the Ground State. *Physical Review*, 100(4):1188–1190, 1955.

[38] S. Federmann. A Spin-Flip Cavity for Microwave Spectroscopy of Antihydrogen. PhD thesis, Universität Wien, 2012.

[39] M. Ahmadi, B. X. R. Alves, C. J. Baker, W. Bertsche, E. Butler, A. Capra, C. Carruth, C. L. Cesar, M. Charlton, S. Cohen, R. Collister, S. Eriksson, A. Evans, N. Evetts, J. Fajans, T. Friesen, M. C. Fujiwara, D. R. Gill, A. Gutierrez, J. S. Hangst, W. N. Hardy, M. E. Hayden, C. A. Isaac, A. Ishida, M. A. Johnson, S. A. Jones, S. Jonsell, L. Kurchaninov, N. Madsen, M. Mathers, D. Maxwell, J. T. K. McKenna, S. Menary, et al. Observation of the hyperfine spectrum of antihydrogen. *Nature*, 548(7665):66–69, 2017.

[40] J. R. Danielson, D. H. E. Dubin, R. G. Greaves, C. M. Surko. Plasma and trap-based techniques for science with positrons. *Reviews of Modern Physics*, 87(1):247–306, 2015.

[41] J. H. Malmberg, T. M. O'Neil. Pure electron plasma, liquid, and crystal. *Physical Review Letters*, 39(21):1333–1336, 1977.

[42] S. A. Prasad, T. M. O'Neil. Finite length thermal equilibria of a pure electron plasma column. *Physics of Fluids*, 22(2):278, 1979.

[43] A. Mohri, H. Higaki, H. Tanaka, Y. Yamazawa, M. Aoyagi, T. Yuyama, T. Michishita. Confinement of nonneutral spheroidal plasmas in multi-ring electrode traps. *Japanese Journal of Applied Physics, Part 1: Regular Papers and Short Notes and Review Papers*, 37(2):664–670, 1998.

[44] X. Fei. Trapping low energy antiprotons in an ion trap. PhD thesis, Harvard University, 1990.

[45] N. Kuroda, H. A. Torii, Y. Nagata, M. Shibata, Y. Enomoto, H. Imao, Y. Kanai, M. Hori, H. Saitoh, H. Higaki, A. Mohri, K. Fujii, C. H. Kim, Y. Matsuda, K. Michishio, Y. Nagashima, M. Ohtsuka, K. Tanaka, Y. Yamazaki. Development of a monoenergetic ultraslow antiproton beam source for high-precision investigation. *Physical Review Special Topics - Accelerators and Beams*, 15(2):1–10, 2012.

[46] M. Hori, J. Walz. Physics at CERN's antiproton decelerator. *Progress in Particle and Nuclear Physics*, 72:206–253, 2013.

[47] S. Maury. The Antiproton Decelerator: AD. *Hyperfine Interactions*, 109(1/4):43–52, 1997.

[48] Y. Bylinsky, A. M. Lombardi, W. Pirkl. RFQD - a Decelerating Radio Frequency Quadrupole for the CERN Antiproton Facility. In *Linac. Proceedings, 20th International Conference, Linac2000*, volume C00821, pages 554–556, Monterey, USA, 2000.

[49] B. R. Beck, J. Fajans, J. H. Malmberg. Temperature and anisotropic-temperature relaxation measurements in cold, pure-electron plasmas. *Physics of Plasmas*, 3(4):1250, 1996.

[50] 黒田直史. Accumulation of a large number of antiprotons and production of an ultra-slow antiproton beam. PhD thesis, The University of Tokyo, 2003.

[51] N. Kuroda, H. A. Torii, M. Shibata, Y. Nagata, D. Barna, M. Hori, D. Horváth, A. Mohri, J. Eades, K. Komaki, Y. Yamazaki. Radial Compression of an Antiproton Cloud for Production of Intense Antiproton Beams. *Physical Review Letters*, 100(20):203402, 2008.

[52] G. B. Andresen, W. Bertsche, P. D. Bowe, C. C. Bray, E. Butler, C. L. Cesar, S. Chapman, M. Charlton, J. Fajans, M. C. Fujiwara, R. Funakoshi, D. R. Gill, J. S. Hangst, W. N. Hardy, R. S. Hayano, M. E. Hayden, R. Hydomako, M. J. Jenkins, L. V. Jørgensen, L. Kurchaninov, R. Lambo, N. Madsen, P. Nolan, K. Olchanski, A. Olin, A. Povilus, P. Pusa, F. Robicheaux, E. Sarid, S. Seif El Nasr, D. M. Silveira, J. W. Storey, R. I. Thompson, et al. Compression of Antiproton Clouds for Antihydrogen Trapping. *Physical Review Letters*, 100(20):203401, 2008.

[53] A. P. Mills, E. M. Gullikson. Solid neon moderator for producing slow positrons. *Applied Physics Letters*, 49(17):1121–1123, 1986.

[54] T. J. Murphy, C. M. Surko. Positron trapping in an electrostatic well by inelastic collisions with nitrogen molecules. *Physical Review A*, 46(9):5696–5705, 1992.

[55] Y. Nagata, Y. Yamazaki. A novel property of anti-Helmholz coils for in-coil syntheses of antihydrogen atoms: formation of a focused spin-polarized beam. *New Journal of Physics*, 16(8):083026, 2014.

[56] 榎本嘉範. Antihydrogen production in cusp trap. PhD thesis, The University of Tokyo, 2011.

[57] C. Ghesquière. An inclusive view on $\overline{p}p \to n\pi$ at rest. In *Symposium on antinucleon-nucleon interactions*, pages 436–446, 1974.

[58] Y. Nagata, N. Kuroda, M. Ohtsuka, M. Leali, E. Lodi-Rizzini, V. Mascagna, M. Tajima, H. A. Torii, N. Zurlo, Y. Matsuda, L. Venturelli, Y. Yamazaki. Direct detection of antihydrogen atoms using a BGO crystal. *Nuclear Instruments and Methods in Physics Research, Section A: Accelerators, Spectrometers, Detectors and Associated Equipment*, 840(May):153–159, 2016.

[59] G. Gabrielse, S. Rolston, L. Haarsma, W. Kells. Antihydrogen production using trapped plasmas. *Physics Letters A*, 129(1):38–42, 1988.

[60] G. Gabrielse, S. L. Rolston, L. Haarsma, W. Kells. Possible antihydrogen production using trapped plasmas. *Hyperfine Interactions*, 44(1-4):287–293, 1989.

[61] Y. Enomoto, N. Kuroda, K. Michishio, C. H. Kim, H. Higaki, Y. Nagata, Y. Kanai, H. A. Torii, M. Corradini, M. Leali, E. Lodi-Rizzini, V. Mascagna, L. Venturelli, N. Zurlo, K. Fujii, M. Ohtsuka, K. Tanaka, H. Imao, Y. Nagashima, Y. Matsuda, B. Juhász, A. Mohri, Y. Yamazaki. Synthesis of Cold Antihydrogen in a Cusp Trap. *Physical Review Letters*, 105(24):243401, 2010.

[62] S. Agostinelli, J. Allison, K. Amako, J. Apostolakis, H. Araujo, P. Arce, M. Asai, D. Axen, S. Banerjee, G. Barrand, F. Behner, L. Bellagamba, J. Boudreau, L. Broglia, A. Brunengo, H. Burkhardt, S. Chauvie, J. Chuma, R. Chytracek, G. Cooperman, G. Cosmo, P. Degtyarenko, A. Dell'Acqua, G. Depaola, D. Dietrich, R. Enami, A. Feliciello, C. Ferguson, H. Fesefeldt, G. Folger, F. Foppiano, A. Forti, S. Garelli, et al. GEANT4 - A simulation toolkit. *Nuclear Instruments and Methods in Physics Research, Section A: Accelerators, Spectrometers, Detectors and Associated Equipment*, 506(3):250–303, 2003.

[63] N. Kuroda, S. Ulmer, D. J. Murtagh, S. Van Gorp, Y. Nagata, M. Diermaier, S. Federmann, M. Leali, C. Malbrunot, V. Mascagna, O. Massiczek, K. Michishio, T. Mizutani, A. Mohri, H. Nagahama, M. Ohtsuka, B. Radics, S. Sakurai, C. Sauerzopf, K. Suzuki, M. Tajima, H. a. Torii, L. Venturelli, B. Wünschek, J. Zmeskal, N. Zurlo, H. Higaki, Y. Kanai, E. Lodi Rizzini, Y. Nagashima, Y. Matsuda, E. Widmann, Y. Yamazaki. A source of antihydrogen for in-flight hyperfine spectroscopy. *Nature communications*, 5:3089, 2014.

[64] J. D. Jackson. *Classical electrodynamics*. John Wiley & Sons, 3rd edition, 1998.

[65] B. Radics, S. Ishikawa, N. Kuroda, D. J. Murtagh, Y. Nagata, M. Tajima, S. Van Gorp, Y. Abo, P. Dupre, Y. Higashi, C. Kaga, M. Leali, V. Mascagna, L. Venturelli, N. Zurlo, H. Breuker, H. Higaki, Y. Kanai, E. L. Rizzini, Y. Matsuda, S. Ulmer, Y. Yamazaki. Antihydrogen synthesis in a double-CUSP trap towards test of the CPT-symmetry. *Hyperfine Interactions*, 237(1):156, 2016.

[66] N. Kuroda, A. Mohri, H. A. Torii, Y. Nagata, M. Shibata. First Observation of a (1,0) Mode Frequency Shift of an Electron Plasma at Antiproton Beam Injection. *Physical Review Letters*, 113(2):025001, 2014.

[67] B. Radics, Y. Nagata, Y. Yamazaki, S. Ishikawa, N. Kuroda, Y. Matsuda, M. Anfreville, S. Aune, M. Boyer, F. Chateau, M. Combet, R. Granelli, P. Legou, I. Mandjavidze, S. Procureur, M. Riallot, B. Vallage, M. Vandenbroucke. The ASACUSA Micromegas Tracker: A cylindrical, bulk Micromegas detector for antimatter research. *Review of Scientific Instruments*, 86(8), 2015.

[68] V. Mäckel, B. Radics, P. Dupre, H. Higaki, Y. Kanai, N. Kuroda, Y. Nagata, M. Tajima, Y. Matsuda, E. Widmann, Y. Yamazaki. Imaging antimatter with a micromegas detector (to be published).

[69] R. Hayano. ASACUSA STATUS REPORT Recent progress and plans for 2017. Technical Report CERN-SPSC-2017-005. SPSC-SR-203, CERN, Geneva, 2017.

[70] S. Martin. private communications, 2015.

[71] Y. Nagata, N. Kuroda, B. Kolbringer, M. Fleck, C. Malbrunot, V. Mäckel, C. Sauerzopf, M. Simon, M. Tajima, H. Breuker, H. Higaki, Y. Kanai, Y. Matsuda, S. Ulmer, L. Venturelli, E. Widmann, Y. Yamazaki. A non-segmented bgo crystal disk with two dimensional readout for an antihydrogen beam detector and data analysis for antihydrogen identification (to be published).

[72] K. Bernadette. to be published.

[73] R. Hayano. ASACUSA STATUS REPORT - Recent progress and plans for 2016. Technical Report CERN-SPSC-2016-001. SPSC-SR-174, CERN, Geneva, 2016.

[74] A. Müller, A. Wolf. Production of antihydrogen by recombination of pbar with e+: What can we learn from electron-ion collision studies? *Hyperfine Interactions*, 109(1-4):233–267, 1997.

[75] C. Kaga, H. Higaki, K. Fukushima, K. Osaki, K. Ito, H. Okamoto. Simulations on mixing charged particles in a nested Penning trap. *JPS conference proceedings*, 18(011013):159–164, 2017.

[76] B. Radics, D. J. Murtagh, Y. Yamazaki, F. Robicheaux. Scaling behavior of the ground-state antihydrogen yield as a function of positron density and temperature from classical-trajectory Monte Carlo simulations. *Physical Review A - Atomic, Molecular, and Optical Physics*, 90(3):1–6, 2014.

[77] W. Ketterle, N. V. Druten. Evaporative Cooling of Trapped Atoms. *Advances In Atomic, Molecular, and Optical Physics*, 37(C):181–236, 1996.

[78] B. Radics, Y. Yamazaki. Antihydrogen level population evolution: impact of positron plasma length. *Journal of Physics B: Atomic, Molecular and Optical Physics*, 49(6):064007, 2016.

Acknowledgement

I would like to thank Prof. Yasuyuki Matsuda for his generous support in many aspects continuously from the master course. He gives me a lot of advice for this thesis. I would like to thank Prof. Yasunori Yamazaki, the leader of the ASACUSA antihydrogen experimental group, for giving me a great opportunity to join the collaboration. He always gives me a lot of insight during discussions.

I would like to thank Dr. Naofumi Kuroda for his great support throughout my work including the design of the experiment, technical details, fruitful discussions, data analysis, and life at Geneva. He is a hard worker and his attitude has been motivated me a lot. Without his guidance and persistent help this thesis would not have been possible. I would like to thank Dr. Hiroyuki A Torii for his suggestions about my work and life at CERN. I would like to thank Dr. Hiroyuki Higaki for his suggestions especially on plasma physics. I would like to thank Dr. Yasuyuki Kanai for teaching me how to handle many experimental devices. I would like to thank Dr. Yugo Nagata for interesting discussions especially on the antihydrogen detector. I would like to thank Dr. Stefan Ulmer, Dr. Chloé Malbrunot and Prof. Eberhard Widmann for their advice on my work and suggestions to the experimental plan. I would like to thank Dr. Daniel J Murtagh, Dr. Pierre Dupré, and Mr. Tatsuhito Kobayashi for their work on the positron manipulation. I would like to thank Dr. Yoshinori Enomoto for his great work on the single cusp trap and his advice especially on electronic circuits. I would like to thank Dr. Simon Van Gorp for his work on the double cusp trap. I would like to thank Dr. Balint Radics, Dr. Volkhard Mäckel, Mr. Shoichiro Ishikawa, and the team at Saclay for their work on the ASACUSA MicroMEGAS detector. I would like to also thank Ms. Miki Ohtsuka, Dr. Clemens Sauerzopf, Ms. Bernadette Kolbringer, Mr. Markus Fleck for their work on the antihydrogen detector. I would like to thank Dr. Martin Simon for his work on the field ionizer. I would like to thank Prof. Luca Venturelli, Dr. Vallerio Mascagna, Dr. Marco Leali for their work on the array detector. I would like to thank Dr. Hiroki Nagahama, Mr. Takehiro Mizutani, Mr. Yoshitaka Higashi, Mr. Takuya Matsudate, and Dr. Chikato Kaga for working with me during beamtime. Again, I would like to thank all the members of the ASACUSA collaboration. It has been invaluable experience for me to work with great collaborators.

I would like to thank all the laboratory members at the University of Tokyo for their warm support and encouragement. I would like to thank RIKEN for their financial support and great environment for research through the Junior Research Associate program. I also would like to thank all the members of the former atomic research group and fundamental symmetries laboratory at RIKEN including secretaries, Ms. Hitomi Wada, Ms. Machiko Izawa, and Ms. Megumi Morita, for their support.

Finally I would like to thank my family for their constant love and financial support.